

INFORMATION TO USERS

This manuscript has been reproduced from the microfilm master. UMI films the text directly from the original or copy submitted. Thus, some thesis and dissertation copies are in typewriter face, while others may be from any type of computer printer.

The quality of this reproduction is dependent upon the quality of the copy submitted. Broken or indistinct print, colored or poor quality illustrations and photographs, print bleedthrough, substandard margins, and improper alignment can adversely affect reproduction.

In the unlikely event that the author did not send UMI a complete manuscript and there are missing pages, these will be noted. Also, if unauthorized copyright material had to be removed, a note will indicate the deletion.

Oversize materials (e.g., maps, drawings, charts) are reproduced by sectioning the original, beginning at the upper left-hand corner and continuing from left to right in equal sections with small overlaps.

Photographs included in the original manuscript have been reproduced xerographically in this copy. Higher quality 6" x 9" black and white photographic prints are available for any photographs or illustrations appearing in this copy for an additional charge. Contact UMI directly to order.

**ProQuest Information and Learning
300 North Zeeb Road, Ann Arbor, MI 48106-1346 USA
800-521-0600**

UMI[®]

University of Alberta

Polythermal Glacier Hydrology and Ice Flow Dynamics

by

Luke Copland 

**A thesis submitted to the Faculty of Graduate Studies and Research in partial fulfillment
of the requirements for the degree of Doctor of Philosophy**

Department of Earth and Atmospheric Sciences

Edmonton, Alberta

Fall 2001



**National Library
of Canada**

**Acquisitions and
Bibliographic Services**

**395 Wellington Street
Ottawa ON K1A 0N4
Canada**

**Bibliothèque nationale
du Canada**

**Acquisitions et
services bibliographiques**

**395, rue Wellington
Ottawa ON K1A 0N4
Canada**

Your file *Votre référence*

Our file *Notre référence*

The author has granted a non-exclusive licence allowing the National Library of Canada to reproduce, loan, distribute or sell copies of this thesis in microform, paper or electronic formats.

The author retains ownership of the copyright in this thesis. Neither the thesis nor substantial extracts from it may be printed or otherwise reproduced without the author's permission.

L'auteur a accordé une licence non exclusive permettant à la Bibliothèque nationale du Canada de reproduire, prêter, distribuer ou vendre des copies de cette thèse sous la forme de microfiche/film, de reproduction sur papier ou sur format électronique.

L'auteur conserve la propriété du droit d'auteur qui protège cette thèse. Ni la thèse ni des extraits substantiels de celle-ci ne doivent être imprimés ou autrement reproduits sans son autorisation.

0-612-68921-2

Canada

University of Alberta

Library Release Form

Name of Author: Luke Copland


Title of Thesis: Polythermal Glacier Hydrology and Ice Flow Dynamics

Degree: Doctor of Philosophy

Year this Degree Granted: 2001

Permission is hereby granted to the University of Alberta Library to reproduce single copies of this thesis and to lend or sell such copies for private, scholarly or scientific research purposes only.

The author reserves all other publication and other rights in association with the copyright in the thesis, and except as herein before provided, neither the thesis nor any substantial portion thereof may be printed or otherwise reproduced in any material form whatever without the author's written permission.



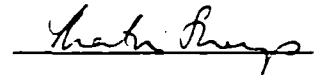
Department of Earth & Atmospheric Sciences
University of Alberta
Edmonton, Alberta T6G 2E3, Canada

Date: September 12, 2001

University of Alberta

Faculty of Graduate Studies and Research

The undersigned certify that they have read, and recommend to the Faculty of Graduate Studies and Research for acceptance, a thesis entitled Polythermal Glacier Hydrology and Ice Flow Dynamics by Luke Copland in partial fulfillment of the requirements for the degree of Doctor of Philosophy



Dr. Martin Sharp



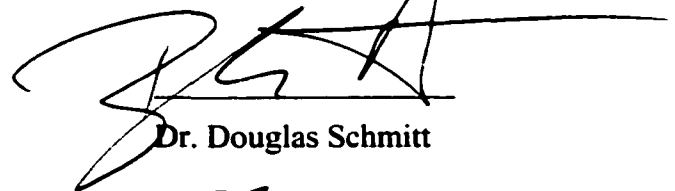
Dr. Benoit Rivard



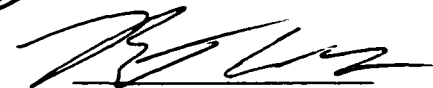
Dr. Andrew Bush



Dr. Edward Lozowski



Dr. Douglas Schmitt



For Dr. Garry Clarke

Date: September 12, 2001

ABSTRACT

Measurements at polythermal John Evans Glacier, Ellesmere Island, indicate strong links between spatial and temporal variations in subglacial hydrology and changes in surface velocity. Radio-echo sounding was used to determine ice thicknesses and bed topography, which allowed reconstruction of likely subglacial flow routing. Spatial patterns in residual bed reflection power (BRP_r) enabled identification of warm and cold areas of the glacier bed. Within warm areas, the detailed pattern of BRP_r was similar to the pattern of predicted subglacial water flow.

Long-term ice motion measurements along a centre-line of 20 stakes indicate summer velocities slightly higher than overwinter levels in the accumulation area, but up to double overwinter levels in the ablation area. To assess the importance of basal motion in accounting for these patterns, expected ice deformation rates were calculated based on the likely range of ice temperatures and longitudinal coupling lengths at the glacier. In the accumulation and upper ablation areas, predicted motion due to ice deformation closely matched observations in both summer and winter. In the lower ablation area, basal motion was required in addition to ice deformation, with the largest basal velocities centred over the areas of predicted subglacial drainage. In addition, there was a rapid onset to summer basal motion directly below a set of moulins which provide the main route for surface meltwater to reach the glacier bed.

Short-term ice motion measurements record three short-term (two- to four-day) high velocity events in summer 1998 and 1999, with velocities >100% above overwinter levels. These events were associated with periods of rapidly increasing meltwater input to

the subglacial drainage system. The first events in 1998 and 1999 occurred at the start of the melt season at the transition from a snow covered to an ice covered surface. A second event in 1999 occurred midway through the summer as surface melting resumed following a cold period, and was strongly localised along a predicted subglacial drainage axis.

ACKNOWLEDGEMENTS

I am very grateful to the University of Alberta Ph.D. Scholarship, University of Alberta Izaak Walton Killam Memorial Scholarship, University of Alberta Department of Earth and Atmospheric Sciences, University of Alberta Andrew Stewart Memorial Graduate Prize, Natural Sciences and Engineering Research Council of Canada, University of Alberta Institute for Geophysical Research, Natural Environment Research Council of the United Kingdom, Polar Continental Shelf Project, Geological Society of America, and the Canadian Circumpolar Institute of the University of Alberta for funding and field logistics. I would like to thank the Nunavut Research Institute and the communities of Resolute Bay and Grise Fiord for permission to work at John Evans Glacier, and Wendy Davis, Darek Glowacki, Anthony Arendt, Trudy Wohlleben, James Davis, Joel Barker, Candice Stuart, Sarah Boon, Karen Heppenstall, Peter Nienow and Rob Bingham for help in the field. Martin Sharp provided excellent guidance throughout the completion of this thesis, both in the field and in Edmonton.

I would like to thank my parents for their support throughout my graduate career, and for encouraging me to follow my love of glaciers. Finally, I would like to thank Trudy Wohlleben for her help and companionship during the last four years, and for her continued interest in my research.

TABLE OF CONTENTS

| | |
|--|-----------|
| CHAPTER 1: INTRODUCTION | 1 |
| 1.1 BIBLIOGRAPHY | 3 |
| | |
| CHAPTER 2: MAPPING THERMAL AND HYDROLOGICAL CONDITIONS BENEATH A POLYTHERMAL GLACIER WITH RADIO-ECHO SOUNDING | 5 |
| 2.1 INTRODUCTION | 5 |
| 2.2 STUDY SITE | 6 |
| 2.3 DATA COLLECTION | 7 |
| 2.3.1 Radar determination of bed topography | 8 |
| 2.3.2 Returned power from radio-echo sounding | 10 |
| 2.3.3 Rate of apparent attenuation with depth | 12 |
| 2.4 RESULTS AND DISCUSSION | 14 |
| 2.4.1 Distribution of warm and cold ice | 14 |
| 2.4.2 Variations in BRP _r within areas of warm ice | 16 |
| 2.4.3 Subglacial drainage reconstruction | 19 |
| 2.5 CONCLUSIONS | 21 |
| 2.6 BIBLIOGRAPHY | 22 |
| | |
| CHAPTER 3: RADIO-ECHO SOUNDING DETERMINATION OF POLYTHERMAL GLACIER HYDROLOGY | 35 |
| 3.1 INTRODUCTION | 35 |
| 3.2 STUDY SITE | 35 |
| 3.3 RESULTS | 36 |
| 3.3.1 Water input locations | 36 |
| 3.3.2 Subglacial flow routing | 37 |
| 3.3.3 Subglacial properties | 40 |
| 3.4 CONCLUSIONS | 42 |
| 3.5 BIBLIOGRAPHY | 43 |

| | |
|--|-----------|
| CHAPTER 4: THE DISTRIBUTION OF BASAL MOTION BENEATH A HIGH ARCTIC POLYTHERMAL GLACIER | 52 |
| 4.1 INTRODUCTION | 52 |
| 4.2 JOHN EVANS GLACIER | 53 |
| 4.3 MEASUREMENTS | 54 |
| 4.3.1 Ice motion | 54 |
| 4.3.2 Glacier geometry | 55 |
| 4.4 RESULTS AND ANALYSIS | 56 |
| 4.4.1 Measured ice motion | 56 |
| 4.4.2 Predicted ice motion | 57 |
| 4.4.2.1 Predicted ice motion without long stresses | 57 |
| 4.4.2.2 Predicted ice motion with long stresses | 59 |
| 4.4.2.3 Predicted ice motion with long stresses and variability in ice temperature | 60 |
| 4.4.2.4 Predicted ice motion with basal motion | 62 |
| 4.5 CONCLUSIONS | 65 |
| 4.6 BIBLIOGRAPHY | 66 |
| | |
| CHAPTER 5: LINKS BETWEEN SHORT-TERM VELOCITY VARIATIONS AND THE SUBGLACIAL HYDROLOGY OF A POLYTHERMAL GLACIER | 76 |
| 5.1 INTRODUCTION | 76 |
| 5.1.1 John Evans Glacier | 77 |
| 5.2 MEASUREMENTS | 78 |
| 5.2.1 Ice motion | 78 |
| 5.2.2 Ice motion errors | 79 |
| 5.2.3 Geophones | 81 |
| 5.2.4 Weather stations | 82 |
| 5.2.5 Discharge records | 82 |
| 5.2.6 Subglacial flow routing | 82 |
| 5.2.7 Residual vertical motion (cavity opening) | 83 |

| | |
|--|------------|
| 5.3 RESULTS | 85 |
| 5.3.1 Long-term velocities | 85 |
| 5.3.2 1999 short-term velocity events | 86 |
| 5.3.2.1 Event 1/99: days 184.60 – 189.04 | 86 |
| 5.3.2.2 Event 2/99: days 196.60 – 198.88 | 87 |
| 5.3.3 1998 short-term velocity events | 89 |
| 5.3.3.1 Event 1/98: days 180.71 – 184.71 | 89 |
| 5.4 DISCUSSION | 90 |
| 5.4.1 Early season events | 91 |
| 5.4.2 Mid-season event | 92 |
| 5.5 CONCLUSIONS | 94 |
| 5.6 BIBLIOGRAPHY | 95 |
| | |
| CHAPTER 6: SUMMARY AND CONCLUSIONS | 117 |
| 6.1 SUMMARY | 117 |
| 6.2 CONCLUSIONS | 119 |
| 6.3 BIBLIOGRAPHY | 121 |

LIST OF TABLES

CHAPTER 5

- 5.1 Summer 1999 measured horizontal velocities (cm day^{-1}) used as input for the principal components analysis. Blank cells indicate missing data; pairwise deletion was used to remove these from the analysis. Stake locations are indicated in Figure 5.2. 98
- 5.2 Eigenvalues and % explained variance for the principal component factors with an eigenvalue greater than 1. 99
- 5.3 Factor loadings for principal components analysis with the first two factors. Bold numbers indicate the factor that each stake loads most heavily on. The spatial distribution of the stakes grouped together by these factors is shown in Figure 5.3a. 100

LIST OF FIGURES

CHAPTER 2

- 2.1 Map showing the location of John Evans Glacier and the distribution of radio-echo sounding measurements made for this study 25
- 2.2 (a) A typical radio-echo sounding trace recorded at John Evans Glacier (b) Returned power from the same trace. IRP = internal reflection power, BRP = bed reflection power 26
- 2.3 (a) Raw radio-echo sounding data for a transect through the centre of Area A in Fig. 2.6 (uncorrected for surface topography). Area of high englacial reflections towards the centre of the transect is probably caused by a crevasse. (b) True surface and bed topography. (c) Bed reflection power (BRP) and internal reflection power (IRP) standardised to $\text{mV}^2 \text{ns}^{-1}$. Note the high IRP where the crevasse is located; traces with an $\text{IRP} > 2 \text{mV}^2 \text{ns}^{-1}$ were removed from further analysis (d) Residual bed reflection power (BRP_r): highest values occur over the overdeepening 27
- 2.4 (a) Relationship between ice thickness and bed reflection power for all 10 MHz traces with an internal reflection power $< 2 \text{mV}^2 \text{ns}^{-1}$ (b) Relationship between ice thickness and bed reflection power for all 10 MHz traces completed over the glacier terminus with an internal reflection power $< 2 \text{mV}^2 \text{ns}^{-1}$. Best-fit curves represent the attenuation of radar power with thickness 28
- 2.5 (a) An example of a radio-echo sounding transect across the terminus of John Evans Glacier (uncorrected for surface topography). The internal reflector is interpreted as the boundary between cold ice above and warm ice below. (b) Thickness and distribution of internal reflecting horizon across the terminus of John Evans Glacier.

White dots indicate trace locations, black dots indicate glacier boundary. X and Y mark the ends of the transect displayed in (a) 29

2.6 (a) A composite map of spatial variability in residual bed reflection power (BRP_r) across John Evans Glacier for surveys at 10 MHz and 20 MHz (black dots mark survey locations). The data from the 20 MHz surveys encompasses the area to the NE of the bedrock ridge shown in Fig. 2.6b (see Fig. 2.1 for details). Areas A, B and C display particularly high BRP_r values and are discussed in the text. (b) Basal topography of John Evans Glacier. Note correlation between valleys/overdeepenings and areas A and B of high BRP_r 30

2.7 Variability in residual bed reflection power (BRP_r) over the glacier terminus, and predicted subglacial water flow routing (marked by heavy black lines). Letters refer to features discussed in the text. Inflow indicates the location where a large marginal stream disappears beneath the glacier; outflow indicates the location of streams which exit from beneath the glacier terminus. Dashed white lines mark elongated areas D and E of high BRP_r . Black triangle marks the location where the elongated area of high BRP_r (area E) crosses an area of low BRP_r 31

2.8 Variability in BRP_r with ice thickness: (a) for positive values of BRP_r (b) for negative values of BRP_r . Positive and negative values are plotted separately because there is no upper limit to the range of positive values, while negative values cannot be less than -1 32

2.9 Relationship between bed angle and BRP_r for surveys with $IRP < 2 \text{ mV}^2 \text{ ns}^{-1}$ at: (a) 5 MHz (b) 10 MHz (c) 20 MHz. Black line shows best fit line for each plot 33

2.10 Subglacial hydraulic potential and predicted subglacial hydrological flow paths for the ablation area of John Evans Glacier for $f = 1$. Flow is not shown for the accumulation area because the bed is inferred to be cold there 34

CHAPTER 3

- 3.1 Location of John Evans Glacier 45**
- 3.2 Variability in internal reflection power (IRP) over John Evans Glacier. High values correlate with the location of crevasses and moulins. ELA = equilibrium line altitude 46**
- 3.3 An example set of traces from a common mid-point survey at John Evans Glacier. A = air wave; G = ground wave; B = bed wave. Depth to bed is ~124 m. The time for the air wave to travel between the transmitter and receiver is not taken into account. 47**
- 3.4 An example of the linear regression used to calculate the mean radio wave velocity through ice at John Evans Glacier. R^2 values were >99.99% significant for all 12 common mid-point surveys 48**
- 3.5 Subglacial flow reconstruction for the ablation area of John Evans Glacier. A is a bedrock ridge; B and C indicate overdeepened areas and separate catchments 49**
- 3.6 (a) Raw traces recorded over the repeat survey period (b) Bed reflection power of these traces corrected for date (day 190 = July 9) (c) Supraglacial and proglacial stream stage records. Part of the proglacial stream record is missing due to changes in the location of the main channel (d) Air temperature recorded at a weather station on the glacier terminus 50**
- 3.7 (a) Variability in ground wave power from the traces displayed in Figure 3.6a over the repeat survey period (b) Relationship between ground wave power and bed reflection power over the same period 51**

CHAPTER 4

- 4.1 Location of John Evans Glacier (inset), and the centre-line velocity stake network superimposed on a Landsat 7 image taken on July 10, 1999. Squares indicate stakes measured by GPS, while circles indicate stakes measured by theodolite. LWS, MWS and UWS mark the lower, middle and upper weather stations, respectively. Temperatures mark ice temperatures at 15 m depth** 68
- 4.2 Bedrock topography at John Evans Glacier determined from radio-echo sounding (Copland and Sharp, in press)** 69
- 4.3 Measured summer and winter surface velocities along the centre-line network** 70
- 4.4 For the centre-line stake transect at John Evans Glacier: (a) surface and bed topography (b) ice thickness (c) shape factor f (d) surface slope angle** 71
- 4.5 Comparison between measured and predicted surface velocities along the centre-line of John Evans Glacier from equation (1), without accounting for longitudinal stresses** 72
- 4.6 Comparison between measured and predicted surface velocities along the centre-line of John Evans Glacier from equations (2) and (3) for longitudinal coupling lengths of 2, 3 and 4 times the local ice thickness. Ice temperature variations are not taken into account. Each dot indicates a velocity stake. Stake 6 is used as the datum** 73
- 4.7 Comparison between measured and predicted surface velocities along the centre-line of John Evans Glacier from equations (4) and (3) for a longitudinal coupling length of $4h$. The differences indicate the difference in temperature between stakes 10-20 (-3°C) and stakes 1-9 (-6 , -8 or -9°C). Each dot indicates a velocity stake. Stake 6 is used as the datum** 74

- 4.8 Comparison between measured and predicted surface velocities along the centre-line of John Evans Glacier from equations (5) and (3) for a longitudinal coupling length of $4h$ and the imposed basal sliding distribution shown in each figure: (a) in the winter (b) in the summer. (c) Comparison between imposed and actual ice deformation rates for the summer and winter. Differences are caused by the influence of basal sliding on longitudinal stresses The imposed ice deformation is defined by the '5°C difference' line shown in Fig. 4.7** 75

CHAPTER 5

- 5.1 Bed topography (m asl) and location of John Evans Glacier** 101
- 5.2 Landsat 7 image of John Evans Glacier from July 1999 showing the location of the velocity stakes (numbered black dots), geophones (white dots; LG = lower geophone, MG = middle geophone, UG = upper geophone), surveying base stations (white squares), stream gauging stations (triangles). Crevasse field indicates location where most supraglacial meltwater reaches the glacier bed. Lower weather station is located next to the middle geophone** 102
- 5.3 (a) Overwinter 1999/2000 horizontal velocities. Each arrow indicates the direction and velocity of a stake. Black squares indicate stakes grouped into Factor 1 in principal components analysis; black circles indicate stakes grouped into Factor 2. (b) Overwinter 1999/2000 vertical velocities. All velocities in cm day^{-1}** 103
- 5.4 Summer 1999 mean horizontal velocities (solid line), overwinter 1999/2000 mean horizontal velocities (dashed line), errors in horizontal velocity (vertical bars), and standard deviation in horizontal velocity (grey lines): (a) for all stakes (b) for stakes grouped by factor 1 in principal components analysis (i.e., lower terminus) (c) for stakes grouped by factor 2 in principal components analysis (i.e., upper terminus). All velocities in cm day^{-1} . (d) Factor scores over time for the two factors** 104

- 5.5 Summer 1999 mean vertical velocities (solid line), overwinter 1999/2000 mean vertical velocities (dashed line), errors in vertical velocity (vertical bars), and standard deviation in vertical velocity (grey lines): (a) for all stakes (b) for stakes grouped by factor 1 in principal components analysis (i.e., lower terminus) (c) for stakes grouped by factor 2 in principal components analysis (i.e., upper terminus). All velocities in cm day^{-1} 105
- 5.6 Event 1/99 (days 184.60-189.04) velocities in cm day^{-1} : (a) horizontal (b) horizontal anomalies (i.e., difference from overwinter 1999/2000) (c) vertical (d) residual vertical: cavity opening is only likely where the assumption that $w_c = 0$ requires ϵ_{\pm} to increase with depth relative to $\epsilon_{\pm s}$. Black lines in (b) mark reconstructed subglacial drainage pathways 106
- 5.7 Summer 1999 lower weather station records: (a) air temperature (b) albedo (%): a value of 40% is defined as the approximate boundary between snow and ice (c) total surface lowering (cm), determined from an ultrasonic depth gauge (UDG) (d) rate of surface lowering (cm day^{-1}) determined from the UDG 107
- 5.8 Water pressure records for summer 1999 (see Fig. 5.2 for sensor locations). The measurements are standardized between the highest and lowest values from each sensor over the period of interest. The proglacial sensor is repositioned during breaks 108
- 5.9 Summer 1999 geophone records: (a) upper geophone (b) middle geophone (c) lower geophone. Note that only the relative magnitude of events are comparable between geophones, not the actual number of counts 109
- 5.10 Pre-Event 2/99 (days 193.92-196.60) velocities in cm day^{-1} : (a) horizontal (b) horizontal anomalies (i.e., difference from overwinter 1999/2000) (c) vertical (d)

residual vertical: cavity opening is only likely where the assumption that $w_c = 0$

requires $\dot{\epsilon}_{zz}$ to increase with depth relative to $\dot{\epsilon}_{zzs}$ 110

5.11 Event 2/99 (days 196.60-198.88) velocities in cm day^{-1} : (a) horizontal (b) horizontal anomalies (i.e., difference from overwinter 1999/2000) (c) vertical (d) residual vertical: cavity opening is only likely where the assumption that $w_c = 0$ requires

$\dot{\epsilon}_{zz}$ to increase with depth relative to $\dot{\epsilon}_{zzs}$ 111

5.12 Summer 1998 (a) horizontal and (b) vertical, mean velocity (solid line), overwinter 1999/2000 mean velocity (dashed line), errors in velocity (vertical bars), and standard deviation in velocity (grey lines). All values in cm day^{-1} . An additional 6 stakes were added to the original network of 15 from day 185 onwards 112

5.13 Event 1/98 (days 182.70-184.70) velocities in cm day^{-1} : (a) horizontal (b) horizontal anomalies (i.e., difference from overwinter 1999/2000) (c) vertical (d) residual vertical: cavity opening is only likely where the assumption that $w_c = 0$ requires

$\dot{\epsilon}_{zz}$ to increase with depth relative to $\dot{\epsilon}_{zzs}$. In (b), white circle indicates location of artesian fountain pictured in Fig. 5.15 113

5.14 Summer 1998 lower weather station records: (a) air temperature (b) albedo (%): a value of 40% is defined as the approximate boundary between snow and ice (c) total surface lowering (cm), determined from an ultrasonic depth gauge (UDG) (d) rate of surface lowering (cm day^{-1}) determined from the UDG 114

5.15 Artesian fountain observed on the lower terminus between days 180 and 186, 1998. Photograph by Martin Sharp. 115

5.16 Summer 1998 geophone records: (a) upper geophone (b) middle geophone (c) lower geophone. Note that only the relative magnitude of events are comparable between geophones, not the actual number of counts 116

CHAPTER 1

INTRODUCTION

Many studies have demonstrated that liquid water at the bed of a temperate glacier influences ice flow dynamics via the role of subglacial water pressure in reducing basal shear traction (Willis, 1995). For example, Iken and Bindshadler (1986) found a strong relationship between the basal water pressure and surface velocity of Findelengletscher, Switzerland, with ice motion greatest during a period of high water pressures at the transition from 'winter' to 'summer' hydrological conditions. Large velocity variations on temperate glaciers have been measured on timescales from hours to days, with spatial variability often localized over distances of less than one ice thickness and closely related to the structure and development of the subglacial hydrological system (e.g., Iken, 1977; Willis, 1995; Mair et al., in review).

Polythermal glaciers differ from temperate glaciers in that they contain regions of both warm and cold ice. Since liquid water can only exist in large quantities where the ice is warm, a major question is the extent to which this produces a unique subglacial drainage system, and in turn how spatial and temporal changes in this system influence surface motion. This information is important for understanding the dynamic response of glaciers to climate change, since both present day ice sheets (e.g., Antarctic) and past ice sheets (e.g., Laurentide) contain warm and cold basal areas. For example, if the climate warms, we need to know how the surface velocity field might be affected by changes in subglacial hydrology. To fully understand the links between the hydrology and dynamics of polythermal glaciers, we therefore need comprehensive information about:

- a) the internal and basal thermal structure of the glacier
- b) the ability of surface meltwater to reach the glacier bed
- c) the routing of meltwater across the glacier bed, and how this relates to the basal topography and thermal condition of the ice
- d) the distribution of basal sliding across the glacier, and its importance relative to ice deformation and total surface motion

e) whether short-term velocity variations occur on polythermal glaciers, and if they do, their relationship to spatial and temporal variations in the subglacial drainage system and basal water flow

Our knowledge of the dynamics and hydrology of polythermal glaciers is currently limited, however, by the lack of detailed information about the structure of their subglacial drainage systems, and the lack of high resolution ice motion measurements. Studies which rely on infrequent velocity measurements at a few locations likely miss many of the small scale, short-term velocity variations which can provide the most information about the controls on ice dynamics. Previous studies on polythermal glaciers have indicated that surface velocities are generally higher in the summer than the winter (Hooke et al., 1983; Andreasen, 1985; Rabus and Echelmeyer, 1997), with Iken (1974) finding a strong link between short-term high velocity events and water pressures measured in moulins at White Glacier, Axel Heiberg Island.

This thesis provides the first study which combines high spatial and temporal resolution measurements of the surface velocity field of a High Arctic polythermal glacier with detailed information about the subglacial drainage system. It is presented in paper format, with each of the four main chapters written as a standalone manuscript. As of September 12, 2001, Chapter 2 has been accepted for publication, Chapter 3 has been published, while Chapters 4 and 5 have been submitted for publication. The full titles and publication details are:

Chapter 2: Copland, L. and Sharp, M. *In press*. Mapping thermal and hydrological conditions beneath a polythermal glacier with radio-echo sounding. *Journal of Glaciology*.

Chapter 3: Copland, L. and Sharp, M. 2000. Radio-echo sounding determination of polythermal glacier hydrology. *In:* Noon, D., Stickley, G.F. and Longstaff, D. (eds.). *Eighth International Conference on Ground Penetrating Radar. SPIE Vol. 4084, 59-64.*

Chapter 4: Copland, L., Sharp, M., Nienow, P. and Bingham, R. The distribution of basal motion beneath a high Arctic polythermal glacier. Submitted to the Journal of Glaciology, July 2001.

Chapter 5: Copland, L., Sharp, M., and Nienow, P. Links between short-term velocity variations and the subglacial hydrology of a polythermal glacier. Submitted to the Journal of Glaciology, July 2001.

The co-authorship of the papers reflects the fact that the field data was collected as part of a collaborative research project at John Evans Glacier. This includes some of the radio-echo sounding transects, ice motion measurements, and meteorological and hydrological data. The data analysis and interpretation, together with the writing of the chapters/papers, were entirely my own work.

Chapter 2 provides a description of the basal topography, thermal structure and subglacial hydrology of John Evans Glacier based on radio-echo sounding measurements. Chapter 3 expands on the radio-echo sounding results to include identification of englacial structures such as crevasses and moulins, and also discusses short-term variations in bed reflection power that may be indicative of changes in subglacial hydrology. Chapter 4 compares the winter and summer ice motion patterns along the glacier centre-line, and relates these to the basal thermal and hydrological conditions discussed in Chapters 2 and 3. Finally, Chapter 5 discusses links between short-term variations in surface motion across the glacier terminus and short-term variations in basal hydrology. The summary and conclusions are presented in Chapter 6.

1.1 BIBLIOGRAPHY

Andreasen, J.-O., 1985. Seasonal surface-velocity variations on a sub-polar glacier in West Greenland. *J. Glaciol.*, **31**(109), 319-323.

Hooke, R. LeB., Brzozowski, J. and Bronge, C. 1983. Seasonal variations in surface velocity, Storglaciären, Sweden. *Geogr. Ann.*, **65A**(3-4), 263-277.

Iken, A. 1974. Velocity fluctuations of an Arctic valley glacier, a study of the White glacier, Axel Heiberg Island, Canadian Arctic Archipelago. *Axel Heiberg Island Research Reports, Glaciology no. 5*. McGill University, Montreal.

Iken, A. 1977. Variations of surface velocities of some Alpine glaciers measured at intervals of a few hours. Comparison with Arctic glaciers. *Z. Gletscherkd. Glazialgeol.*, **13**(1/2), 23-35.

Iken, A. and Bindschadler, R.A. 1986. Combined measurements of subglacial water pressure and surface ice velocity of Findelengletscher, Switzerland: conclusions about drainage system and sliding mechanism. *J. Glaciol.*, **32**(110), 101-117.

Mair, D., Sharp, M. and Willis, I. *In review*. Influence of cavity opening on subglacial drainage system evolution and configuration: Haut Glacier d'Arolla, Switzerland. *J. Glaciol.*

Rabus, B.T. and Echelmeyer, K.A. 1997. The flow of a polythermal glacier: McCall Glacier, Alaska, U.S.A. *J. Glaciol.*, **43**(145), 522-536.

Willis, I.C. 1995. Intra-annual variations in glacier motion: a review. *Prog. Phys. Geogr.*, **19**(1), 61-106.

CHAPTER 2

MAPPING THERMAL AND HYDROLOGICAL CONDITIONS BENEATH A POLYTHERMAL GLACIER WITH RADIO-ECHO SOUNDING

2.1 INTRODUCTION

Polythermal glaciers are widespread in the high latitudes, and contain ice that is both at and below the pressure melting point ('warm' and 'cold' ice, respectively). Liquid water exists where the ice is warm, and surface melt may gain access through cold surface layers to warm areas of the glacier bed via moulins and crevasses (Skidmore and Sharp, 1999). Borehole temperature measurements suggest that polythermal glaciers in the Canadian high Arctic consist predominantly of cold ice with a thin layer of warm basal ice beneath the centre of the ablation area (Blatter, 1987; Blatter and Kappenberger, 1988). This differs greatly from the polythermal glaciers found in locations such as Svalbard and northern Scandinavia, where latent heat release from re-freezing in the accumulation area results in warm ice throughout most of the accumulation and lower ablation areas. In these glaciers cold ice is generally present only in a relatively thin layer close to the surface (Holmlund and Eriksson, 1989).

In the Canadian high Arctic, the glacier margins and terminus generally remain cold and frozen to the bed due to the steep englacial temperature gradient that conducts away geothermal heat where the ice is thin. Hydrological observations suggest that, in winter, spring, and early summer, the cold margins create a thermal dam to the outflow of subglacial water, which may become ponded in the region behind the glacier terminus (Skidmore and Sharp, 1999). As meltwater inputs to the glacier bed increase in the early summer, subglacial water pressures rise, the thermal dam is breached, and the reservoir releases as an outburst flood. This behaviour contrasts markedly with the hydrology of temperate glaciers and Svalbard-type polythermal glaciers, where water outflow can continue throughout the year as drainage conduits beneath the glacier terminus do not generally close over winter (Wadham et al., 2000).

The objective of this study is to further our understanding of the hydrology and thermal regime of a polythermal glacier in the Canadian high Arctic by using high resolution radio-echo sounding to image its internal and basal properties. We analyse the presence/absence of an internal reflecting horizon, and the spatial variability in residual bed reflection power (i.e., bed reflection power corrected for variations in ice thickness), to identify the distribution of warm and cold-based ice. We then evaluate the hypothesis that spatially contiguous areas of high residual bed reflection power within areas of warm basal ice represent regions of preferred subglacial drainage. We do this by making comparisons with independent reconstructions of the pattern of subglacial drainage that are based on the form of the subglacial hydraulic potential surface derived from digital elevation models of the glacier surface and glacier bed (Copland and Sharp, 2000).

Other studies have used returned power from radio-echo sounding to identify subglacial lakes (e.g., Oswald and Robin, 1973; Robin et al., 1977; Siegert and Ridley, 1998), and to distinguish between wet and frozen beds in the Antarctic (Bentley et al., 1998; Gades et al., 2000). Gades et al. (2000) found low and nearly constant residual bed reflection power across Siple Dome. This is suggestive of ice frozen to bedrock, while high basal reflectivity under the adjacent Siple Ice Stream and Ice Stream C is indicative of a thin basal water layer or a thick thawed or frozen till layer. Gades (1998) used temporal and spatial variations in bed reflection power to monitor the subglacial conditions at Black Rapids Glacier, Alaska, during the time of annual spring speedup. Glacier-wide changes were not detected during these measurements, although variations in returned power along the glacier margins suggested that changes in the subglacial hydrological system occurred in these areas.

2.2 STUDY SITE

John Evans Glacier (79°40'N, 74°30'W) is located on the east coast of Ellesmere Island, Nunavut, Canada (Fig. 2.1). The glacier terminates on land, and occupies a 220 km² basin, of which approximately 75% is glacierized (Skidmore and Sharp, 1999). The glacier ranges in elevation from 100 m to 1200 m asl, with a mean ice thickness of ~150 m in the terminus area and a maximum ice thickness of ~400 m close to the equilibrium line at ~750-850 m asl. For the years 1997 to 1999, mean annual air temperatures were

-14.3°C at the terminus (200 m asl), -15.2°C at 850 m asl, and -14.8°C in the upper accumulation area (1150 m asl). 15 m ice temperatures in the accumulation and upper ablation areas are in the range -7 to -15°C. The melt season normally extends from early June to early August. During this period supraglacial meltwater enters the glacier interior via moulins and crevasses, and lakes form on the glacier surface and along the glacier margins.

2.3 DATA COLLECTION

The radio-echo sounding system consists of a monopulse transmitter with a peak power of 24 kW (Narod and Clarke, 1994), and an air-wave triggered oscilloscope receiver connected to a palmtop computer for digital data recording. Receiver and transmitter arms are resistively loaded dipoles, and were oriented in-line (E-plane). Centre frequencies of 5, 10 or 20 MHz were used, and traces were recorded in the time domain. To reduce noise, the received signal was low pass filtered (at 1.5x the transmitted centre frequency) and averaged at least 32 times before recording. The oscilloscope sampling interval was typically 9.8 ns (512 samples/trace with a 5000 ns time base), which equates to a Nyquist frequency (f_n) of 51 MHz. Where the ice was particularly shallow or deep, sampling intervals of 3.9 ns ($f_n = 128$ MHz) and 19.5 ns ($f_n = 26$ MHz) were occasionally used for the surveys at 20 MHz and 5 MHz, respectively. The Nyquist frequency defines the highest frequency that can be recorded, and was always well above the low pass filter level for each centre frequency. This ensures that the traces measured the full spectrum of the received wave. A 2 MHz vertical high pass finite impulse response filter, from *Radan* post-processing software (Geophysical Survey Systems, Inc.), was used to remove the slowly decaying low frequency feature that is common at the start of traces where the transmitter and receiver are in-line. This processing did not affect the timing or characteristics of the high frequency bed and internal reflections.

Traces were recorded at 3200 locations by towing the radio-echo sounding unit on two sleds behind a skidoo, skier or hiker (Fig. 2.1). Most soundings were made in May, before the start of the melt season, which ensured constant antenna-surface coupling (Copland and Sharp, 2000). This is an important consideration as Gades (1998) and

Bogorodsky et al. (1983) argue that variable amounts of surface water influence the radar power that enters the glacier. Horizontal trace locations were determined with a hand-held GPS to within ± 50 m, with interpolation between occasional GPS points where the transects were straight. The horizontal GPS co-ordinates were used to determine surface elevation from a digital elevation model (DEM) of the glacier surface derived from 1959 stereo aerial photos (Woodward et al., 1997). The surface DEM has a grid spacing of 25 m, and the derived elevations were verified against altimeter estimates. Recording traces in a regular network along straight and parallel transects was not possible due to the presence of obstacles such as large crevasses and deeply incised surface streams. To avoid such features, transects were generally completed in areas of flat surface topography, along the centre of 300-500 m wide interfluves. As discussed in Section 2.3.2, measurements that included significant returns from crevasses were discarded from the final analysis.

2.3.1 Radar determination of bed topography

Ice thickness was determined at all trace locations by manually recording the time between the first peak of the air wave and the first peak of the bed wave from 'A-scopes' displayed in *Radan* (Fig. 2.2a). Phase inversion is rare, and there are few internal reflectors at John Evans Glacier, so the bed reflection was generally easily identifiable and simple to follow between traces. To convert travel time to ice thickness it was assumed that the radar wave travelled across the glacier surface at 0.300 m ns^{-1} (speed of light), and that it travelled through the ice at 0.171 m ns^{-1} . The velocity through ice ($0.1711 \pm 0.0031 \text{ m ns}^{-1}$) was determined from 12 common mid-point surveys on John Evans Glacier in 1999, and equates to a real dielectric constant of 3.074 (Copland and Sharp, 2000). Since the oscilloscope was air-wave triggered, the time for the air wave to cross between the transmitter and receiver was added to the time between the peak of the air and bed waves to determine the final ice thickness. The bed and air wave peaks are identifiable to within ± 2 samples (i.e., $\pm 19.5 \text{ ns}$ for most surveys), which equates to an ice thickness of $\pm 1.7 \text{ m}$ for a two-way travel path. Errors in ice depth measurements also arise from uncertainty in the location of a reflector (e.g., due to spatially variable radio-wave velocity in ice), and are typically quoted as one-tenth of the transmitted

wavelength (Bogorodsky et al., 1983). This equates to ± 1.7 m for the most commonly used centre frequency of 10 MHz, ± 3.4 m for a centre frequency of 5 MHz, and ± 0.85 m for a centre frequency of 20 MHz.

The bed topography was determined by subtracting the ice thickness from the surface elevation at each trace location. A DEM of the glacier bed with the same 25 m grid spacing as the surface DEM was produced by interpolating between the 3200 bed elevations derived from the radio-echo sounding traces, and 6700 bedrock elevations along the glacier edge derived from the surface DEM. The interpolation was completed with a TIN (triangulated irregular network) for the surface and bed DEMs, which maintains the elevations of the original data points. These DEMs are used to calculate the subglacial hydraulic potentials and associated subglacial flow reconstructions that are discussed in Section 2.4.3. The bed DEM is also used in the calculation of the bed slopes discussed in Section 2.4.2. The estimated accuracy of the surface DEM is 6 m, while the accuracy of the bed DEM is dependent on both the accuracy of the surface DEM and the errors in the ice thickness measurements.

In our ice thickness calculations, we assumed that the bed reflection occurred from a point directly below the mid-point between the receiver and transmitter (which were separated by up to 20 m). Ice thickness was determined from the angular distance from the transmitter to the mid-point at the bed, which results in an overestimation of depth compared to the straight-line distance from the mid-point on the surface to the mid-point at the bed. This overestimation is small compared to other errors, however, and is <0.5 m when the ice is 100 m thick, and <0.2 m when the ice is 250 m thick. In addition, the assumption that the bed reflection occurs from the mid-point at the bed is probably not always true, particularly in areas of steep topography where reflections from valley side-walls may occur before reflections from the underlying glacier bed. These effects are commonly reduced via migration, but this was not possible at John Evans Glacier due to the generally irregular spacing of measurement points. We estimated errors in the ice thickness measurements by performing ray-tracing along representative transects from the glacier terminus, upper ablation area, and accumulation area. As outlined by Rabus and Echelmeyer (1997), the bed along a given profile is assumed to be the envelope of intersecting ellipses with the transmitter and receiver as focal points. Although ray

tracing is a crude method (e.g., it assumes that reflections occur only from topography along the transect), it provides an estimate of the errors in our ice thickness determinations. These errors are generally +/- 10%, although they rarely reach +/- 20% in areas of very steep topography (approximately 5% of points are in this kind of terrain). These errors are not significant in our discussion as they do not affect the general location of subglacial valleys and ridges, and they do not change the location of spatially contiguous areas of high residual bed reflection power discussed later. Indeed, migration would only serve to increase the values of high residual bed reflection power as it would have the effect of increasing ice thickness in areas of steep basal topography.

2.3.2 Returned power from radio-echo sounding

Following the work of Gades (1998) and Gades et al. (2000), the internal reflection power (IRP) and bed reflection power (BRP) were calculated for all the traces recorded at John Evans Glacier from (Fig. 2.2):

$$\text{Received power} = \int_{t_1}^{t_2} (s(t))^2 dt \quad (1)$$

where s is the amplitude of the signal and t is time. For BRP, t_1 is taken as 100 ns before the bed peak and t_2 as 400 ns after the bed peak. This time window encompasses all the power returned from the glacier bed. For IRP, a variable time window extending from 600 ns after the air wave peak to 100 ns before the bed peak was used (Fig. 2.2a). This excluded the noise from the air and ground waves at the start of each trace, as well as returns from the glacier bed.

The use of a variable time window differs from the approach of Gades (1998) and Gades et al. (2000), who used a fixed time window to calculate IRP. This approach could not be used at John Evans Glacier because the window between the surface and bed waves approaches zero at small ice thicknesses (a problem never encountered by Gades (1998) or Gades et al. (2000)). To standardise our measurements, the total IRP was therefore divided by the length of the specified time window. This approach was also applied to calculations of BRP. Unfortunately, because dielectric loss increases with

depth, this may result in a systematic bias in the standardised IRP values, which will tend to be relatively low where the ice is very thick, and relatively high where it is thin.

Features such as crevasses produce large englacial reflections and are readily identifiable as regions of high IRP even in thick ice. Such large englacial reflections could cause a reduction in the amount of energy that reaches the glacier bed. Because our goal is to map spatial variations in BRP that may be associated with variations in the properties of the glacier bed, we rejected all traces that displayed the presence of strong englacial reflectors. This was done by defining a threshold IRP value ($2 \text{ mV}^2 \text{ ns}^{-1}$) that identified all locations where crevasses were known to exist (Copland and Sharp, 2000). By this criterion, approximately 7.5% of the original traces were excluded from further analysis. Tests with IRP threshold values between 1 and $10 \text{ mV}^2 \text{ ns}^{-1}$ made no significant difference to the final results.

Elsewhere the IRP was uniformly low without a clear spatial pattern. This makes it unlikely that IRP affects the patterns in BRP in the remaining traces, particularly since the BRP was typically more than an order of magnitude greater than the IRP in these traces (Fig. 2.3). Variability in bed power in the remaining traces is assumed to be due to differences in ice thickness and bed properties, rather than to the presence of englacial features or englacial scattering.

For a flat, homogeneous ice sheet resting on a smooth horizontal rock bed, the main controls on received power are described by the radar equation (Bogorodsky et al., 1983):

$$P_r = \frac{P_t}{4\pi[2(H+h)]^2} G_t A_r q \frac{1}{L} \quad (2)$$

where P_r and P_t are the received and transmitted power, H is the height of the antenna above the ice surface, h is the ice thickness, G_t is the transmitter gain, A_r is the effective area of the receiving antenna, q is the refraction gain, and L the losses involved:

$$L = L_a (L_r)^2 L_R \quad (3)$$

where L_A is the dielectric loss by two-way propagation through the ice, L_T is the transmission loss through the surface, and L_R is the reflection loss at the base of the ice sheet. These can be described by:

$$L_A = \exp(2\kappa h); \quad L_T = \frac{1}{(1-|R'|^2)}; \quad L_R = \frac{1}{|R''|^2} \quad (4)$$

where κ is the dielectric loss in nepers per meter and $|R'|^2$ and $|R''|^2$ are the power reflection coefficients at the surface and the base, respectively.

Although the conditions at John Evans Glacier do not meet many of the assumptions associated with this equation, and P_r is not numerically equivalent to BRP, these equations nevertheless illustrate the main controls on BRP. We assume that losses due to polarization and scattering at the ice/bed interface are minimal and/or constant (Gades, 1998), and that the antenna characteristics and surface coupling were constant for all traces recorded at a particular frequency. The remaining controls on BRP are then h and L . Therefore, if we can determine the apparent attenuation with depth as the radar wave passes through the glacier, the remaining variability in BRP will be a function of variability in bed conditions.

2.3.3 Rate of apparent attenuation with depth

To determine the rate of apparent attenuation with depth for John Evans Glacier, BRP was plotted against ice thickness for all traces with IRP $< 2 \text{ mV}^2 \text{ ns}^{-1}$ (Fig. 2.4a). Apparent attenuation describes any way in which radar power decreases with depth in the glacier, and can be due to factors such as geometric spreading, scattering, and dielectric absorption. Individual plots were produced for the different centre frequencies, because lower frequencies are less strongly attenuated in ice and therefore produce different reflection characteristics. These plots contained 2140 points for the 10 MHz traces, 525 points for the 5 MHz traces, and 303 points for the 20 MHz traces. Most of the discussion in this paper focuses on the results from the 10 MHz traces due to the large number of records at this frequency, and the fact that similar spatial patterns in BRP were displayed

in the 5 MHz and 20 MHz records. The 10 MHz traces recorded over the glacier terminus were also isolated and analysed independently to provide detailed information for a small area where the englacial temperature distribution is likely quite uniform (>450 traces within an area of <1 km²; Figs. 2.4b and 2.5b). Attenuation rate increases with ice temperature, so spatial differences in englacial thermal structure will likely cause variability in the rate of loss with depth.

A least squares best-fit curve through each plot provides the predicted BRP for a given ice thickness and transmitter frequency. Both exponential and power best-fit curves described the attenuation rate with depth, although exponential fits were chosen for our final calculations as they had slightly higher r^2 values. The r^2 value of 0.842 for the glacier terminus plot was particularly high (Fig. 2.4b), and provides a solid base for the interpretations of variability in BRP_r from this area. The best-fit curves for the glacier-wide plots had lower r^2 values (0.689 and 0.691), which is consistent with the suggestion that variability in englacial temperatures is greater over the entire glacier than over the terminus area alone. It is therefore necessary to determine whether the scatter of data points about the best-fit curve for the whole glacier arises because the curve does not adequately describe the relationship between BRP and ice thickness, or because there are spatial variations in ice temperature, bed properties, or both.

To compare measured to predicted BRP in areas with different ice thicknesses, the residual bed reflection power (BRP_r) was calculated from (Gades, 1998):

$$BRP_r = \frac{BRP_{measured}}{BRP_{predicted}} - 1 \quad (5)$$

To evaluate whether the observed spatial patterns in BRP_r (Figs. 2.6a and 2.7) are due to the failure of the best-fit curve to adequately describe the relationship between BRP and ice thickness, we plotted BRP_r against ice thickness for the whole glacier (Fig. 2.8). It is clear that there is no systematic relationship between the two variables, so we conclude that BRP_r is determined by the ice temperature and/or the bed properties. If ice temperature is the dominant control, we expect low BRP_r in areas where glacier ice is relatively warm and high BRP_r in areas with relatively cold ice. If bed properties are the

dominant control, we expect high BRP_r in areas where the bed is especially reflective and low BRP_r where bed reflectivity is low.

2.4 RESULTS AND DISCUSSION

2.4.1 Distribution of warm and cold ice

On a glacier-wide scale there is a marked contrast between the generally negative BRP_r over the upper half of the glacier, and the generally positive BRP_r over the lower half of the glacier (Fig. 2.6a). The division between the two areas correlates closely with the location of the equilibrium line at ~ 750 m asl. An important question is whether these patterns are due to differences in englacial conditions (i.e., attenuation related) or basal conditions (i.e., reflection related). If they are attenuation related, we would expect to see negative BRP_r where the englacial ice is relatively warm, and positive BRP_r where it is relatively cold (due to the increase in attenuation rate with ice temperature). This would suggest that ice in the ablation area is generally colder than that in the accumulation area. This suggestion directly contradicts the results of measurements of the englacial temperature distribution within nearby White Glacier, Axel Heiberg Island (Blatter, 1987), and Laika Ice Cap, Coburg Island (Blatter and Kappenberger, 1988). These show that warm ice is found only in the ablation areas of these two glaciers. It is also inconsistent with hydrochemical evidence for subglacial drainage of supraglacially-derived meltwaters beneath the lower ablation area of John Evans Glacier (Skidmore and Sharp, 1999).

Consequently, a more likely explanation is that the BRP_r patterns are related to changes in basal conditions. Since water has a very high dielectric constant relative to both ice and rock, and water can only exist at the bed where the ice is warm, the BRP_r patterns are consistent with the suggestion that there is cold basal ice in the accumulation area (negative BRP_r), and warm basal ice in the ablation area (positive BRP_r) (Fig. 2.6a). In the ablation area, exceptions to this pattern occur along the glacier margin and in the vicinity of a pronounced bedrock ridge, where the ice is thin and BRP_r values are low. The ice is likely cold in these locations due to the high englacial temperature gradient that would effectively remove geothermal heat.

A faint but continuous internal reflector that is present over much of the glacier terminus (Fig. 2.5a) provides further information about the thermal structure of the glacier. This reflector occurs approximately 20 m above the glacier bed in all traces over the centre of the terminus region. Close to the glacier margin, however, it rapidly approaches the bed and then disappears altogether (Fig. 2.5b). Since the internal reflector is present only in areas with high BRP_r , we interpret it as the boundary between cold ice above and warm ice below. A faint reflector is expected at this boundary because warm ice has a slightly higher dielectric constant ($\epsilon_i \sim 3.3$) than cold ice ($\epsilon_i \sim 3.1$) (Macheret et al., 1993). Similar internal reflecting horizons have been identified in radio-echo sounding records from many other polythermal glaciers. These have also been interpreted as the boundary between warm and cold ice (e.g., Dowdeswell et al., 1984; Bamber, 1987; Kotlyakov and Macheret, 1987; Holmlund and Eriksson, 1989; Björnsson et al., 1996; Hamran et al., 1996; Moorman and Michel, 2000). On White Glacier, Axel Heiberg Island, a warm ice layer of up to 40 m thickness was identified from temperature measurements in 32 boreholes (Blatter, 1987). As at John Evans Glacier, this layer occurred in the centre of the ablation zone and its upper surface was generally parallel to the basal topography, except where the layer decreased in thickness close to the glacier margins. Similar ice temperature measurements (or thermal modelling) would be necessary to confirm that the internal reflector at John Evans Glacier marks the boundary between warm and cold ice.

It is possible that the presence of the internal reflecting horizon in the glacier terminus region could affect the strength of the bed returns in this area, but we think this is unlikely for two reasons. First, the power of this reflection is always at least two orders of magnitude less than the BRP. Second, if the internal reflector significantly reduced the BRP, one would expect the BRP_r to be low over the centre of the terminus, but it is in fact high in this region. The internal reflecting horizon was not observed in the upper part of the ablation area, even though BRP_r is high there. This is probably because the 0°C isotherm is at the glacier bed in this area. Flow acceleration and channelling around the bedrock ridge are likely to play a role in generating the warm layer over the terminus.

2.4.2 Variations in BRP_r within areas of warm ice

In this section we investigate the hypothesis that variations in BRP_r within the warm-based areas of the ablation zone are a reflection of variations in subglacial hydrology. Figure 2.6a shows the large-scale variations in BRP_r calculated from the exponential best-fit curve for the entire glacier (Fig. 2.4a), while Fig. 2.7 plots BRP_r within the inferred area of warm-based ice near the terminus. In this plot, BRP_r is derived from the exponential best-fit curve to data collected in the terminus area only (Fig. 2.4b). The terminus plot (Fig. 2.7) shows differences in BRP_r in an area where there is little variability in ice thickness, englacial properties, thermal structure and bed slope. This homogeneity of properties gives us confidence that spatial variations in BRP_r over the terminus are caused by changes in the nature of the ice/bed interface.

On the glacier-wide scale, BRP_r is particularly high in three areas (A and B in Fig. 2.6a, C in Figs. 2.6a and 2.7). Area A is defined by at least 100 individual traces, and extends from near the western glacier margin to the upstream edge of the bedrock ridge. Topographically, this area encompasses a valley bottom, with highest BRP_r values (up to 30) in the overdeepened eastern end of the valley. The overdeepening contains ice up to 300-400 m thick, and its base is up to 150 m lower than the lowest point of the subglacial bedrock ridge directly downstream.

The high BRP_r in area B occurs in a subglacial valley to the south of the bedrock ridge (Fig. 2.6b). Values of BRP_r are not as high as in area A, but BRP_r is still up to 10 times greater than predicted. High BRP_r values in this area are seen in surveys at both 10 MHz and 20 MHz, and are defined by more than 50 individual traces. This area is also overdeepened by up to 50 m in a location where ice thicknesses are ~250 m, with the overdeepening in close proximity to the area of highest BRP_r .

In area C, BRP_r becomes increasingly positive towards the glacier terminus, with values of BRP_r up to 10 times higher than predicted in the areas furthest downstream. Once again, these values are well defined by more than 100 traces over different transects. Unlike areas A and B, however, the glacier terminus is not overdeepened.

Within the glacier terminus region there are two narrow, elongated areas with high BRP_r (D and E in Fig. 2.7). These areas are also well defined by traces over several different transects, and have BRP_r values up to 10 times higher than predicted. The

downstream end of area D is close to the location of a large artesian fountain observed on the glacier surface in 1998. The fountain reached heights of up to 5 m, and brought large quantities of solute-rich, turbid subglacial water to the glacier surface. The fountain developed at the onset of the annual outburst flood on June 29, and was active for 13 days. Outflow of turbid, solute-rich water at the ice/bed interface also began on June 29 (at Outflow₁ on Fig. 2.7) and continued throughout the melt season.

The upstream end of area E coincides with an area where a large marginal stream with low solute concentrations disappears beneath the glacier, and is unusual because it cuts across an area of low BRP_r, where the ice is inferred to be cold-based (marked by a triangle in Fig. 2.7). This elongated area of high BRP_r follows the western edge of the study area and is virtually continuous to the downstream edge of the area surveyed. The stream that emerges at Outflow₂ (Fig. 2.7) lies directly downglacier from this location, and is much less solute-rich than the stream at Outflow₁. This implies less time for contact between the water and glacier bed at Outflow₂, and is consistent with the suggestion that the ice marginal stream that enters the glacier at the upstream end of area E provides at least some of the water to this outlet.

There are several potential explanations for these high BRP_r areas. One possibility is that we have overestimated the rate of attenuation of the radar energy with depth (which would make the BRP_r values too high). This explanation is unlikely, however, as ice thicknesses similar to those found in areas A, B and C occur in other parts of the glacier, yet high BRP_r values are not seen in these regions. In addition, our entire range of estimates of dielectric absorption produce essentially the same patterns. We experimented with a power best-fit curve (Fig. 2.4a) for plotting Fig. 2.6a, as well as applying the terminus best-fit curve (Fig. 2.4b) to the data plotted in Fig. 2.6a, but no significant differences in the BRP_r patterns were found. Spatial variations in the thermal structure of the ice may also cause errors when calculating the attenuation rate based on values from different parts of the glacier. The inclusion of data points collected in cold ice would result in the underestimation of radar attenuation in warm ice. This would underestimate BRP_r in warm ice areas, which means that correction for this effect would only serve to accentuate the areas of high BRP_r that are the focus of our discussion.

A second possibility is that high BRP_r is the result of multiple reflections (e.g., from off-nadir locations) that are included within the window over which BRP is calculated, and which therefore increase the apparent power returned from the glacier bed. This could be a particular problem in overdeepened areas where there is much surrounding topography. Indeed, the largest peak in BRP_r in Fig. 2.3d is close to a multiple reflection at the glacier bed in Fig. 2.3a. The BRP_r remains high well away from areas of multiple reflections, however, and in general there are very few multiple reflections in the areas of high BRP_r . For example, the bed is virtually flat across the glacier terminus, giving little potential for multiple reflections in an area where large variations in BRP_r are observed.

Another possibility is that BRP_r is influenced by the incidence angle of the returned bed wave, with lower powers where bed slopes are steep. This could provide an explanation for the high BRP_r values in the base of valleys and overdeepenings. To quantify the influence of bed slope on BRP_r , we calculated the mean bed slope over a 200 x 200 m area centred on grid points with 100 m spacing across the glacier (Zevenbergen and Thorne, 1987). This area encompasses the region from which most bed returns are expected to occur. For each radio-echo sounding measurement, the bed slope of the nearest grid point was plotted against BRP_r for every point with $IRP < 2 \text{ mV}^2 \text{ ns}^{-1}$ (Fig. 2.9). The best-fit curves show no significant or consistent correlation between BRP_r and bed slope at any frequency. The r^2 values are 0.003 at 5 MHz, 0.051 at 10 MHz and 0.054 at 20 MHz. Similar results were obtained when BRP was plotted against bed slope (i.e., when ice thickness was not taken into account). In addition, large changes in BRP_r occur across the glacier terminus where there is little change in bed slope. From these observations, we conclude that although bed slope may affect individual BRP_r values, it does not have an effect on the spatially contiguous BRP_r patterns that are the focus of our discussion.

Having eliminated these explanations, we argue that the observed variations in BRP_r are real and are related to differences in conditions at the ice/bed interface. This argument is based upon the following observations: (i) the major variations in BRP_r appear to occur within an area of warm-based ice, and (ii) the regions of highest BRP_r in the glacier terminus area are found in close proximity to the observed and predicted

locations of drainage elements. Since subglacial hydrology is often cited as an influence on bed reflection power (Hamran et al., 1996; Bentley et al., 1998; Gades, 1998; Gades et al., 2000), we now evaluate the hypothesis that the BRP_r patterns are related to spatial variations in the amount or distribution of water at the glacier bed.

2.4.3 Subglacial drainage reconstruction

We determined likely subglacial water routing at John Evans Glacier by calculating flow accumulation patterns from gridded values of subglacial hydraulic potential (Φ) (Shreve, 1972; see Copland and Sharp, 2000, for details):

$$\Phi = \rho_w g B + f \rho_i g (H - B) \quad (6)$$

where ρ_w and ρ_i are the densities of water and ice, respectively, g is the acceleration due to gravity, B is the bed elevation (Fig. 2.6b), f is the ratio of the subglacial water pressure to the ice overburden pressure, and H is the surface elevation. Water flows from areas of high to low hydraulic potential, and normal to the equipotential contours. Drainage reconstructions were made using values of f from 0 to 1 (i.e., from flow under atmospheric pressure to flow under pressures as high as ice overburden), but no significant differences were found in the predicted flow routing. This is due to the strong topographic control on subglacial water flow beneath John Evans Glacier, particularly around the subglacial bedrock ridge.

Figure 2.10 shows the subglacial drainage reconstruction. Drainage pathways are shown only for those areas of the glacier where ice is inferred to be warm-based because water cannot exist where the basal ice is cold. Figure 2.7 shows the relationship between the predicted pattern of water flow over the glacier terminus, and the distribution of BRP_r. The drainage reconstruction does not take into account the location of point water inputs to the glacier bed such as crevasses and moulins, but it nevertheless provides a general idea of the likely flow routing.

For areas A and B in Fig. 2.6a, there is a strong correlation between the areas of highest BRP_r and areas where water is predicted to flow along valley bottoms and accumulate in overdeepenings (Fig. 2.10). These overdeepenings are natural sinks for

water originating from upstream areas, and provide a focus for water flow across the glacier bed. Hooke and Pohjola (1994) proposed that most water flows englacially across overdeepenings, but this seems unlikely at John Evans Glacier due to the dominance of cold ice throughout most of the ice thickness, and the lack of deep englacial reflectors in the radio-echo sounding returns.

Lower in the ablation area, high BRP_r in area C (Figs. 2.6a and 2.7) may reflect the accumulation of water behind the glacier terminus, where ice is frozen to the bed. Outburst floods occur on an annual basis from the terminus of John Evans Glacier, and can last from days to weeks. The first water to be released during these floods is highly turbid and solute-rich (electrical conductivity (EC) $>400 \mu\text{S cm}^{-1}$), and contains relatively high concentrations of ionic species that are products of silicate mineral weathering (Skidmore and Sharp, 1999). After the initial release, there is a rapid decrease in EC, which suggests that water which has been stored at the glacier bed for long periods is driven out of the subglacial drainage system at the onset of the annual outburst event, and that more dilute water derived from recent surface melting is flushed through the system later in the summer.

Beneath the glacier terminus, subglacial water flow is predicted to occur along two main pathways that correlate closely with the narrow, elongated areas of high BRP_r (D and E; Fig. 2.7). As discussed in Section 2.4.2, field observations also suggest that subglacial flow occurs in these areas. During the melt season water enters the glacier in close proximity to the upstream end of area E, and exits it near to the downstream ends of areas D and E.

Based on the close correlation between areas of high BRP_r , and the observed and predicted locations of subglacial drainage pathways, it seems likely that there is a relationship between spatial variations in BRP_r and some parameter that describes the distribution of water at the glacier bed. Possible parameters could include the presence/absence of water, the thickness of a basal water layer, the location of major drainage channels, or the volume of water contained within basal sediment. This relationship between BRP_r and water distribution at the glacier bed most likely arises because the dielectric constant of water (88 at 0°C) is much higher than that of any other naturally occurring subglacial material. For example, common mid-point surveys show

that John Evans Glacier ice has a mean dielectric constant of 3.1 (Copland and Sharp, 2000), while the dielectric constant of carbonates, the dominant bedrock in the John Evans Glacier catchment, (Kerr, 1972), is 6. A wet bed will therefore produce a higher BRP_r than a dry frozen bed for the same subglacial material. Spatial variability in BRP_r can also be altered by factors such as basal roughness and the electrical conductivity of basal materials. However, we do not believe that spatial variations in the solute content (i.e., electrical conductivity) of subglacial water are a major control on the observed patterns of BRP_r . In general, we would expect an inverse relationship between the flux of water in subglacial drainage systems and the solute content of the water. Thus, if solute content were the dominant control on BRP_r , one would expect to see an association between areas of low BRP_r and the observed and predicted locations of major drainage pathways. This is the opposite of what is observed (Fig. 2.7).

2.5 CONCLUSIONS

It appears that it may be possible to infer the thermal conditions and subglacial water distribution beneath a polythermal glacier from the occurrence of an internal reflecting horizon and the spatial pattern of BRP_r . Our results suggest that the pattern of BRP_r is influenced by the distribution of warm and cold areas of the glacier bed, and by the location of individual drainage pathways and areas where water accumulates at the glacier bed. The occurrence of an internal reflector likely reflects the transition between cold ice above and warm ice below.

Data collection by radio-echo sounding is relatively rapid and inexpensive, and can provide detailed information about subglacial properties over a large area. The method is ideally suited to polythermal glaciers due to their low englacial water content and low englacial scattering compared to temperate glaciers. We expect that the method will work best on glaciers where there are marked variations in hydrology and thermal regime, and where an intensive fieldwork program can be undertaken to fully sample these conditions.

2.6 BIBLIOGRAPHY

Bamber, J.L. 1987. Internal reflecting horizons in Spitsbergen glaciers. *Ann. Glaciol.*, **9**, 5-10.

Bentley, C.R., Lord, N. and Liu, C. 1998. Radar reflections reveal a wet bed beneath stagnant Ice Stream C and a frozen bed beneath ridge BC, West Antarctica. *J. Glaciol.*, **44**(146), 149-156.

Björnsson, H., Gjessing, Y., Hamran, S.-E., Hagen, J., Liestøl, O., Pálsson, F. and Erlingsson, B. 1996. The thermal regime of sub-polar glaciers mapped by multi-frequency radio-echo sounding. *J. Glaciol.*, **42**(140), 23-32.

Blatter, H. 1987. On the thermal regime of an arctic valley glacier: a study of White Glacier, Axel Heiberg Island, N.W.T., Canada. *J. Glaciol.*, **33**(114), 200-211.

Blatter, H. and Kappenberger, G. 1988. Mass balance and thermal regime of Laika Ice Cap, Coburg Island, N.W.T., Canada. *J. Glaciol.*, **34**(116), 102-110.

Bogorodsky, V., Bentley, C. and Gudmandsen, P. 1983. *Radioglaciology*. Dordrecht, Reidel.

Copland, L. and Sharp, M. 2000. Radio-echo sounding determination of polythermal glacier hydrology. In: Noon, D., Stickley, G. and Longstaff, D. (eds.) *Eighth International Conference on Ground Penetrating Radar*. SPIE Vol. **4084**, 59-64.

Dowdeswell, J.A, Drewry, D.J., Liestøl, O. and Orheim, O. 1984. Radio echo-sounding of Spitsbergen glaciers: problems in the interpretation of layer and bottom returns. *J. Glaciol.*, **30**(104), 16-21.

Gades, A.M. 1998. Spatial and temporal variations of basal conditions beneath glaciers and ice sheets inferred from radio echo-sounding measurements. (Ph.D. thesis, University of Washington.)

Gades, A.M., Raymond, C.F., Conway, H. and Jacobel, R.W. 2000. Bed properties of Siple Dome and adjacent ice streams, West Antarctica, inferred from radio-echo sounding measurements. *J. Glaciol.*, **46**(152), 88-94.

Hamran, S.-E., Aarholt, A., Hagen, J., and Mo, P. 1996. Estimation of relative water content in a sub-polar glacier using surface-penetration radar. *J. Glaciol.*, **42**(142), 533-7.

Holmlund, P. and Eriksson, M. 1989. The cold surface layer on Storglaciären. *Geogr. Ann.*, **71A** (3-4), 241-244.

Hooke, R.LeB., and Pohjola, V.A. 1994. Hydrology of a segment of a glacier situated in an overdeepening, Storglaciären, Sweden. *J. Glaciol.*, **40**(134), 140-148.

Kerr, J.W. 1972. Geology, Dobbin Bay, District of Franklin. Scale 1:250,000. *Geol. Surv. Can. Map* 1358A.

Kotlyakov, V.M. and Macheret, Y.Y. 1987. Radio echo-sounding of sub-polar glaciers in Svalbard: some problems and results of Soviet studies. *Ann. Glaciol.*, **9**, 151-159.

Macheret, Y.Y., Moskalevsky, M.Y. and Vasilenko, E.V. 1993. Velocity of radio waves in glaciers as an indicator of their hydrothermal state, structure and regime. *J. Glaciol.*, **39**(132), 373-384.

Moorman, B.J. and Michel, F.A. 2000. Glacial hydrological system characterization using ground-penetrating radar. *Hydrol. Process.*, **14**, 2645-2667.

Narod, B.B. and Clarke, G.K.C. 1994. Miniature high-power impulse transmitter for radio-echo sounding. *J. Glaciol.*, **40**(134), 190-194.

- Oswald, G.K.A. and Robin, G. de Q. 1973. Lakes beneath the Antarctic ice sheet. *Nature*, **245**(5423), 251-254.
- Rabus, B.T. and Echelmeyer, K.A. 1997. The flow of a polythermal glacier: McCall Glacier, Alaska, U.S.A. *J. Glaciol.*, **43**(145), 522-536.
- Robin, G. de Q., Drewry, D.J. and Meldrum, D.T. 1977. International studies of ice sheet and bedrock. *Philos. Trans. R. Soc. London, Ser. B.*, **279**(963), 185-196.
- Shreve, R.L. 1972. Movement of water in glaciers. *J. Glaciol.*, **11**(62), 205-214.
- Siegert, M.J. and Ridley, J.K. 1998. Determining basal ice conditions in the Dome C region of East Antarctica using satellite radar altimetry and airborne radio-echo sounding. *J. Glaciol.*, **44**(146), 1-8.
- Skidmore, M.L. and Sharp, M.J. 1999. Drainage system behaviour of a High Arctic polythermal glacier. *Ann. Glaciol.*, **28**, 209-215.
- Trabant, D.C., Harrison, W.D. and Benson, C.S. 1975. Thermal regime of McCall Glacier, Brooks Range, Northern Alaska. In Weller, G. and Bowling, S., eds. *Climate of the Arctic*. Fairbanks, University of Alaska. Geophysical Institute, 347-349.
- Wadham, J.L., Tranter, M. and Dowdeswell, J.A. 2000. Hydrochemistry of meltwaters draining a polythermal-based, high-Arctic glacier, south Svalbard: II. Winter and early Spring. *Hyd. Proc.*, **14**(10), 1767-1786.
- Woodward, J., Sharp, M. and Arendt, A. 1997. The effect of superimposed ice formation on the sensitivity of glacier mass balance to climate change. *Ann. Glaciol.*, **24**, 186-190.
- Zevenbergen, L.W. and Thorne, C.R. 1987. Quantitative analysis of land surface topography. *Earth Surf. Proc. Land.*, **12**, 47-56.

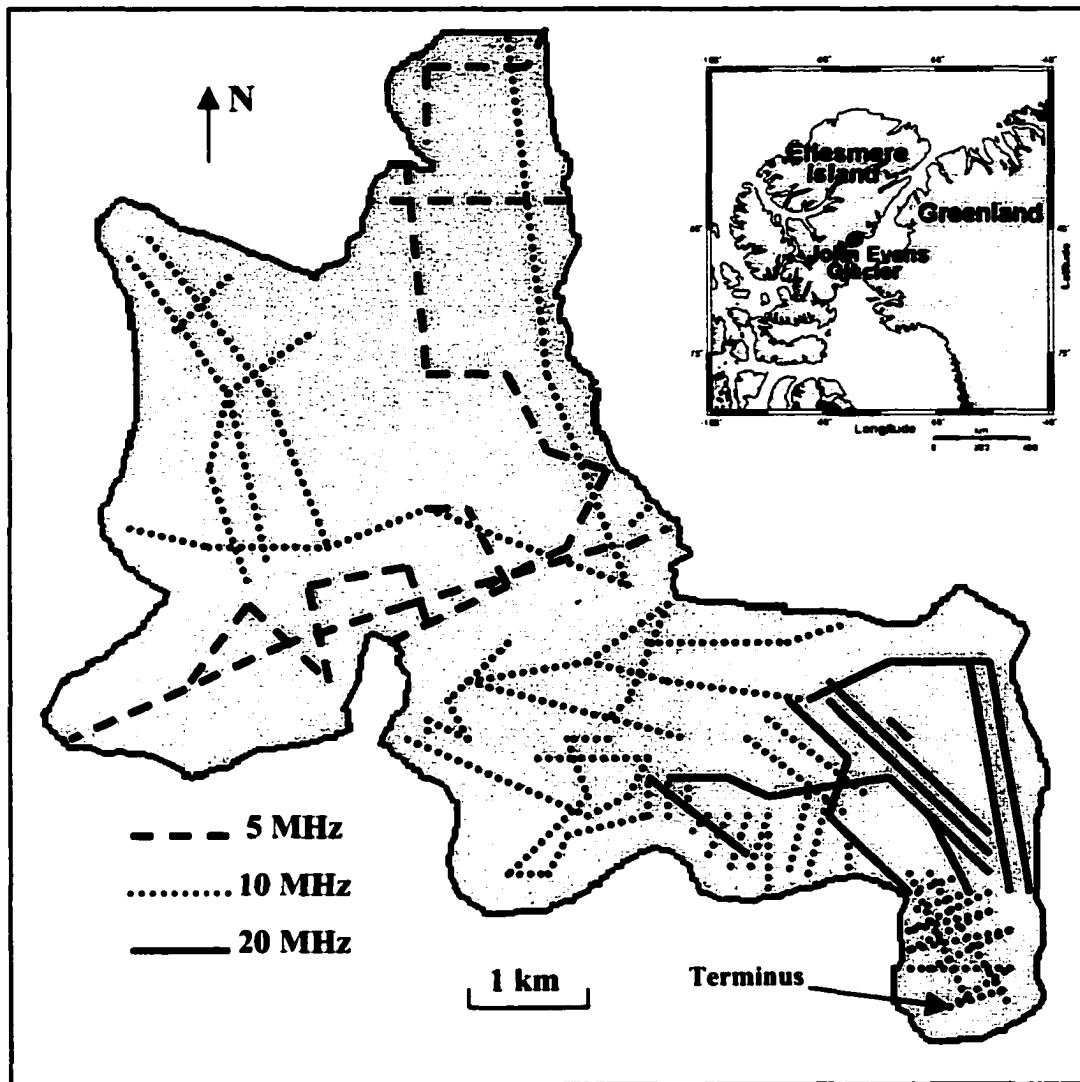


Figure 2.1 Map showing the location of John Evans Glacier and the distribution of radio-echo sounding measurements made for this study

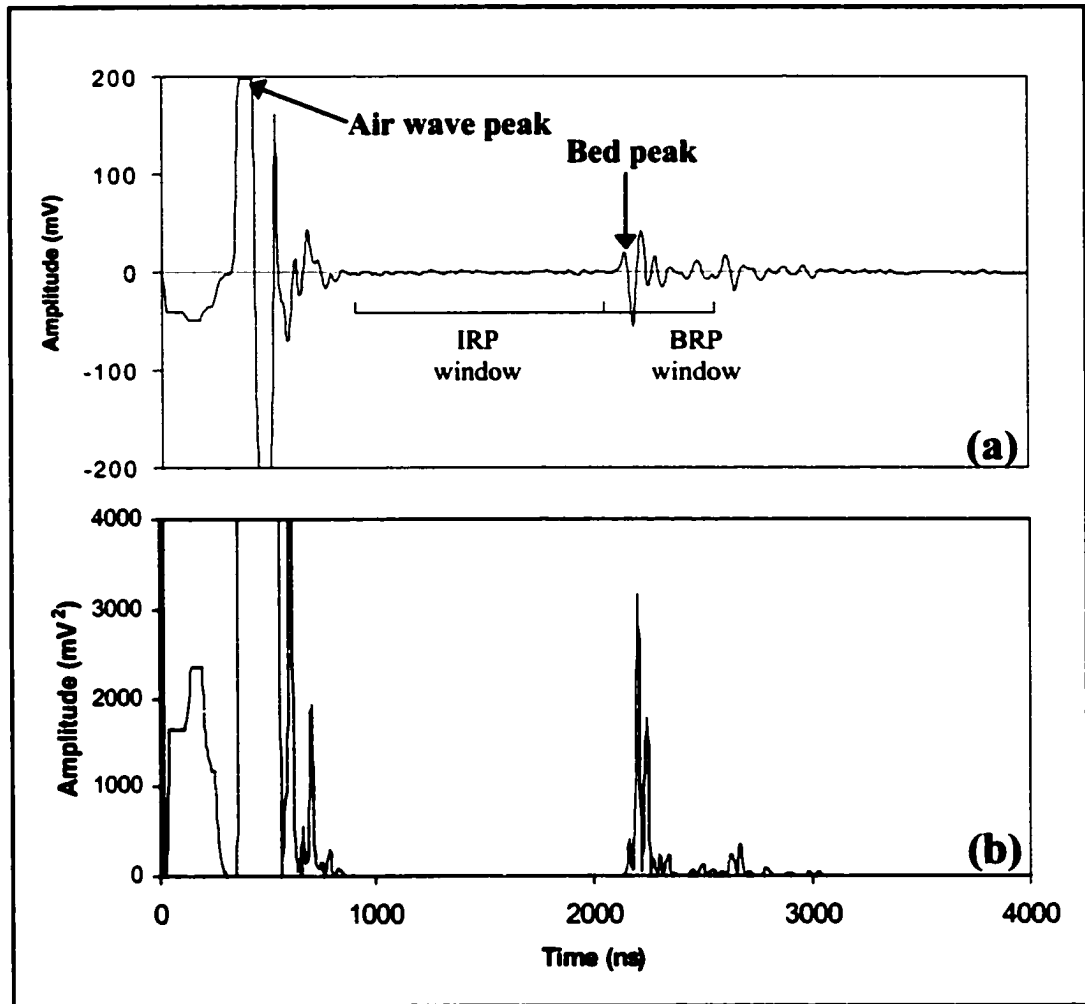


Figure 2.2 (a) A typical radio-echo sounding trace recorded at John Evans Glacier (b) Returned power from the same trace. IRP = internal reflection power, BRP = bed reflection power

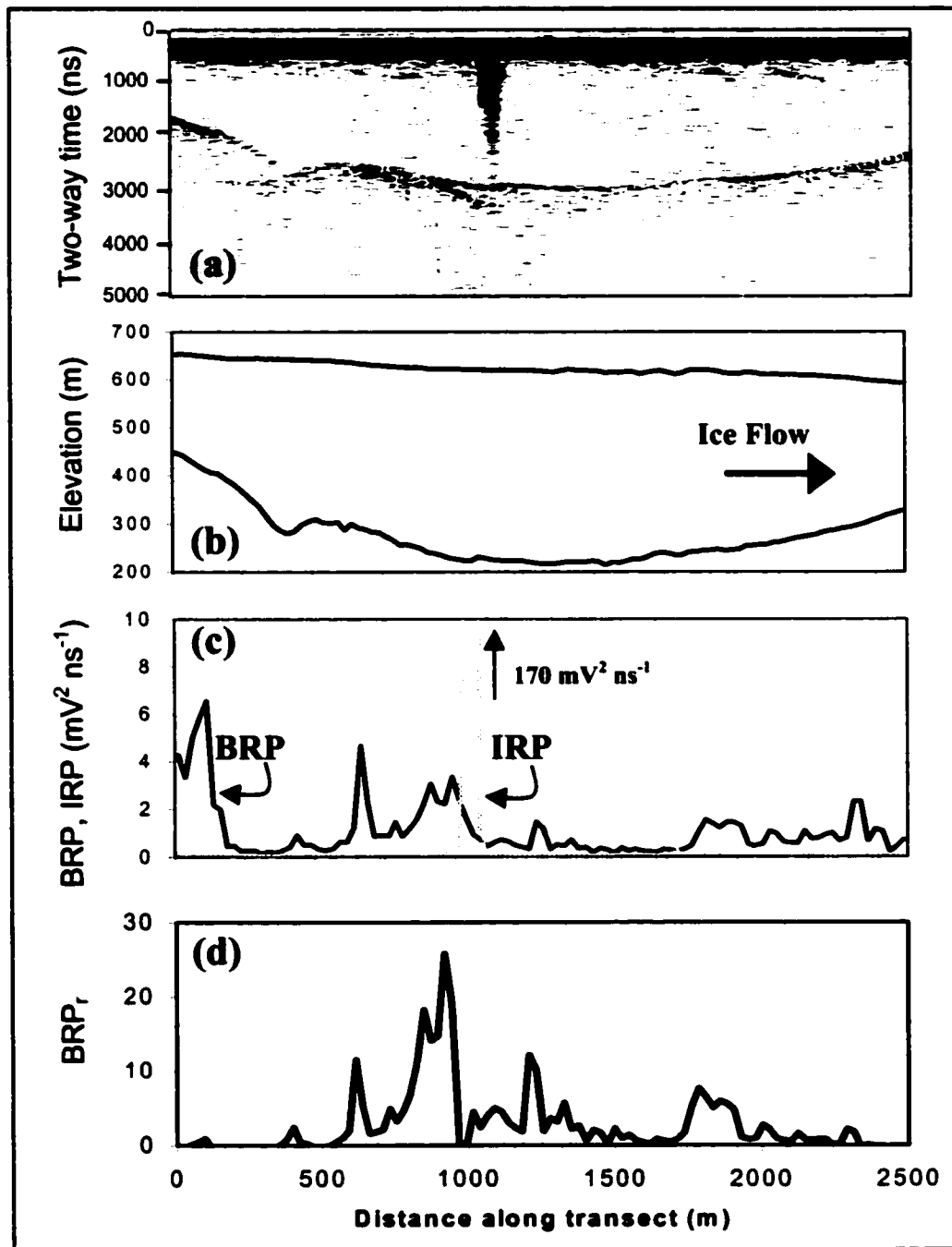


Figure 2.3 (a) Raw radio-echo sounding data for a transect through the centre of Area A in Fig. 2.6 (uncorrected for surface topography). Area of high englacial reflections towards the centre of the transect is probably caused by a crevasse. (b) True surface and bed topography. (c) Bed reflection power (BRP) and internal reflection power (IRP) standardised to $\text{mV}^2 \text{ns}^{-1}$. Note the high IRP where the crevasse is located; traces with an $\text{IRP} > 2 \text{mV}^2 \text{ns}^{-1}$ were removed from further analysis (d) Residual bed reflection power (BRP_r): highest values occur over the overdeepening

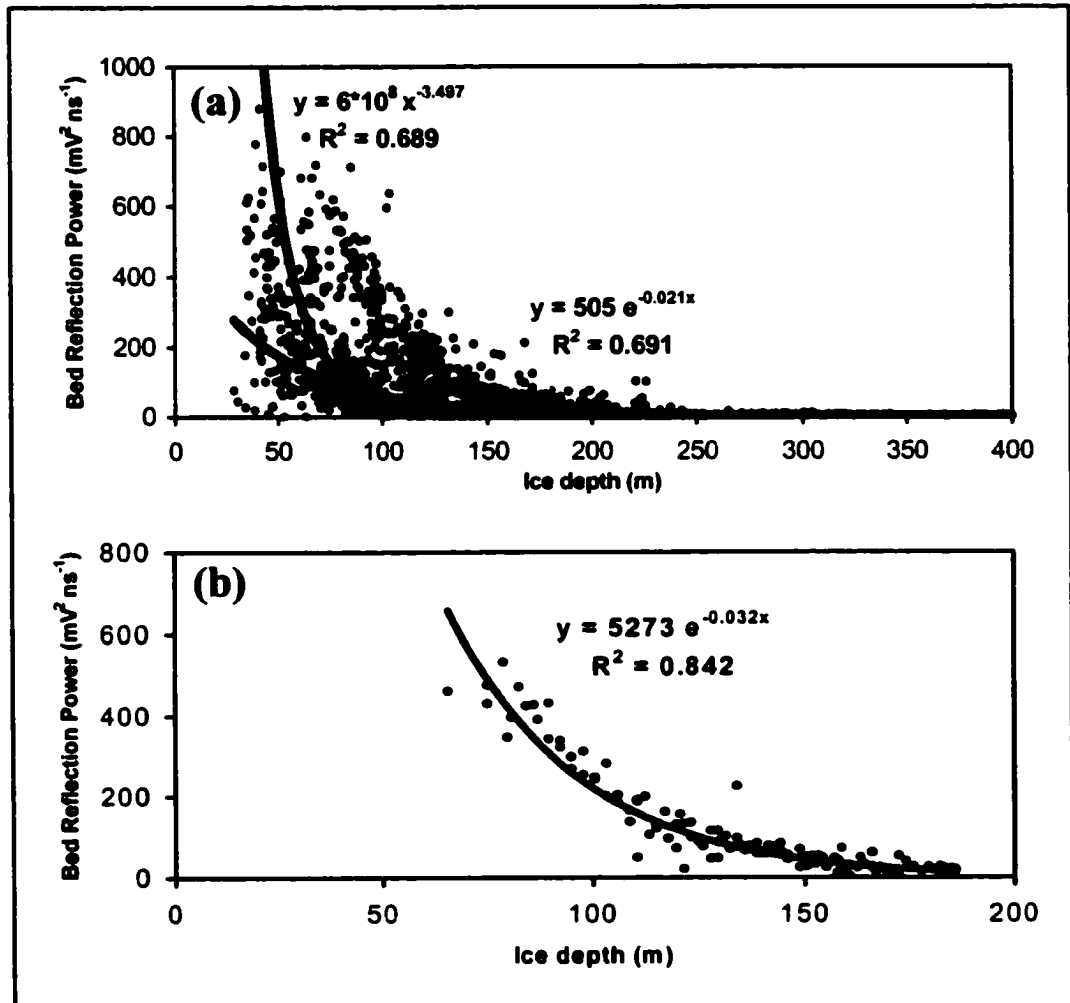


Figure 2.4 (a) Relationship between ice thickness and bed reflection power for all 10 MHz traces with an internal reflection power $< 2 \text{ mV}^2 \text{ ns}^{-1}$ (b) Relationship between ice thickness and bed reflection power for all 10 MHz traces completed over the glacier terminus with an internal reflection power $< 2 \text{ mV}^2 \text{ ns}^{-1}$. Best-fit curves represent the attenuation of radar power with thickness

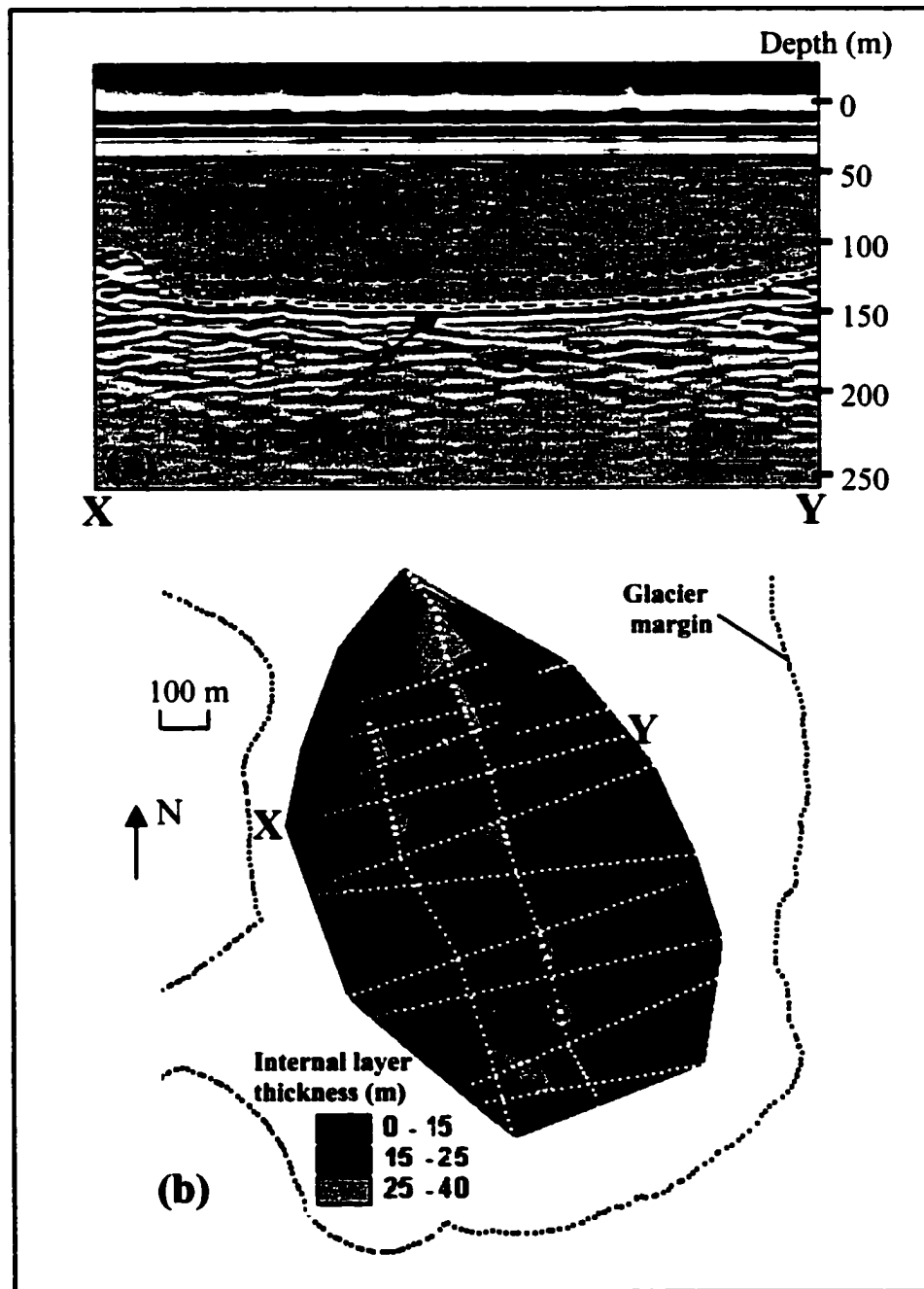


Figure 2.5 (a) An example of a radio-echo sounding transect across the terminus of John Evans Glacier (uncorrected for surface topography). The internal reflector is interpreted as the boundary between cold ice above and warm ice below. (b) Thickness and distribution of internal reflecting horizon across the terminus of John Evans Glacier. White dots indicate trace locations, black dots indicate glacier boundary. X and Y mark the ends of the transect displayed in (a)

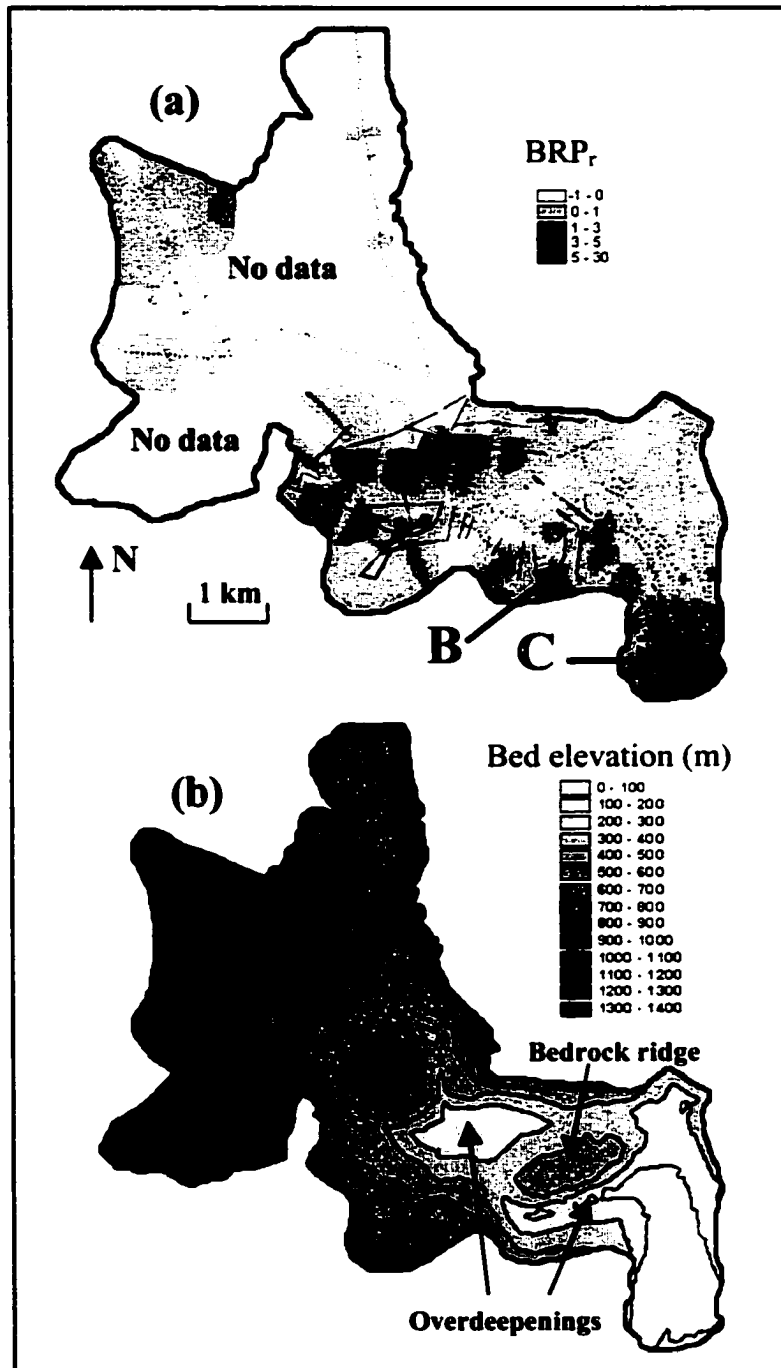


Figure 2.6 (a) A composite map of spatial variability in residual bed reflection power (BRP_r) across John Evans Glacier for surveys at 10 MHz and 20 MHz (black dots mark survey locations). The data from the 20 MHz surveys encompasses the area to the NE of the bedrock ridge shown in Fig. 2.6b (see Fig. 2.1 for details). Areas A, B and C display particularly high BRP_r values and are discussed in the text. (b) Basal topography of John Evans Glacier. Note correlation between valleys/overdeepenings and areas A and B of high BRP_r.

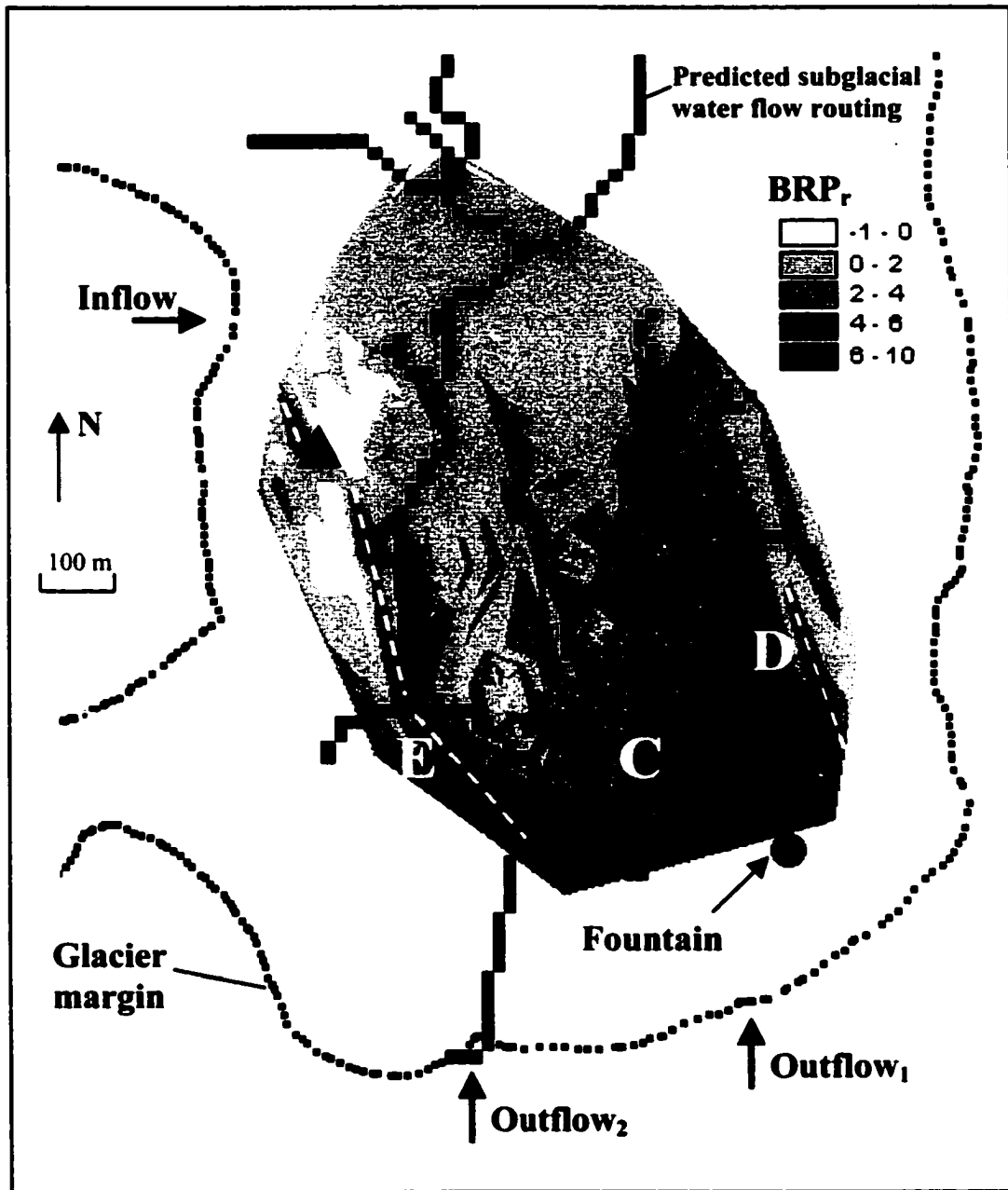


Figure 2.7 Variability in residual bed reflection power (BRP_r) over the glacier terminus, and predicted subglacial water flow routing (marked by heavy black lines). Letters refer to features discussed in the text. Inflow indicates the location where a large marginal stream disappears beneath the glacier; outflow indicates the location of streams which exit from beneath the glacier terminus. Dashed white lines mark elongated areas D and E of high BRP_r . Black triangle marks the location where the elongated area of high BRP_r (area E) crosses an area of low BRP_r .

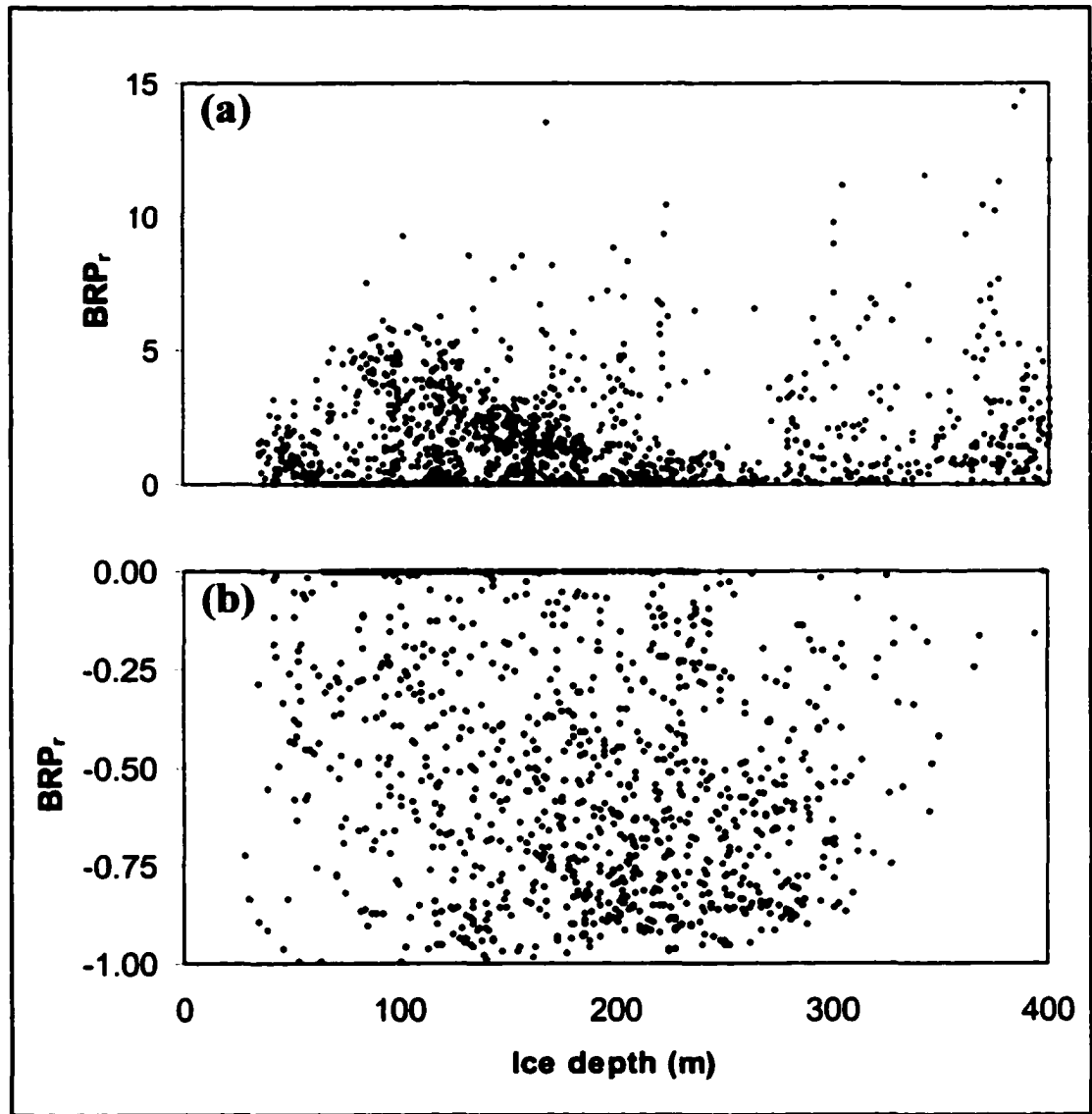


Figure 2.8 Variability in BRP_r with ice thickness: (a) for positive values of BRP_r , (b) for negative values of BRP_r . Positive and negative values are plotted separately because there is no upper limit to the range of positive values, while negative values cannot be less than -1

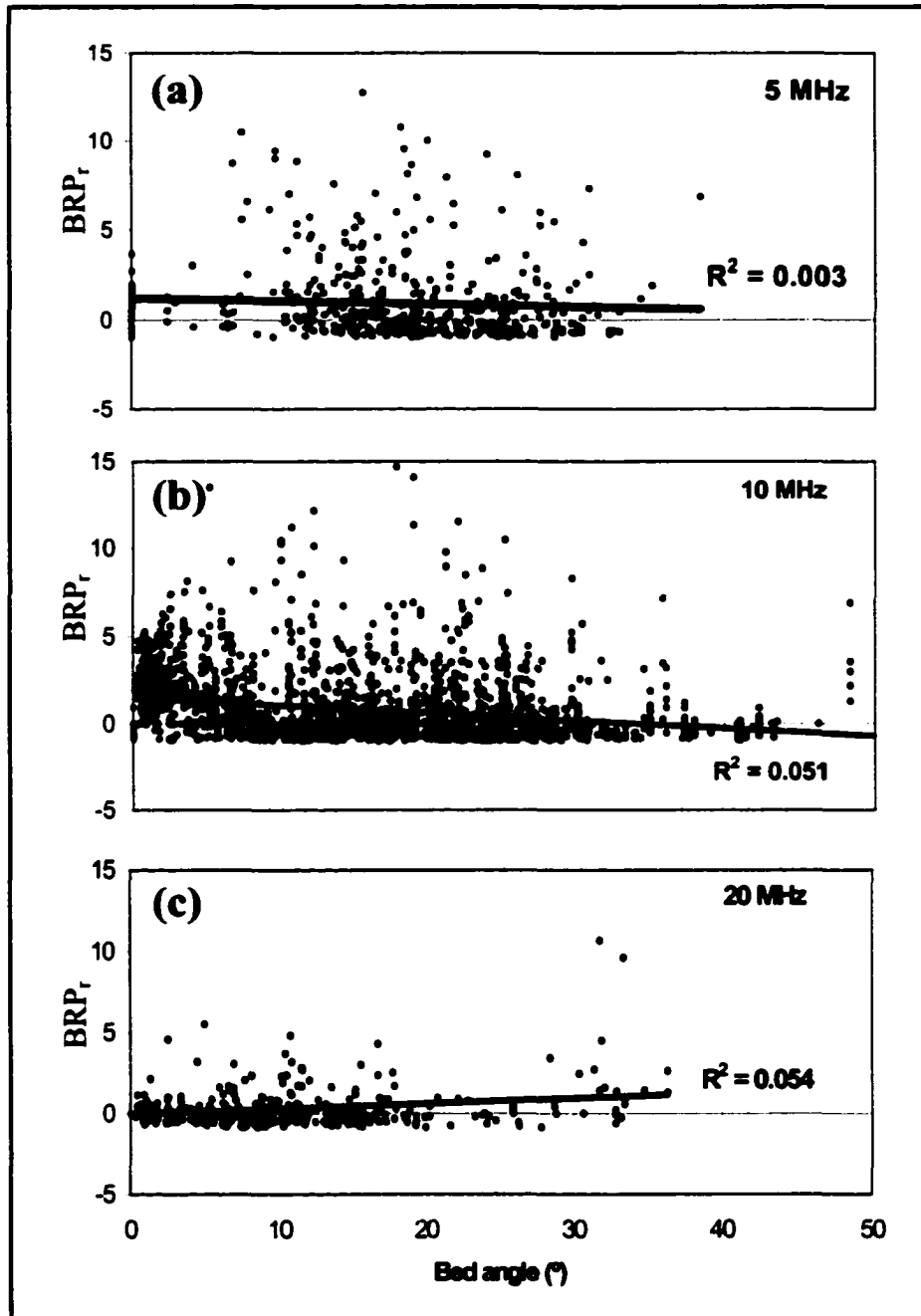


Figure 2.9 Relationship between bed angle and BRP_r for surveys with $IRP < 2 \text{ mV}^2 \text{ ns}^{-1}$ at: (a) 5 MHz. (b) 10 MHz. (c) 20 MHz. Black line shows best fit line for each plot

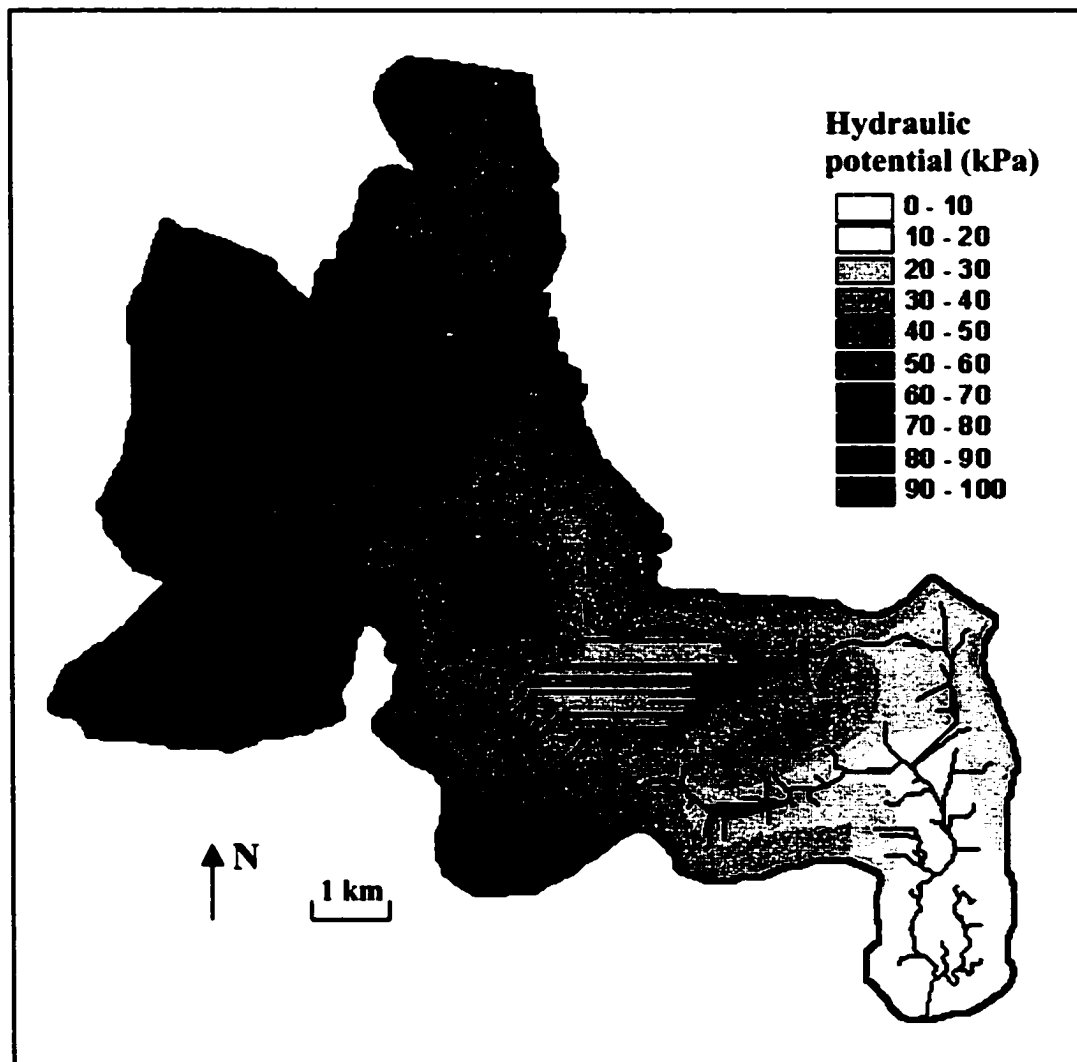


Figure 2.10 Subglacial hydraulic potential and predicted subglacial hydrological flow paths for the ablation area of John Evans Glacier for $f = 1$. Flow is not shown for the accumulation area because the bed is inferred to be cold there

CHAPTER 3

RADIO-ECHO SOUNDING DETERMINATION OF POLYTHERMAL GLACIER HYDROLOGY

3.1 INTRODUCTION

Many studies have demonstrated that water at the bed of a glacier influences ice motion via the influence of subglacial water pressure on basal shear traction (Iken and Bindschadler, 1986; Willis, 1995). Geomorphological evidence and computer models also indicate that subglacial hydrology was a crucial control on the dynamics of the Pleistocene mid-latitude ice sheets (Arnold and Sharp, 1992). High Arctic glaciers exhibit polythermal basal conditions which most closely resemble those found beneath Pleistocene ice sheets (Heine and McTigue, 1996), but little is currently known about their hydrology. Polythermal glaciers contain ice that is both at and below the pressure melting point, with high Arctic glaciers characterized by warm ice that is present only close to the glacier bed in the ablation area (Blatter and Hutter, 1991).

In this paper we discuss three sources of information which radio-echo sounding has provided about the subglacial hydrology of a polythermal glacier: the location of water input points to the glacier interior, the routing of water across the glacier bed, and temporal changes in basal water flow.

3.2 STUDY SITE

John Evans Glacier is a polythermal valley glacier on the east coast of Ellesmere Island, Nunavut, Canada (79°40'N, 74°30'W; Figure 3.1). It covers an area of approximately 165 km², and ranges in elevation from 100 m to 1200 m asl. Over the period 1996-2000, mean annual air temperature was -14.7°C over the glacier terminus, with a range of monthly means between -29.2°C in February 1999 and +4.8°C in July 1999. High bed reflection powers and the presence of an internal reflector in radio-echo sounding records indicate a warm base beneath most of the ablation zone (Copland and Sharp, in press).

Radio-echo sounding measurements were made at ~3200 locations over the glacier surface with a custom-built unit operating at centre frequencies of 5, 10 or 20 MHz (higher frequencies were used in shallower ice depths). The monopulse transmitter produced a peak power of 24 kW (Narod and Clarke, 1994), and a Tektronix 730 digital oscilloscope connected to a HP palmtop computer acted as the receiver and data recorder. The unit was towed on two sleds, and the signal was low pass filtered at 1.5x the transmitted centre frequency and averaged over 32 traces to reduce noise. It was then high pass filtered with the RADAN software package (Geophysical Survey Systems, Inc.) to remove the low frequency feature that is present at the start of traces where the transmitter and receiver are oriented in-line. The data were not migrated due to irregular trace and transect spacing caused by complex surface topography, crevasses, and deeply incised surface streams.

3.3 RESULTS

3.3.1 Water input locations

For most polythermal glaciers, crevasses (linear cracks in the ice surface) and moulins (near-vertical shafts) provide the main routes for water to enter the glacier interior. The location and characteristics of these features are important inputs for hydrological modelling because they control the subglacial water distribution, which in turn is a control on ice dynamics. They can be observed where the snow melts in the summer, but are difficult to map in other parts of the glacier and at other times of the year.

Crevasses and moulins are identifiable in radio-echo sounding records as a series of near-surface reflectors due to the large dielectric contrast between glacier ice and the air or water within them. There are few other internal reflectors in polythermal glaciers, so plots of spatial variability in internal reflection power (IRP) provided an effective means of identifying these features. Returned power was determined by squaring and summing the amplitudes of the raw traces, with the IRP calculations covering the period between the end of the ground wave (600 ns after air wave peak) and the start of the bed reflection (100 ns before bed peak). To normalize the results, the total power was divided by the measurement period to produce units of $\text{mV}^2 \text{ns}^{-1}$.

Figure 3.2 shows the variability in IRP over John Evans Glacier, and there is indeed a strong correlation between areas of high IRP and the location of crevasses and moulins seen in the field and in aerial photos and satellite imagery (Fig. 5.2).

3.3.2 Subglacial flow routing

Raw radio-echo sounding data provide basic information about the shape and relative location of reflectors, but little about their actual depth below the surface unless the radio wave velocity (RWV) is known. The RWV in a glacier depends on many factors such as ice density, water content and ice structure, with measured values typically in the range 0.150 to 0.190 m ns⁻¹ (Bogorodsky et al., 1983). Many workers use a mean velocity of 0.167 m ns⁻¹ to convert travel times to depths (e.g., Knudsen & Hasholt, 1999), but this value is not appropriate for all glaciers.

To determine the appropriate RWV for John Evans Glacier, a series of common mid-point (CMP) soundings were made at 12 locations over the glacier surface in summer 1999. CMP surveys involve separating the transmitter and receiver equally from a central point while measuring the variation in travel time of the waves to a central bed reflector. An example of the results from such a survey are provided in Figure 3.3, with the three primary radar returns relating to:

1. The air wave (A) - which triggers the oscilloscope, and travels directly through the air between the transmitter and receiver at the speed of light (~ 0.300 m ns⁻¹)
2. The ground wave (G) - which travels along the near surface at the RWV of ice.
3. The bed wave (B) - which is reflected from the glacier bed and travels at the RWV of ice.

The RWV of ice is determined by solving (Macheret et al., 1993):

$$\tau_B = \frac{1}{V_B} \sqrt{4h_B^2 + d^2 \cos^2 \varphi_B} \quad (1)$$

where $\tau_B = \tau_d + \tau_0$ (τ_d is the delay time of the bottom signal B measured relative to A, τ_0 is the propagation time in air of signal A from the transmitter to the receiver), V_B is the

mean velocity of the bottom signal B , h_B is the echo depth of the bottom, d is the antenna separation distance, and φ_B is the difference in slope angles of the glacier surface and glacier bed. Given that φ_B is approximately 0 at the CMP locations, Equation (1) can be transformed to a linear form:

$$y = ax + b \quad (2)$$

by squaring and assigning:

$$y = \tau_B^2, \quad x = d^2, \quad a = \frac{1}{V_B^2}, \quad b = \frac{4h_B^2}{V_B^2} \quad (3)$$

the RWV through the ice is calculated by plotting d^2 vs. τ_B^2 , and fitting a linear least-squares regression line through the data points (Figure 3.4). The mean velocity is then given by the square root of the inverse slope of the regression line. For the 12 CMP sites on John Evans Glacier, the mean RWV was 0.1711 m ns^{-1} , with a standard deviation of 0.0031 m ns^{-1} . This velocity is equivalent to a real dielectric constant of 3.074. Using this velocity (V_{ice}), the ice depth (h) was determined for the 3200 trace locations at John Evans Glacier by:

$$h = \left(\frac{t_s + t_b}{2} \right) V_{ice} \quad (4)$$

where t_s is the time taken for the trigger wave to pass across the glacier surface between the transmitter and receiver, and t_b is the time between the peak of the air and bed waves. The times are halved to convert the two-way travel time to an ice depth.

A digital elevation model (DEM) of the glacier bed was produced by subtracting the ice depth from the surface elevation and then interpolating between the known bed elevations with a TIN (triangular irregular network). The horizontal location of each trace was measured with a hand-held GPS, and the surface elevation was determined by referencing the horizontal location to a DEM of the glacier surface derived from aerial

photogrammetry (Woodward et al., 1997). Both the surface and bed DEMs were interpolated to matching 25 m grids.

Using a modification of the method outlined by Shreve (1972), the gridded hydraulic potential was calculated from the DEMs of the glacier surface and bed by (Paterson, 1994):

$$\Phi = \rho_w g B + f \rho_i g (H - B) \quad (5)$$

where ρ_w and ρ_i are the densities of water and ice, g is the acceleration due to gravity, B is the bed elevation, f is the ratio of subglacial water pressure to ice overburden pressure (i.e., p_w/p_i), and H is the surface elevation. Using the 'hydro' extension in ArcView, the drainage reconstruction was produced from the gridded hydraulic potentials in three steps:

1. Any sinks (i.e., overdeepenings) were filled to allow water to pass across them
2. The flow direction was defined by the adjacent 25 x 25 m cell with the lowest elevation
3. The flow accumulation was calculated as the number of upstream cells that flow into each downslope cell

Figure 3.5 shows the reconstructed subglacial drainage for the ablation area of John Evans Glacier for $f = 1$, and for cells with upstream flow accumulation of 50 cells or more. The reconstruction is not shown for the accumulation area due to the low bed reflection powers there that are indicative of cold-based ice and a dry bed (Copland and Sharp, in press). Reconstructions with different values of f made no significant difference to the flow routing, and increasing/decreasing the specified minimum flow accumulation simply shortened/lengthened the individual flow paths. A reconstruction of water flow over the bedrock under atmospheric conditions was also made (i.e., $f = 0$), but this made no significant difference to the routing.

From these reconstructions, it is evident that bedrock topography dominates flow routing beneath John Evans Glacier. A large bedrock ridge (A in Figure 3.5) controls flow in the ablation area, with most water flowing in the catchment to the north of the

ridge (B) before reaching the glacier terminus. There is a secondary catchment (C) to the south of the bedrock bump with a smaller upstream accumulation area. There are also overdeepened areas to the north and south of the bedrock ridge where the flow reconstructions suggest that water collects (B and C in Figure 3.5). Further evidence for subglacial water ponding in these areas is provided by the presence of high bed reflection powers (Copland and Sharp, in press).

The black dots in Figure 3.5 mark the location of two large moulins in the area of high IRPs (Figure 3.2), which provide sinks for supraglacial streams. If water reached the glacier bed directly beneath these features it would flow in the northern catchment, although it could pass into the southern catchment as observations suggest that water may flow for considerable distances englacially between the base of moulins and the glacier bed (Holmlund, 1988). Further work (e.g., dye tracing) is necessary to determine which routing is correct.

3.3.3 Subglacial properties

Repeat traces at the same location in the centre of the glacier terminus were recorded over a nine day period in July 1999 (Figure 3.6a; the survey location is marked by a triangle in Figure 3.5). The system parameters remained the same for all surveys, with a transmitted centre frequency of 10 MHz, a parallel antenna configuration with the dipoles aligned up- and down-glacier, and a receiver/transmitter separation of 10 m. Traces were recorded manually whenever we walked by the equipment. Except on days 194 and 198, when they were used for CMP surveys, the transmitter and receiver remained in the same position throughout the experiment. When it was necessary to move them, markers were placed on the ice surface so that the equipment was replaced in the same location after it was moved. Ice depth at the measurement location was 124 m.

The timing of the bed reflection was the same for all traces, but the returned bed power (evaluated from 100 ns before the first bed peak to 400 ns after it) varied by up to 50% (Figures 3.6a and 3.6b). This variation in bed power was mainly a result of changes in the magnitude and number of returns which occurred after the first bed peak (Figure 3.6a). Since the system setup and ice depth remained constant, it is assumed that variability in bed reflection power is related to differences in transmitted energy and/or

the nature of the basal reflector. Gades (1998) argued that variable coupling between the antennae and glacier surface can produce significant differences in the amount of power transmitted into the glacier, and is primarily influenced by the amount of water at the glacier surface. More water results in better coupling and stronger basal reflection strengths, even when conditions at the glacier bed are constant. Figure 3.7a shows that ground wave power (evaluated from 150 ns to 600 ns after the air wave peak) did vary during the repeat survey period. If surface coupling is an influence on basal reflection strength, there should be a positive relationship between bed power and ground wave power. Figure 3.7b shows that such a relationship does not exist, which suggests that variability in basal reflection strength is related to physical changes at the glacier bed. The recorded bed power decreased following movement of the equipment on day 194, but not following movement of the equipment on day 198. From these observations it is hard to determine whether equipment movement was a significant influence on the recorded bed reflection power.

Gauging records from a supraglacial stream which feeds water to the glacier bed via one of the moulins marked on Figure 3.5, from a proglacial stream that provides the main outflow at the glacier terminus, and air temperature records from a weather station ~250 m upglacier of the survey point, display several similarities to the bed power patterns (Figure 3.6). Although only two measurements were made on each of the first two days, bed power is higher in the late afternoon than in the morning. This correlates with similar changes in supraglacial stream discharge during a period of relatively warm weather, with higher flows in the late afternoon than the morning. In addition, the higher diurnal bed powers on day 191 than day 190 coincide with an increase in proglacial discharge over this time. This proglacial discharge event represents the flood generated by drainage of a supraglacial lake into one of the moulins identified in Figure 3.5 on day 188. Proglacial discharge then falls on day 193 as the glacier bed dries out, with a decrease in supraglacial discharge and virtual disappearance of diurnal patterns after day 195 as the weather cools and there is a small snowfall. Bed power also declines over this period, with values during the coldest and lowest discharge period on day 196 and 197 almost half of those at the peak on day 191. The supraglacial, and later the proglacial, discharge increases on day 198 and the early part of day 199 as the weather warms, but

then falls again on day 199 as temperatures cool. By the time a radar measurement was made late in the evening on day 199 the water had largely drained from beneath the glacier terminus, and consequently the bed power remained low.

From these records, it appears that variability in the quantity of water at the glacier bed provides a control on returned bed power. This can be explained by the dielectric constant of water of ~ 88 at 0°C , which is much higher than the dielectric constants of $\sim 6-15$ common to most other subglacial materials.

Figure 3.5 shows that the repeat survey point is located at the upper end of a predicted subglacial flow path, which suggests that variability in bed power might arise from changes in water flow through a subglacial channel. If this were the case, a phase inversion would be expected in radio-echo sounding returns as the channel filled and drained because the dielectric constant of air is lower than that of ice, while the dielectric constant of water is higher than that of ice (Arcone, 1996). The phase remains constant for all traces, however, which makes it likely that the radar returns are responding to changes in water flow through or over basal sediment. A 4 m thick aquifer beneath the glacier snout provides strong support for a sediment layer beneath the terminus region (Skidmore and Sharp, 1999), and Gades (1998) demonstrates that bed power changes of 25-50% can be produced on the time scale of days by changes in porosity and/or water conductivity in the upper portion of a stratified till layer.

3.4 CONCLUSIONS

This study has demonstrated that radio-echo sounding provides an effective method for monitoring and detecting several hydrological features of polythermal glaciers:

1. Internal and near-surface features such as moulins and crevasses can be identified by high internal reflection powers. This provides a method for remotely mapping near-surface features which are often snow covered and difficult to access in the field.
2. Using common mid-point surveys, the mean radio-wave velocity through John Evans Glacier was measured as $0.1711 \pm 0.0031 \text{ m ns}^{-1}$. This enables determination of true ice thickness and bed topography, and allows predictions of subglacial flow routing.

These flow predictions are supported by maps of returned bed power (Copland and Sharp, in press).

3. Repeat traces over a nine day period in July 1999 appear to show a relationship between basal reflection strength, air temperature, and supraglacial/proglacial stream discharge. Higher resolution measurements are necessary to evaluate whether this may provide a way to monitor changes in hydrological conditions at the glacier bed.

3.5 BIBLIOGRAPHY

Arcone, S.A. 1996. High resolution glacial ice stratigraphy: a ground-penetrating radar study of Pegasus Runway, McMurdo Station, Antarctica. *Geophysics*, **61**, 1653-1663.

Arnold, N. and Sharp, M. 1992. Influence of glacier hydrology on the dynamics of a large Quaternary ice sheet. *Journal of Quaternary Science*, **7**, 109-124.

Blatter, H. and Hutter, K. 1991. Polythermal conditions in Arctic glaciers. *Journal of Glaciology*, **37**, 261-269.

Bogorodsky, V., Bentley, C. and Gudmandsen, P. 1983. *Radioglaciology*. Reidel, Dordrecht, 254 pp.

Copland, L. and Sharp, M. *In press*. Mapping thermal and hydrological conditions beneath a polythermal glacier with radio-echo sounding. *Journal of Glaciology*.

Gades, A.M. 1998. Spatial and temporal variations of basal conditions beneath glaciers and ice sheets inferred from radio echo-sounding measurements. Unpublished Ph.D. thesis, University of Washington.

Heine, J.T. and McTigue, D.F. 1996. A case for cold-based continental ice sheets – a transient thermal model. *Journal of Glaciology*, **42**, 37-42.

Holmlund, P. 1988. Internal geometry and evolution of moulins, Storlgaciären. Sweden. *Journal of Glaciology*, **34**, 242-248.

Iken, A. and Bindschadler, R.A. 1986. Combined measurements of subglacial water pressure and surface ice velocity of Findelengletscher, Switzerland: conclusions about drainage system and sliding mechanism. *Journal of Glaciology*, **32**, 101-117.

Knudsen, N.T. and Hasholt, B. 1999. Radio-echo sounding at the Mittivakkat Gletscher, Southeast Greenland. *Arctic, Antarctic and Alpine Research*, **31**, 321-328.

Macheret, Y.Y., Moskalevsky, M.Y. and Vasilenko, E.V. 1993. Velocity of radio waves in glaciers as an indicator of their hydrothermal state, structure and regime. *Journal of Glaciology*, **39**, 373-384.

Narod, B.B. and Clarke, G.K.C. 1994. Miniature high-power impulse transmitter for radio-echo sounding. *Journal of Glaciology*, **40**, 190-194.

Paterson, W.S.B. 1994. *The Physics of Glaciers* (3rd ed.). Elsevier Science, Oxford.

Shreve, R.L. 1972. Movement of water in glaciers. *Journal of Glaciology*, **11**, 205-214.

Skidmore, M.L. and Sharp, M.J. 1999. Drainage system behaviour of a High Arctic polythermal glacier. *Annals of Glaciology*, **28**, 209-215.

Willis, I.C. 1995. Intra-annual variations in glacier motion: a review. *Progress in Physical Geography*, **19**, 61-106.

Woodward, J., Sharp, M. and Arendt, A. 1997. The effect of superimposed ice formation on the sensitivity of glacier mass balance to climate change. *Annals of Glaciology*, **24**, 186-190.

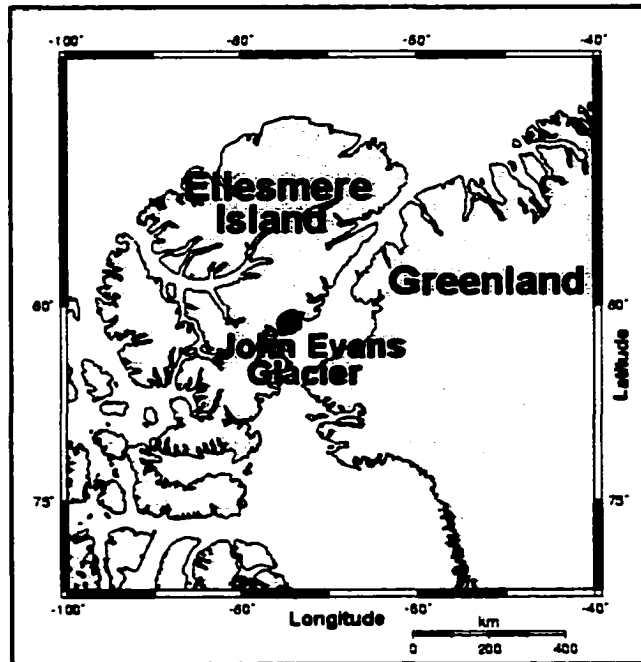


Figure 3.1 Location of John Evans Glacier

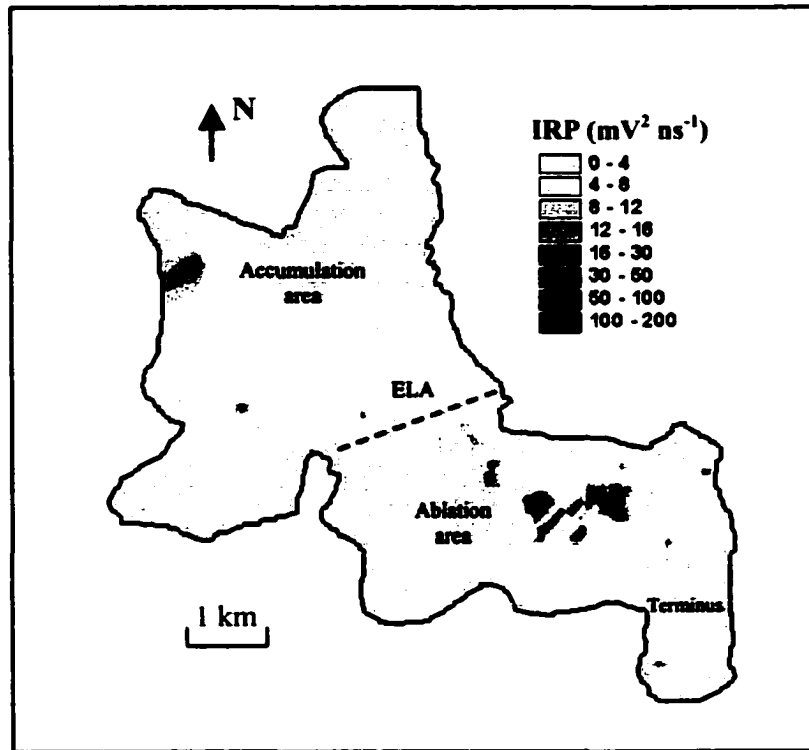


Figure 3.2 Variability in internal reflection power (IRP) over John Evans Glacier. High values correlate with the location of crevasses and moulins. ELA = equilibrium line altitude

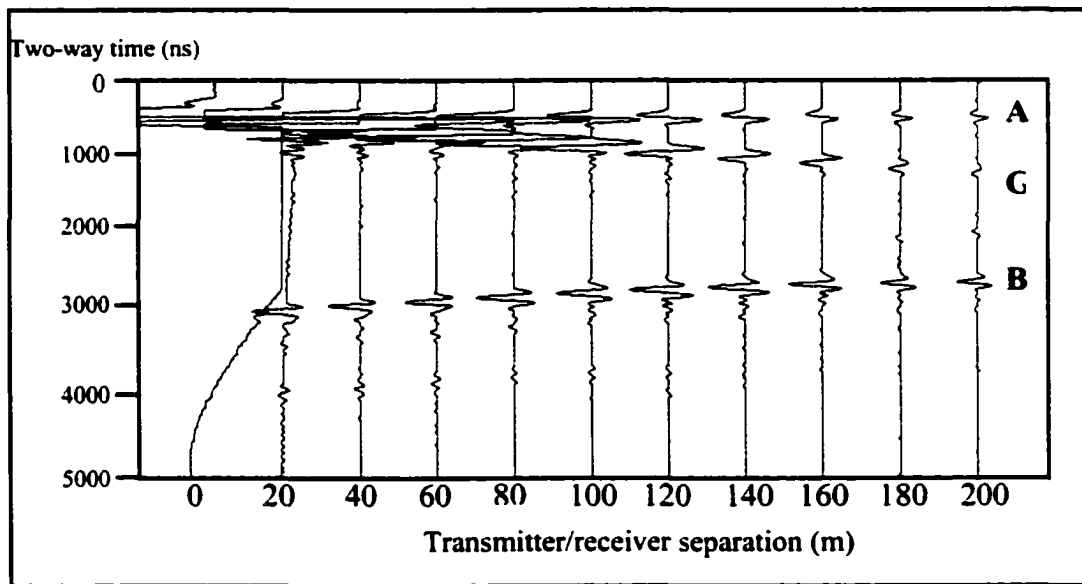


Figure 3.3 An example set of traces from a common mid-point survey at John Evans Glacier. A = air wave; G = ground wave; B = bed wave. Depth to bed is ~124 m. The time for the air wave to travel between the transmitter and receiver is not taken into account.

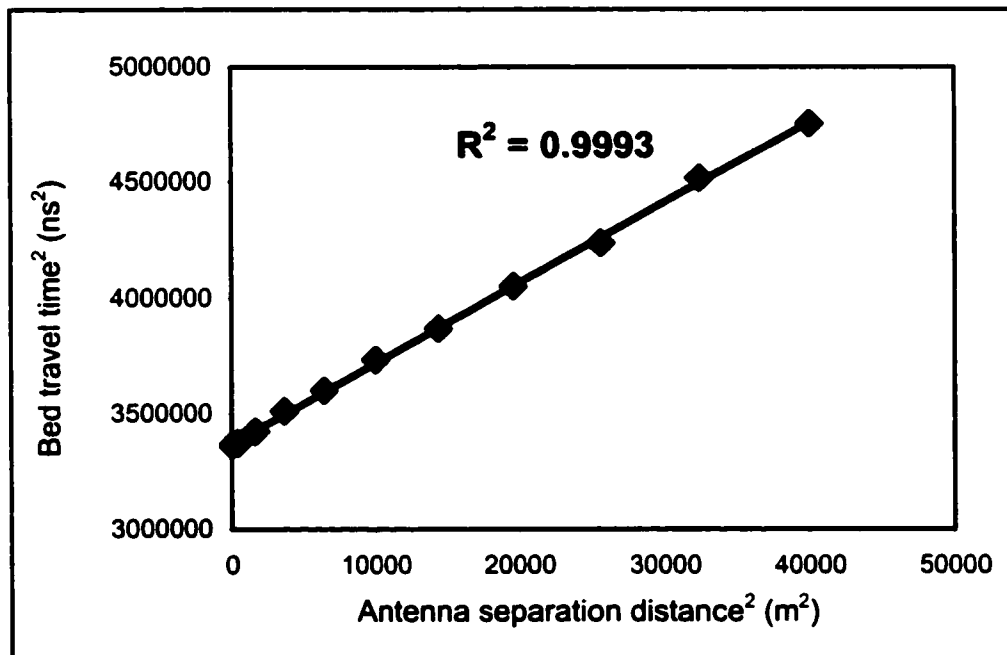


Figure 3.4 An example of the linear regression used to calculate the mean radio wave velocity through ice at John Evans Glacier. R^2 values were >99.99% significant for all 12 common mid-point surveys

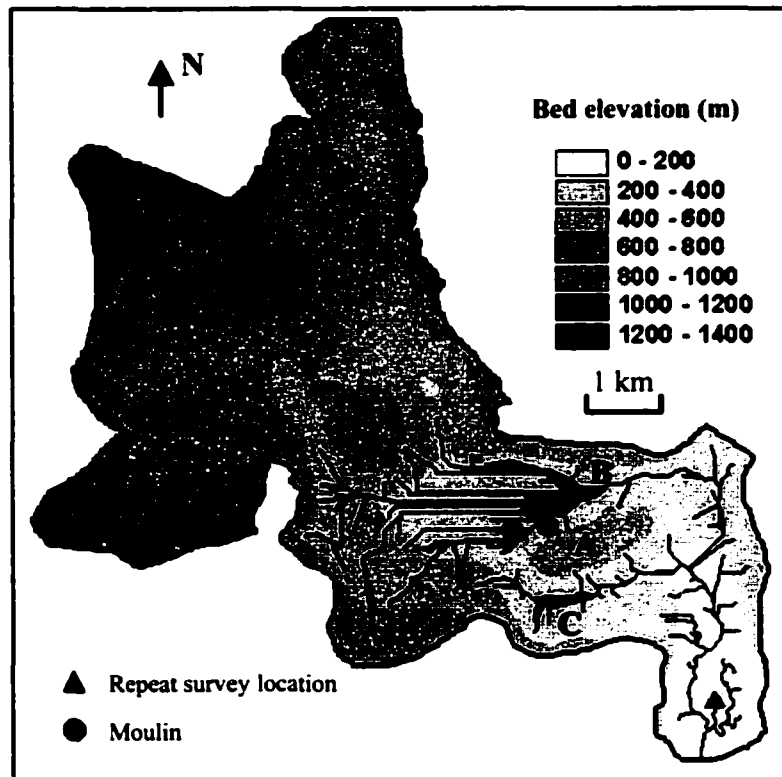


Figure 3.5 Subglacial flow reconstruction for the ablation area of *John Evans Glacier*. A is a bedrock ridge; B and C indicate overdeepened areas and separate catchments

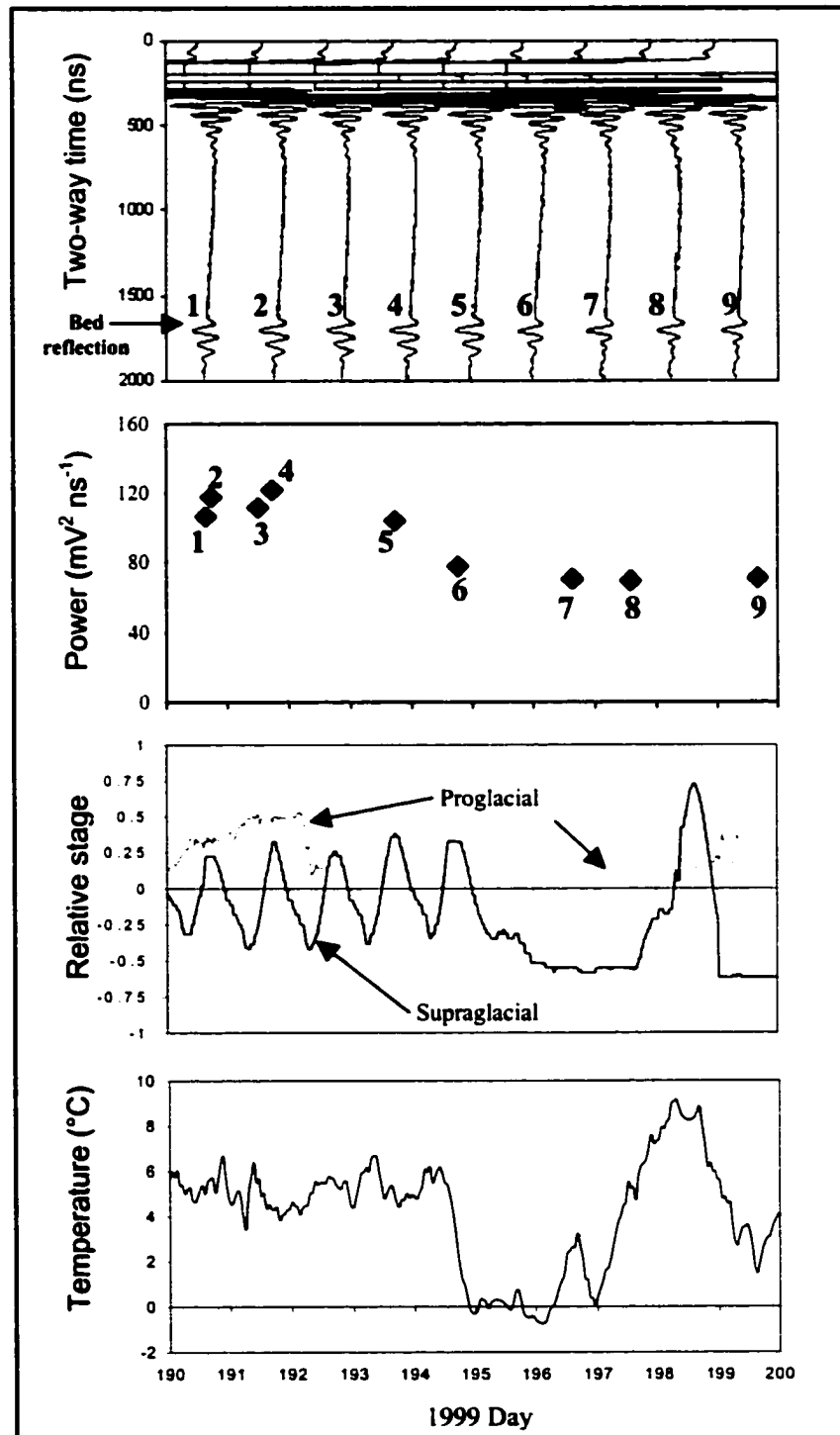


Figure 3.6 (a) Raw traces recorded over the repeat survey period (b) Bed reflection power of these traces corrected for date (day 190 = July 9) (c) Supraglacial and proglacial stream stage records. Part of the proglacial stream record is missing due to changes in the location of the main channel (d) Air temperature recorded at a weather station on the glacier terminus

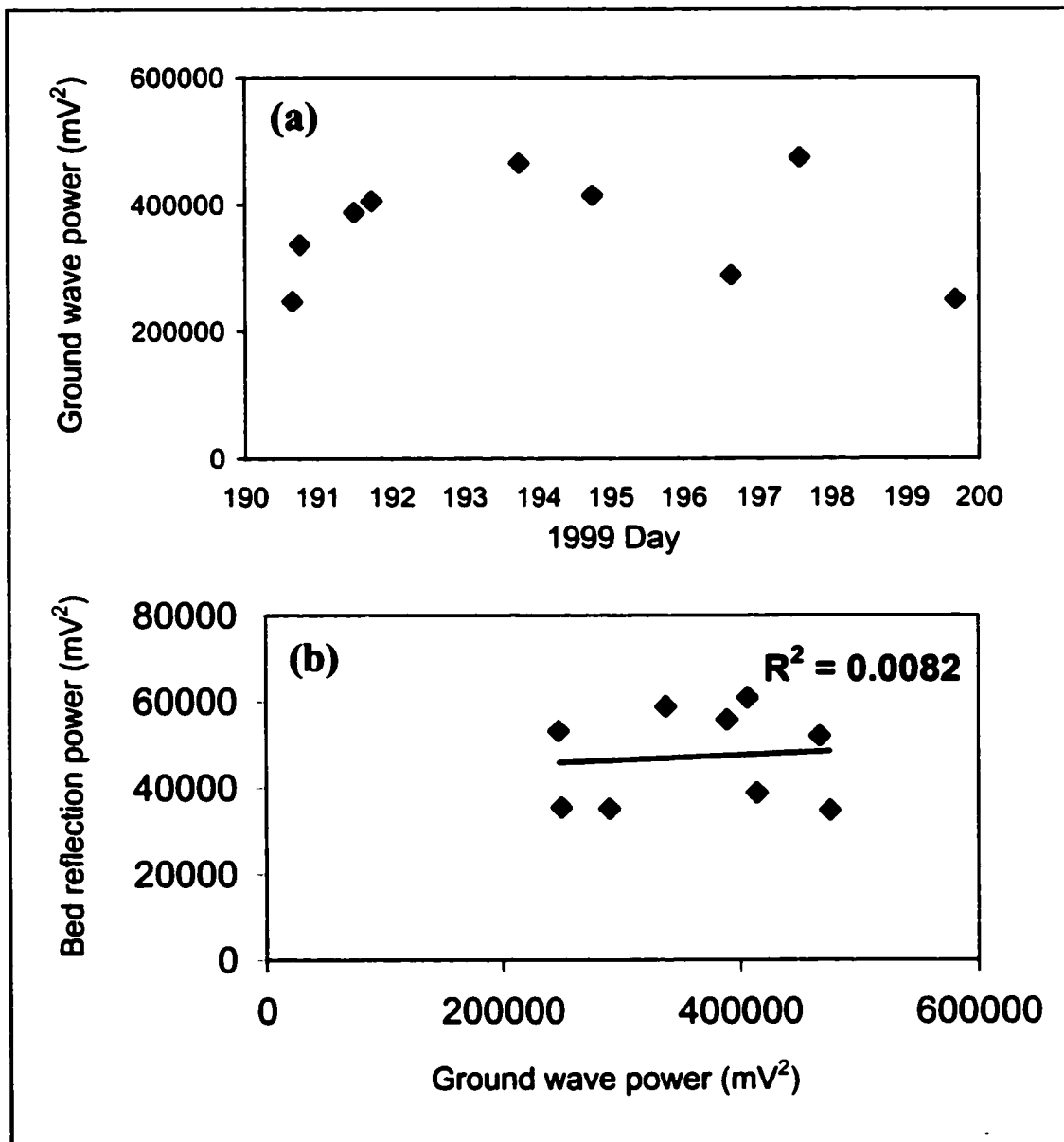


Figure 3.7 (a) Variability in ground wave power from the traces displayed in Figure 3.6a over the repeat survey period (b) Relationship between ground wave power and bed reflection power over the same period

CHAPTER 4

THE DISTRIBUTION OF BASAL MOTION BENEATH A HIGH ARCTIC POLYTHERMAL GLACIER

4.1 INTRODUCTION

Measurements on temperate glaciers have shown that water at the glacier bed is an important control on basal motion, with short-term high velocity events correlating with large transient basal water pressures (Iken and Bindshadler, 1986; Paterson, 1994; Willis, 1995). Polythermal glaciers contain both temperate and cold ice, and subglacial drainage exists only where the basal ice is warm (i.e., at the pressure melting point). Our objectives in this paper are to determine whether basal motion occurs beneath a polythermal glacier in the Canadian high Arctic, to assess its relationship to basal thermal and hydrological conditions, and to determine the extent to which longitudinal stress coupling may expand surface velocity anomalies away from areas of basal motion.

In our discussion, basal motion refers to any motion at the base of a glacier which is not caused by ice deformation. This encompasses both basal sliding and/or basal sediment deformation. Longitudinal coupling describes the horizontal distance over which a local gradient in ice motion affects ice motion in an upglacier and downglacier direction. This is highly dependent on viscosity, which means that highly viscous cold ice typically has a longer coupling length than warm ice (Kamb and Echelmeyer, 1986).

Our analysis is based on measurements of summer and winter surface velocities at 20 locations along the centre-line of John Evans Glacier, Ellesmere Island. These measurements are compared with surface velocities due to ice deformation that are predicted from ice thicknesses and surface slopes along the glacier centre-line. Basal motion is assumed to occur where observed surface velocities consistently exceed predicted deformation velocities. To test the reliability of estimates of basal motion, ice deformation rates were calculated for the range of likely ice temperatures and for different longitudinal coupling lengths.

There have been several previous studies of the surface motion of polythermal glaciers (Iken, 1974; Andreasen, 1985; Hooke et al., 1989; Rabus and Echelmeyer, 1997). These generally suggest that basal motion occurs over at least part of the ablation zone in the summer. Iken (1974) found a strong relationship between short-term summer velocity increases and water pressures in nearby moulins at White Glacier, Axel Heiberg Island. Andreasen (1985) observed seasonal velocity fluctuations at Kitdlerssuaq Glacier, West Greenland, and Hooke et al. (1989) made similar observations at Storglaciären, Sweden. At McCall Glacier, Alaska, Rabus and Echelmeyer (1997) found summer velocity increases of up to 75% above mean winter values. From an analysis similar to that described here, they concluded that basal motion occurred year-round beneath a 2 km section of the lower glacier, where it accounted for more than 70% of the total motion.

The rationale for performing this study at John Evans Glacier is that the glacier is in a cold, dry climate where no previous analysis has been made of the seasonal occurrence and distribution of basal sliding. From records at 3 automatic weather stations along the length of the glacier between 1997 and 1999 (Fig. 4.1), the mean annual air temperature was -14.8°C . Ice temperatures at 15 m depth in the accumulation area range between -9.5°C and -15.1°C (Fig. 4.1). This compares to a mean annual air temperature of -12°C , and ice temperatures of -1°C to -1.5°C in the accumulation area of McCall Glacier (Rabus and Echelmeyer, 1997). The higher ice temperatures at McCall Glacier are the result of greater latent heat release from the refreezing of meltwater in the snowpack. The potential implications of lower ice temperatures for ice motion include differences in longitudinal coupling length, and in the ability of surface meltwater to reach the glacier bed and escape through a frozen margin.

4.2 JOHN EVANS GLACIER

John Evans Glacier is a polythermal valley glacier on the central east coast of Ellesmere Island, Canada ($79^{\circ}40'\text{N}$, $74^{\circ}30'\text{W}$; Fig. 4.1). The glacier is approximately 20 km long, ranges in elevation from 100 m to 1200 m asl, and the ice covers approximately 165 km^2 . Radio-echo sounding indicates a mean ice thickness of ~ 150 m in the terminus area, and a maximum ice thickness of almost 400 m close to the equilibrium line at ~ 750 - 850 m asl (Copland and Sharp, 2000). High residual bed reflection powers from radio-

echo sounding suggest that the ablation area is mainly warm-based, while low residual powers suggest that the accumulation area is mainly cold-based (Copland and Sharp, in press). The main exceptions to this pattern occur along the glacier margin and over a pronounced bedrock bump in the ablation area, where the ice is frozen to the bed.

During the melt season (typically early June to early August), most surface runoff from the lower ablation area flows off the glacier margins, while most surface runoff from the accumulation and upper ablation areas sinks to the glacier bed via a series of moulins in a crevasse field between stakes 9 and 10 (Fig. 4.1). This water likely flows along the glacier bed as dye tracing shows that the sediment-free and low electrical conductivity (EC) water ($<10 \mu\text{S cm}^{-1}$) that enters the moulins is released at the glacier terminus as sediment-laden and high EC water ($> 100 \mu\text{S cm}^{-1}$) within a period of hours to days in the summer (Bingham et al., 2001). In the early melt season, this subglacial meltwater is trapped beneath the glacier terminus by a thermal dam created by the frozen snout (Skidmore and Sharp, 1999). This dam is typically breached at the end of June/start of July, which releases a large flood pulse over the proglacial area which contains water with $\text{EC} >400 \mu\text{S cm}^{-1}$.

4.3 MEASUREMENTS

4.3.1 Ice motion

Twenty velocity stakes were drilled and frozen into the ice surface along the glacier centre-line (Fig. 4.1). These were surveyed regularly to determine rates of surface motion over both summer and winter periods. Reflecting prisms were mounted on the lower 9 stakes, which were surveyed with an electronic theodolite from a station located on bedrock. The upper 11 stakes were out of range of the theodolite, so were surveyed by differential GPS. To ensure consistency between measurements, summer velocities relate to the last 2 to 3 weeks of July, while overwinter velocities represent the period between the last survey of one field season and the first of the next field season (typically early August to late May). Most overwinter velocities were measured in 1999/2000, and most summer velocities in 1999. Exceptions (due to poor or missing data) are that summer 2000 velocities were used for stakes 1-3, while the overwinter 1998/99 velocity was used for stake 15. Where surface velocities were recorded at the same stake in different years,

there was good agreement to within +/- 10% in horizontal motion for both summer and winter measurement periods. To enable comparison between the different lengths of the summer and winter measurement periods, all velocities are corrected to m a^{-1} .

Errors in the theodolite measurements were determined by locating each stake at least twice per daily survey in July 1999 (the original data set was subsampled to produce the velocities reported here). The difference between the two or more measurements of a stake and its mean location for a given survey provide a mean position error of +/- 0.61 cm. By assuming that successive position errors are of opposite sign, this equates to a mean horizontal displacement error of +/- 1.22 cm. This produces a mean velocity error of +/- 0.22 m a^{-1} over a typical 20 day summer measurement period, and +/- 0.015 m a^{-1} over a typical 300 day overwinter measurement period.

An estimate of the errors in the differential GPS measurements is provided by the unit directly, and averages +/- 1.04 cm for the positioning of a stake. This equates to a maximum displacement error of +/- 2.08 cm if we assume that successive position errors are of opposite sign. Over a 20 day summer measurement period this produces a mean velocity error of +/- 0.38 m a^{-1} , while over a 300 day overwinter measurement period the mean velocity error is +/- 0.025 m a^{-1} . These errors are much lower than the measured velocities, and give confidence that measurements over these timescales represent an accurate picture of the ice motion field. It is also likely that some errors arise from factors such as the tilting of stakes by wind or melt between surveys, but these influences are likely small in comparison to the true ice motion.

4.3.2 Glacier geometry

A digital elevation model (DEM) of the glacier surface was derived from 1959 stereo aerial photography (Woodward et al., 1997), and verified against the differential GPS measurements made in 1999. On average, the surface elevation at the centre-line stakes was 7.3 m lower in 1999 than 1959, although the elevation change did not vary in a consistent way with distance along the centre line, and some stakes were at higher elevations in 1999 than 1959. Comparison between the original aerial photography and 1999 Landsat 7 imagery indicates little difference in the length or area of John Evans Glacier since 1959. These observations show that John Evans Glacier has changed little

over the last 40 years, and give us confidence that the surface DEM provides a representative picture of the surface conditions. The surface DEM was interpolated to a regular grid with 25 m spacing, and was used in the calculation of the surface slopes used as input for the ice deformation calculations discussed later. The mean surface slope at a point was determined from the change in elevation between grid points 100 m to the N, E, S and W of that point (Zevenbergen and Thorne, 1987).

Ice thicknesses were determined from ground based radio-echo sounding at 3200 locations between 1997 and 1999 (Copland and Sharp, 2000; Copland and Sharp, in press). A DEM of the glacier bed was produced by subtracting the ice thickness from the surface DEM elevation at each measurement location, and interpolating the resulting bed elevations to a 25 m grid that matches the surface DEM (Fig. 4.2). The ice thickness at each point along the centre-line was determined by subtracting the bed DEM from the surface DEM. Errors in the bed DEM arise from errors in both the surface DEM and the ice thickness calculations, and are estimated at 10 to 20% of the local ice thickness (Copland and Sharp, in press). Errors of this magnitude make little difference to the ice deformation calculations discussed later.

4.4 RESULTS AND ANALYSIS

4.4.1 Measured ice motion

Along the glacier centre-line, velocities are relatively low ($< 18 \text{ m a}^{-1}$) in the accumulation area and upper ablation area (stakes 1-9), with relatively little change between the summer and winter (Fig. 4.3). There is a rapid increase in velocity between stakes 9 and 10, particularly in the summer when the velocity increases from 17.5 m a^{-1} at stake 9 to 32.1 m a^{-1} at stake 10 over a horizontal distance of 800 m. As expected, this area contains numerous transverse crevasses (Fig. 4.1). Between stakes 10 and 17, surface velocities reach their peak in both winter and summer. Summer velocities are on average 62% higher in the summer than the winter in this region, with local increases of up to double overwinter levels (e.g., stake 11 increased by 102%). Towards the glacier terminus, there is a general reduction in velocity below stake 18, although velocities are still higher in the summer than the winter.

Initial analysis of the surface velocity field suggests that basal motion occurs at least during the summer between stakes 10 and 17. The large increase in summer motion at these stakes is too high to be explained by seasonal changes in ice deformation. As discussed earlier, moulins in the crevasse field between stakes 9 and 10 provide the main location where supraglacial meltwater enters the glacier bed. The rapid onset of high velocities in this crevassed region suggests that surface-fed subglacial water flow is an important influence on basal motion beneath the lower ablation area in the summer.

The important question that remains is whether basal motion also occurs during the winter at John Evans Glacier, when very cold air temperatures prevent surface melting. Recent work by Rabus and Echelmeyer (1997) suggests that basal motion may occur throughout the year at polythermal McCall Glacier, Alaska. To determine whether basal motion occurs during the winter at John Evans Glacier, we start by predicting the motion due to ice deformation for the likely range of ice temperatures at the glacier, and for a range of longitudinal coupling lengths. Excess of measured motion over predicted motion will be taken to suggest that basal motion occurs, and we will attempt to determine the distribution and rate of basal motion that must be imposed to match predicted and observed surface velocities.

4.4.2 Predicted ice motion

4.4.2.1 Predicted ice motion without longitudinal stresses

If longitudinal stresses are ignored, the surface motion due to ice deformation (u_d) at any point along the centre-line of a glacier flowing in a channel of parabolic cross-section can be described by (Nye, 1965; Rabus and Echelmeyer, 1997):

$$u_d = \frac{2A}{n+1} (\rho g f \sin \alpha)^n h^{n+1} \quad (1)$$

where A is the flow-law parameter, n is the flow-law exponent (we use a value of 3), ρ is the density of ice, g is the acceleration due to gravity, f is the shape factor, α is the surface slope angle, and h is ice thickness. To evaluate equation (1), a centre-line transect with 100 m grid point spacing was defined that passes through the DEM grid cells in

which the stakes are located. The bed and surface topography, together with the values of f , h and α at each velocity stake, are shown in Fig. 4.4. In all of our figures, we only show the results at the grid cells which contain velocity stakes as these are the only locations where we have velocity measurements to compare to predictions. Ice thickness reaches a peak of ~ 300 m around the equilibrium line between stakes 6 and 9, and decreases gradually towards the glacier snout. The value of f is based on the half-width to depth ratio of the channel along the glacier centre-line (Paterson, 1994), and is generally close to 1 due to the relatively large channel width. The surface slope angle is generally low ($<6^\circ$) and invariant throughout the accumulation area, but is higher and more variable in the ablation area, with a peak of 7.9° at stake 17.

The value of A depends mainly on ice temperature, and can cause large spatial variations in ice motion when the ice is non-temperate. This is because A has a linear influence on ice deformation in equation (1), and increases in value by 50% between -5°C and -2°C (Paterson, 1994). Since we do not have any deep borehole temperature measurements, we use values of A for two scenarios to represent the likely upper and lower limits of ice temperatures. The value of A is weighted towards ice temperatures close to the glacier bed, as this is where most ice deformation occurs. Based on the measured ice temperatures at 15 m depth (Fig. 4.1), and inferences about thermal conditions at the glacier bed from radio-echo sounding (Copland and Sharp, in press), these two scenarios are:

- (a) *Warm*: depth weighted mean ice temperatures of -5°C in the accumulation and upper ablation areas (stakes 1-9), and -2°C in the lower ablation area (stakes 10-20).
- (b) *Cold*: depth weighted mean ice temperatures of -10°C in the accumulation and upper ablation areas (stakes 1-9), and -5°C in the lower ablation area (stakes 10-20).

Although these scenarios are crude estimates of the true ice temperature distribution, they bracket the range of likely conditions at John Evans Glacier, and provide upper and lower limits to our ice deformation calculations. The values of A that relate to these temperature distributions are taken from Paterson (1994), and are $2.4 \times 10^{-24} \text{ Pa}^{-3} \text{ s}^{-1}$ at -2°C , $1.6 \times 10^{-24} \text{ Pa}^{-3} \text{ s}^{-1}$ at -5°C , and $4.9 \times 10^{-25} \text{ Pa}^{-3} \text{ s}^{-1}$ at -10°C .

The surface velocities predicted by equation (1) for the two temperature scenarios are shown in Fig. 4.5, together with the measured winter velocities. The fit between the predicted and measured velocities is generally poor, with under-prediction at virtually all stakes using the cold scenario, particularly in the accumulation area. The fit with the warm scenario is better in the accumulation area, but fluctuates between large over- and under-prediction in the ablation area. This high frequency variability in predicted velocities is attributable to large local variations in surface slope and ice thickness, which are not smoothed out due to the failure of equation (1) to take longitudinal coupling into account. Clearly, longitudinal stresses need to be taken into account if we are to improve the predictions of surface motion.

4.4.2.2 Predicted ice motion with longitudinal stresses

Following Kamb and Echelmeyer (1986), and Rabus and Echelmeyer (1997), the effect of longitudinal stresses on the deformational velocity of a glacier can be determined by averaging the effect of α , f and h with a triangular weighting function of unit value to give a value B :

$$B(x) = \int_{x-2l}^{x+2l} (n \ln(\alpha f) + (n+1) \ln h) (1 - |x' - x| / 2l) dx' \quad (2)$$

where l is the longitudinal coupling length, x is the centre-line position where $B(x)$ is evaluated, and x' is the centre-line position where the integral is being evaluated. For John Evans Glacier, the integral is approximated as a finite sum at a spacing $\Delta x'$ of 100 m over a total distance of $\pm 2l$ from x . The triangular weighting function gives most importance to the values of α , f and h at location x , and progressively less importance to these values at sites more distant from x . For points beyond the glacier boundary, the ice thickness and surface slope are set to 0. Once $B(x)$ has been evaluated at every point along the centre-line, the surface velocity $u_s(x)$ is predicted by referencing to a datum location x_0 where the surface velocity u_{obs} is known:

$$u_s(x) = u_{obs}(x_0) \exp(B(x) - B(x_0)) \quad (3)$$

In equation (3), the predicted surface velocity is not calculated directly as in equation (1), but is determined from the enhancement of motion at a point caused by the difference in ice conditions from the datum state. By experimenting with each stake in turn as the datum, we find that the best fit between measured and predicted velocities is obtained using stake 6. The values of ice thickness, surface slope and f are all close to the centre-line average at this stake (Fig. 4.4), and the small difference between summer and winter velocities suggests that surface motion is dominated by ice deformation (Fig. 4.3). When stake 6 is used as the datum there is generally a good fit between measured and predicted velocities between stakes 1-9 in the accumulation and upper ablation areas, although velocities are greatly under-predicted between stakes 10-20 in the lower ablation area (Fig. 4.6). Use of other stakes in the accumulation area as the datum also produces a generally good fit over the upper glacier and an under-prediction over the lower glacier. In contrast, the use of stakes in the ablation area as the datum produces velocities which are very much higher than observed (by 2x or more) in the accumulation area, and a generally poor fit to the measured motion over most of the ablation area.

Results obtained using longitudinal coupling lengths of 2, 3 and 4 times the local ice thickness are shown in Fig. 4.6, with the best fit provided by $l = 4.0 h$. With longitudinal coupling lengths of greater than $4h$, local variability tends to be lost and there is no further significant reduction in the magnitude of the residuals. Kamb and Echelmeyer (1986) state that l/h is typically in the range 1 to 3 for temperate valley glaciers and 4 to 10 for ice sheets. The value of 4 is therefore a realistic value for John Evans Glacier, a large polythermal ice mass.

4.4.2.3 Predicted ice motion with longitudinal stresses and variability in ice temperature

Since the value of A is not included explicitly in equations (2) and (3), an implicit assumption is that the ice temperature at the datum point is the same as over the rest of the glacier. In reality, this assumption is unrealistic for polythermal glaciers as borehole temperature measurements show that ice temperatures can and do vary substantially along their length (Blatter, 1987; Blatter and Kappenberger, 1988). Consequently, an adjustment needs to be made to equation (2) to account for this variability. Based on the

linear influence of A on equation (1), a simple way to do this is to multiply the velocity at location x by the ratio of A at location x ($A(x)$) to A at the datum location ($A(x_0)$). Using the same method of incorporating deviations in α , f and h from the datum state outlined in equation (2) (Kamb and Echelmeyer, 1986), the calculation of $B(x)$ becomes:

$$B(x) = \int_{x-2l}^{x+2l} (n \ln(\alpha f) + (n+1) \ln h + \ln(A(x)/A(x_0))) (1 - |x'-x|/2l) dx' \quad (4)$$

The surface velocity at location x is recalculated using the new values of $B(x)$ in equation (3). When using this scheme, it is the change in ice temperature between the datum location and the point of interest that defines the degree to which the velocity field is modified. This is in contrast to the actual ice temperatures that modify the surface motion in equation (1). If we consider the temperatures described in the warm and cold scenarios in Section 4.4.2.1, these provide an initial estimate of a 3°C to 5°C mean ice temperature difference between the accumulation and lower ablation areas. We choose the values of A at -3°C as the upper end of this temperature range (i.e., lower ablation area; stakes 10-20) and -6°C and -8°C as the lower ends of this temperature range (i.e., accumulation and upper ablation areas; stakes 1-9), as these lie in the centre of the temperatures described by the warm and cold scenarios. The choice of different upper and lower temperatures with the same temperature range will produce slightly different results because the value of A is not a linear function of temperature.

Using a longitudinal coupling length of $4h$ and equation (4), it is clear that the predicted surface velocities are closer to the observed velocities when temperature variations are taken into account (Fig. 4.7). Predicted velocities with a 3°C temperature difference are still lower than observed between stakes 10 and 20, but are generally a good fit between stakes 1 and 9. With a 5°C temperature difference, predicted velocities are closer to observed between stakes 10 and 20, and remain a good fit between stakes 1 and 9. We also experimented with a 6°C temperature difference (i.e., -3°C at stakes 10-20, -9°C at stakes 1-9), but this results in over-prediction at stakes 15 and 16. The over-prediction at stakes 8 and 9 in all scenarios may be explained by the fact that these stakes

are not located on the same well-defined flowline as the other stakes, and are in an area where flow resistance due to flowline convergence is probably not accurately determined.

From these experiments, it is clear that we can not account for all of the observed winter ice motion between stakes 10 and 20 by deformation alone unless we over-predict the motion at stakes 15 and 16 (e.g., by increasing the temperature difference to 6°C). If we therefore take the scenario with a 5°C ice temperature difference as the ‘best fit’ to our observed data, we can only match the predicted to the observed winter velocities by imposing a basal motion anomaly over the lower ablation area. The distribution and magnitude of such an anomaly will now be investigated.

4.4.2.4 Predicted ice motion with basal motion

If we impose a basal motion anomaly at a point along the glacier centre-line, we need to account for how this anomaly will modify surface velocities both upglacier and downglacier from its origin. If we assume that the length scales of this longitudinal coupling are similar to those imposed by variations in ice deformation, we can follow the suggestion by Kamb and Echelmeyer (1986), and add to the existing source term in equation (4):

$$B(x) = \int_{x-2l}^{x+2l} (n \ln(\alpha f) + (n+1) \ln h + \ln(A(x)/A(x_0)) + \ln(1 + u_b/u_d))(1 - |x'-x|/2l) dx' \quad (5)$$

where u_b/u_d is the ratio of basal motion to internal deformation. As before, equation (3) is used to recalculate the surface velocity from the value of $B(x)$ in equation (5). As stated by Kamb and Echelmeyer (1986), this method is a basic *ad hoc* way of accounting for the longitudinal stresses imposed by basal motion, but still provides a useful first attempt at determining the influence of basal motion on surface velocity.

Since equation (5) requires *a priori* knowledge of u_d to calculate u_b/u_d , we use the value of u_d calculated from equation (4) with a longitudinal coupling length of $4h$ and an ice temperature of -8°C at stakes 1-9, and -3°C at stakes 10-20. The only exception is at locations where the predicted ice deformation is very low, as this would produce very high values of u_b/u_d that could bias the results. At these locations (the 400 m closest to the

glacier terminus where the ice is very thin), the ice deformation rate is set to 1 m a^{-1} . Results from areas very close to the terminus should therefore be treated with greater scepticism than results from the rest of the centre-line. A final solution to equation (5) is reached by iterating with different values of u_b until the predicted surface motion most closely matches observations.

Fig. 4.8a shows the basal motion that needs to be imposed to best reproduce the measured surface motion in winter. There is a rapid onset to basal motion between stakes 10 and 11, with basal velocities of up to 7 m a^{-1} between stakes 11-14 and 18-20, and little or no basal motion between stakes 15-17. The inferred basal motion distribution is broadly consistent with our current knowledge of the basal hydrological conditions at John Evans Glacier. As discussed by Copland and Sharp (in press), the area beneath stakes 11-14 is overdeepened by up to 50 m in comparison to surrounding basal topography (Fig. 4.2). High residual bed reflection powers from radio-echo sounding measurements in May suggest that basal water is present in this area prior to the initiation of surface melt, which implies that basal water is stored overwinter in the overdeepening. In addition, rapid conduit closure at the end of the summer melt season is expected beneath stakes 15-17 due to high surface slopes and thick ice there. This would lead to basal water being trapped beneath stakes 11-14 after it reaches the glacier bed via the moulins between stakes 9 and 10 at the end of the summer. A peak in winter basal motion between stakes 11-14 is therefore consistent with the available hydrological evidence. The inferred high conduit closure rates and low residual bed reflection powers from radio-echo sounding are also consistent with the suggestion that there is little or no basal motion beneath stakes 15-17 in the winter.

Beneath stakes 18-20, there is evidence that water is present at the glacier bed throughout the year. The thermal dam at the glacier margin likely traps basal water behind it at the end of the previous summer, a suggestion supported by the progressive increase in residual bed reflection power towards the glacier terminus in radio-echo sounding records (Copland and Sharp, in press). As at stakes 11-14, most of these measurements were made before the onset of surface melting, implying that basal water is present throughout the winter beneath this part of the glacier. Further evidence for the overwinter storage of subglacial water is provided by water chemistry (Skidmore and

Sharp, 1999; K. Heppenstall, pers. comm.). The first water to be released from the glacier after the thermal dam breaks in the summer has a very high EC ($>400 \mu\text{S cm}^{-1}$), and contains ionic species such as Li^{2+} that are indicative of long water:rock contact times at the glacier bed and are not present at detectable levels later in the melt season. In contrast, water that is released later in the summer is more dilute ($\text{EC} < 200 \mu\text{S cm}^{-1}$), and contains more suspended sediment, indicative of more rapid subglacial water flow and lower water:rock contact times. All of these independent sources of evidence support the contention that subglacial water is stored overwinter behind the glacier snout, and that basal motion could occur there during the winter.

In the summer, a much larger basal motion anomaly is necessary to recreate the observed surface motion field (using the same temperature distribution and longitudinal coupling length of $4h$ to determine ice deformation) (Fig. 4.8b). As in the winter, there is a sudden onset to basal motion over a short distance in the summer, although the onset is slightly further upglacier between stakes 9 and 10. The inferred basal motion rate of 20 m a^{-1} between stakes 10-14 would account for up to 75% of the total surface motion there, and is consistent with the large volumes of water reaching the glacier bed via the moulins between stakes 9 and 10 in the summer. The inferred basal motion decreases to 10 m a^{-1} between stakes 15-20, although it accounts for a progressively larger proportion of total surface motion towards the terminus. Although not shown in Fig. 4.8b, it is also possible that basal motion of up to 5 m a^{-1} occurs beneath stakes 6-10. However, this motion would be much lower than that occurring between stakes 10-20, and would not change the rapid increase in rates of basal motion between stakes 9 and 10.

To explain these summer basal motion patterns, we speculate that meltwater flow is channelised when it first enters the moulins between stakes 9 and 10, but that it soon becomes distributed as it reaches the overdeepening and is ponded. This would explain the high basal motion between stakes 10-14 as the distributed subglacial drainage system would likely produce high basal water pressures. As the subglacial water exits the overdeepening along a single overflow point, it would probably become channelised. The potential for channelisation is enhanced by the steep surface slopes over the terminus (Fig. 4.4), which would increase the heat dissipation from flowing water and enlarge any existing flow pathways. This would result in lower basal water pressures than in areas

where the flow is distributed, and provides an explanation for the lower rates of basal motion beneath stakes 15-20.

To assess the importance of basal motion in modifying ice deformation rates via longitudinal stresses, Fig. 4.8c compares the imposed ice deformation rates in equation (5) (i.e., before basal motion is introduced) to the ice deformation rates once basal motion is introduced. The new ice deformation rates are calculated from the difference between the total surface motion and imposed basal motion. From Fig. 4.8c, it is clear that ice deformation can be substantially modified in areas where there is basal motion. There is a general decrease in ice deformation in areas where there is high basal motion (e.g., stakes 11-14), and an increase in deformation where there is a change from an area of high to low or no basal motion (e.g., stakes 8-9 and 15-17). This is because areas of faster moving ice are slowed down by surrounding areas of more gradually moving ice. Similarly, areas of slow moving ice are accelerated by nearby areas of faster ice. This has the effect of expanding the surface effect of basal motion anomalies up to 2 km upglacier from their source, particularly in the summer.

4.5 CONCLUSIONS

From a simple analysis of the measured summer and winter surface centre-line velocity fields along John Evans Glacier, it appears that basal motion occurs throughout the year beneath the lower ablation area. The onset of basal motion occurs directly downstream from a set of moulins that provides the main source of water to the glacier bed in the summer. In the winter, peaks in basal motion occur where subglacial water storage is suggested by radio-echo sounding, subglacial flow reconstructions, and analysis of meltwater chemistry. In addition, radio-echo sounding suggests that the glacier bed is cold in the accumulation area where observed surface velocities can be explained solely by ice deformation, and warm in the ablation area where basal motion needs to be introduced to account for the observed velocities. Long stresses are important at the glacier, and a longitudinal coupling length of four times the local ice thickness provides the best fit between predicted and observed surface motion. Long stresses have the effect of expanding the surface effect of basal motion anomalies up to 2 km upglacier from their source.

To confirm our conclusions requires more detailed 2D and 3D modelling, together with borehole drilling to measure basal motion, basal water pressures and englacial ice temperatures. Future work could also assess the importance of spatial variations in longitudinal coupling related to spatial variations in ice temperature.

4.6 BIBLIOGRAPHY

Andreasen, J.-O., 1985. Seasonal surface-velocity variations on a sub-polar glacier in West Greenland. *J. Glaciol.*, **31**(109), 319-323.

Bingham, R., Nienow, P., Sharp, M., Boon, S. and Heppenstall, K. 2001. Dye-tracer studies of the hydrology of a High-Arctic polythermal valley glacier: implications for glacier motion. CGU/ESC Annual Meeting, Ottawa.

Blatter, H. 1987. On the thermal regime of an arctic valley glacier: a study of White Glacier, Axel Heiberg Island, N.W.T., Canada. *J. Glaciol.*, **33**(114), 200-211.

Blatter, H. and Kappenberger, G. 1988. Mass balance and thermal regime of Laika Ice Cap, Coburg Island, N.W.T., Canada. *J. Glaciol.*, **34**(116), 102-110.

Copland, L. and Sharp, M. 2000. Radio-echo sounding determination of polythermal glacier hydrology. In: *Eighth International Conference on Ground Penetrating Radar*, David Noon, Glen F. Stickley, Dennis Longstaff (eds.). SPIE Vol. **4084**, pp. 59-64.

Copland, L. and Sharp, M. *In press*. Mapping hydrological and thermal conditions beneath a polythermal glacier with radio-echo sounding. *J. Glaciol.* Accepted Jan. 2001.

Kamb, B. and Echelmeyer, K.A. 1986. Stress-gradient coupling in glacier flow: I. Longitudinal averaging of the influence of ice thickness and surface slope. *J. Glaciol.*, **32**(111), 267-284.

Hooke, R.LeB., Calla, P., Holmlund, P., Nilsson, M. and Stroeven, A. 1989. A 3 year record of seasonal variations in surface velocity, Storglaciären, Sweden. *J. Glaciol.*, **35**(120), 235-247.

Iken, A. 1974. Velocity fluctuations of an Arctic valley glacier, a study of the White glacier, Axel Heiberg Island, Canadian Arctic Archipelago. *Axel Heiberg Island Research Reports, Glaciology no. 5*. McGill University, Montreal.

Kamb, B. and Echelmeyer, K.A. 1986. Stress-gradient coupling in glacier flow: I. Longitudinal averaging of the influence of ice thickness and surface slope. *J. Glaciol.*, **32**(111), 267-284.

Nye, J.F. 1965. The flow of a glacier in a channel of rectangular, elliptic or parabolic cross-section. *J. Glaciol.*, **5**(41), 661-690.

Paterson, W.S.B. 1994. *The Physics of Glaciers (3rd ed.)*. Elsevier Science, Oxford.

Rabus, B.T. and Echelmeyer, K.A. 1997. The flow of a polythermal glacier: McCall Glacier, Alaska, U.S.A. *J. Glaciol.*, **43**(145), 522-536.

Skidmore, M.L. and Sharp, M.J. 1999. Drainage system behaviour of a High Arctic polythermal glacier. *Ann. Glaciol.*, **28**, 209-215.

Woodward, J., Sharp, M. and Arendt, A. 1997. The effect of superimposed ice formation on the sensitivity of glacier mass balance to climate change. *Ann. Glaciol.*, **24**, 186-190.

Zevenbergen, L.W. and Thorne, C.R. 1987. Quantitative analysis of land surface topography. *Earth Surf. Proc. Land.*, **12**, 47-56.

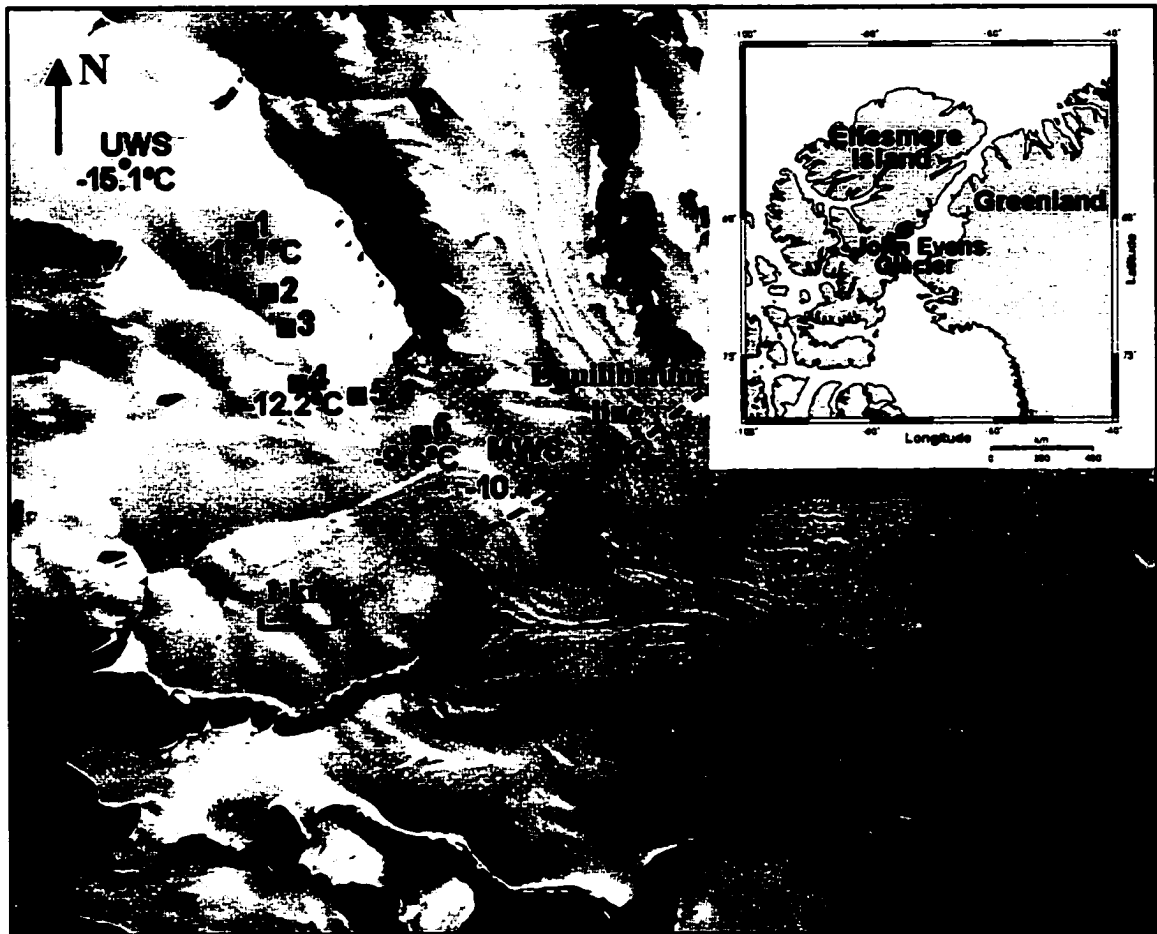


Figure 4.1 Location of John Evans Glacier (inset), and the centre-line velocity stake network superimposed on a Landsat 7 image from July 10, 1999. Squares indicate stakes measured by GPS, while circles indicate stakes measured by theodolite. LWS, MWS and UWS mark the lower, middle and upper weather stations, respectively. Temperatures mark ice temperatures at 15 m depth.

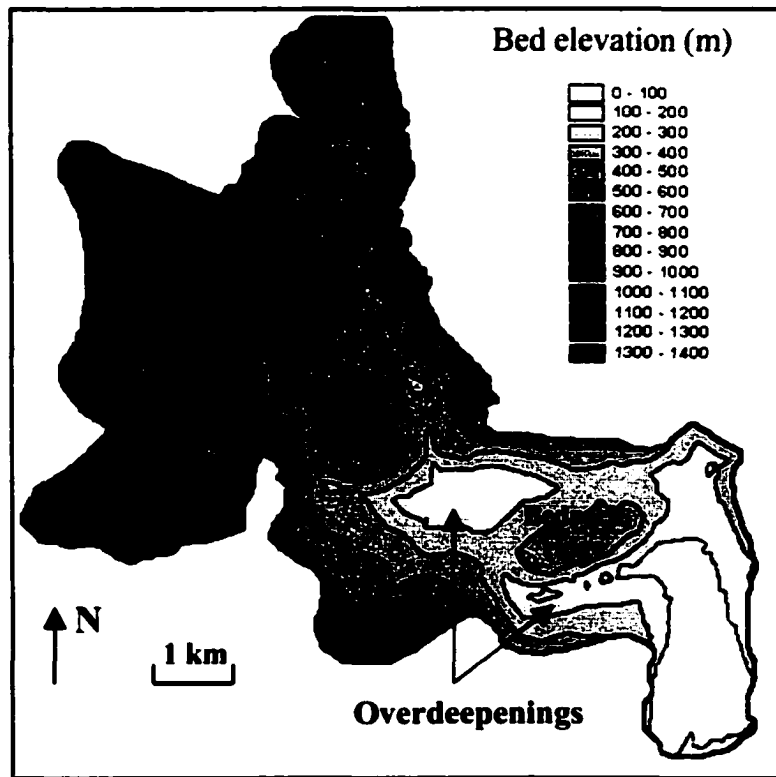


Figure 4.2 Bedrock topography at John Evans Glacier determined from radio-echo sounding (Copland and Sharp, in press)

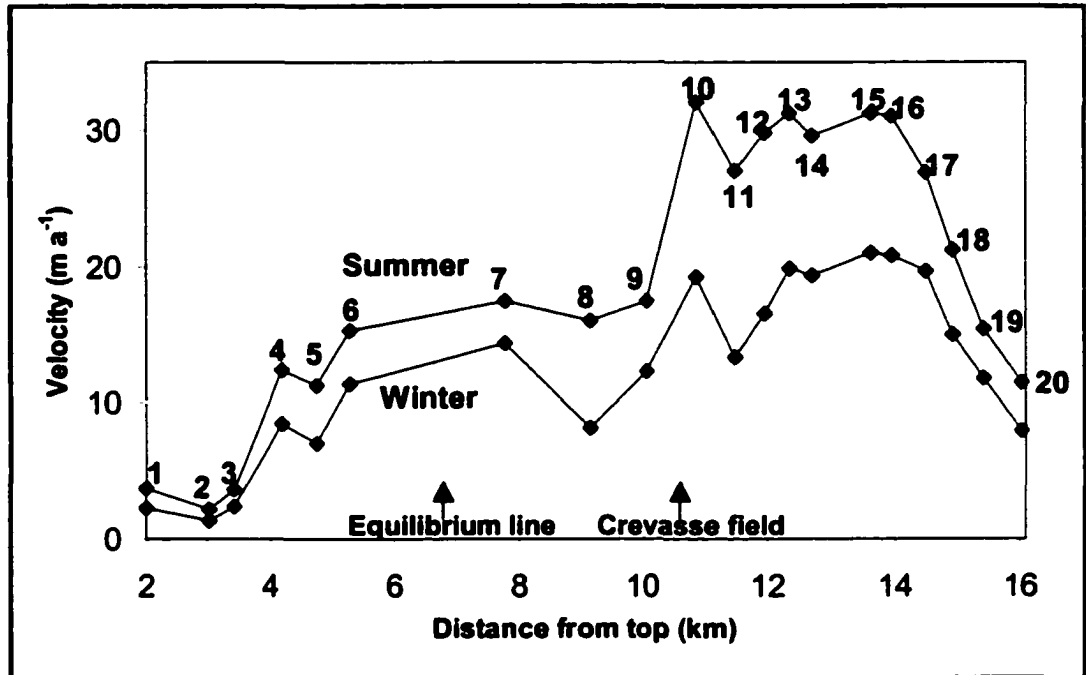


Figure 4.3 Measured summer and winter surface velocities along the centre-line network

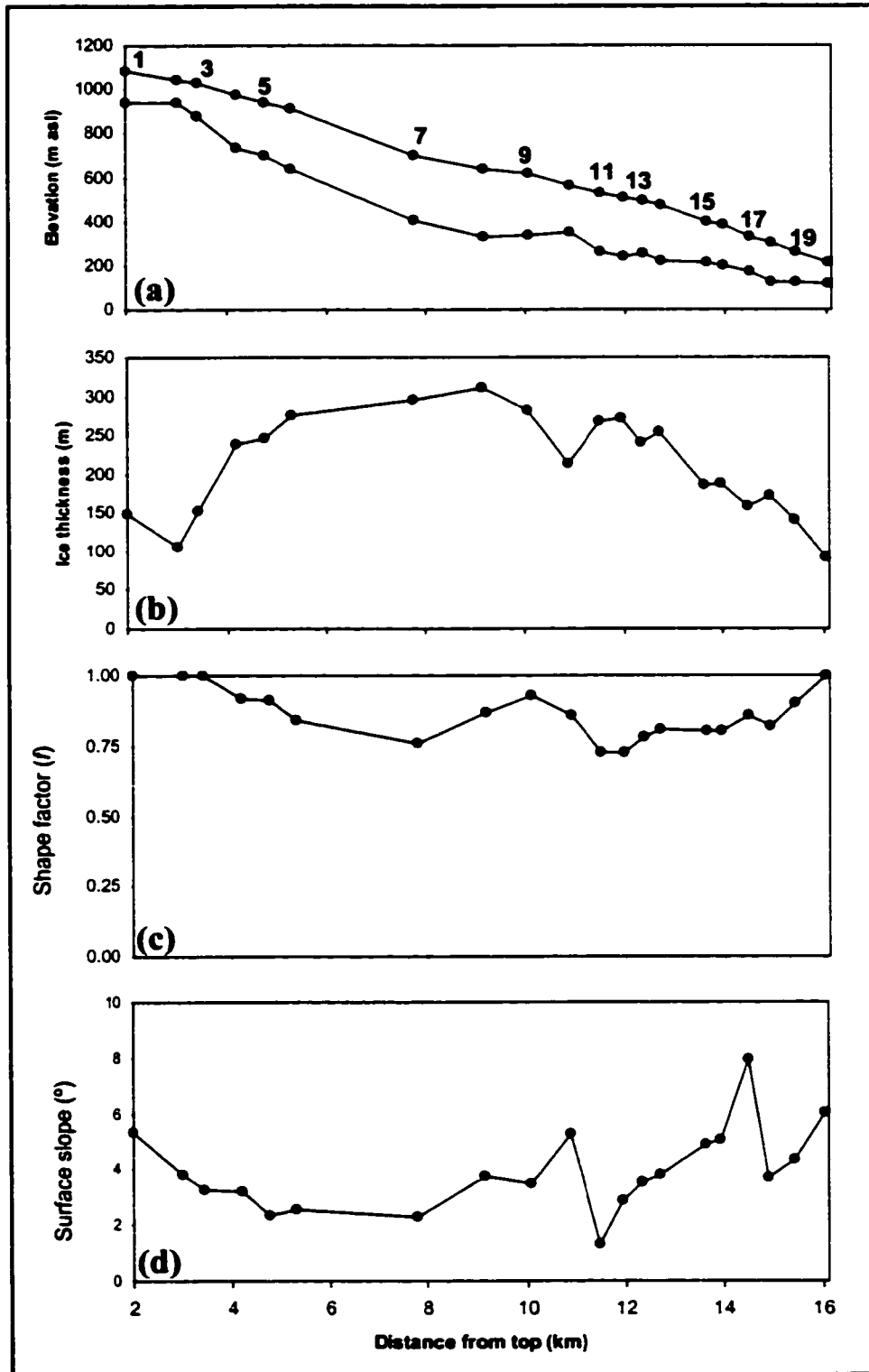


Figure 4.4 For the centre-line stake transect at John Evans Glacier: (a) surface and bed topography (b) ice thickness (c) shape factor f (d) surface slope angle

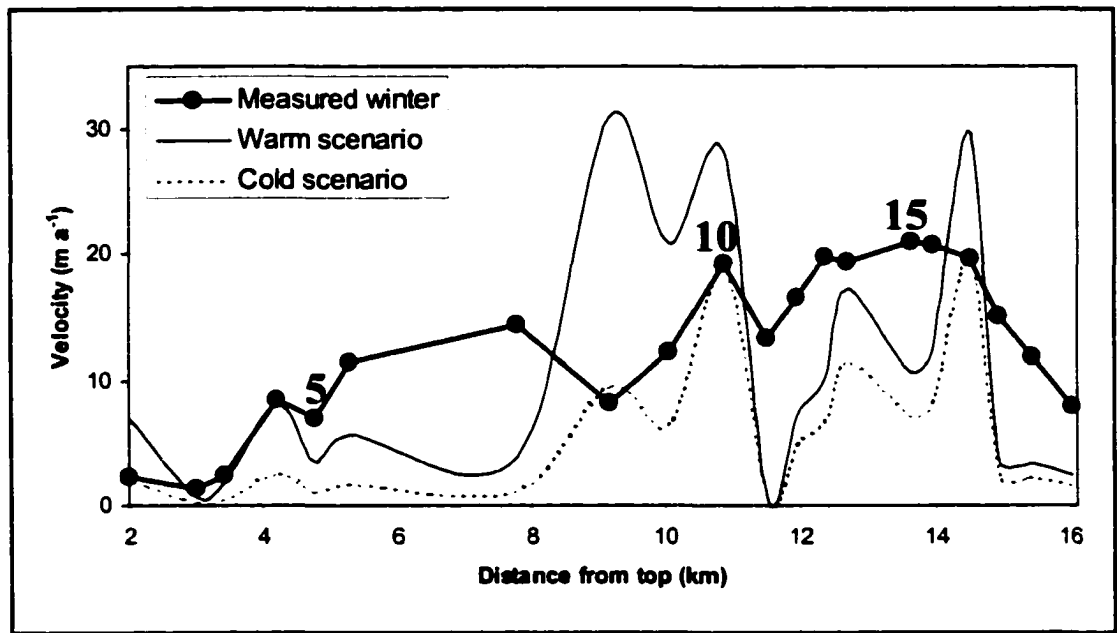


Figure 4.5 Comparison between measured and predicted surface velocities along the centre-line of John Evans Glacier from equation (1), without accounting for longitudinal stresses

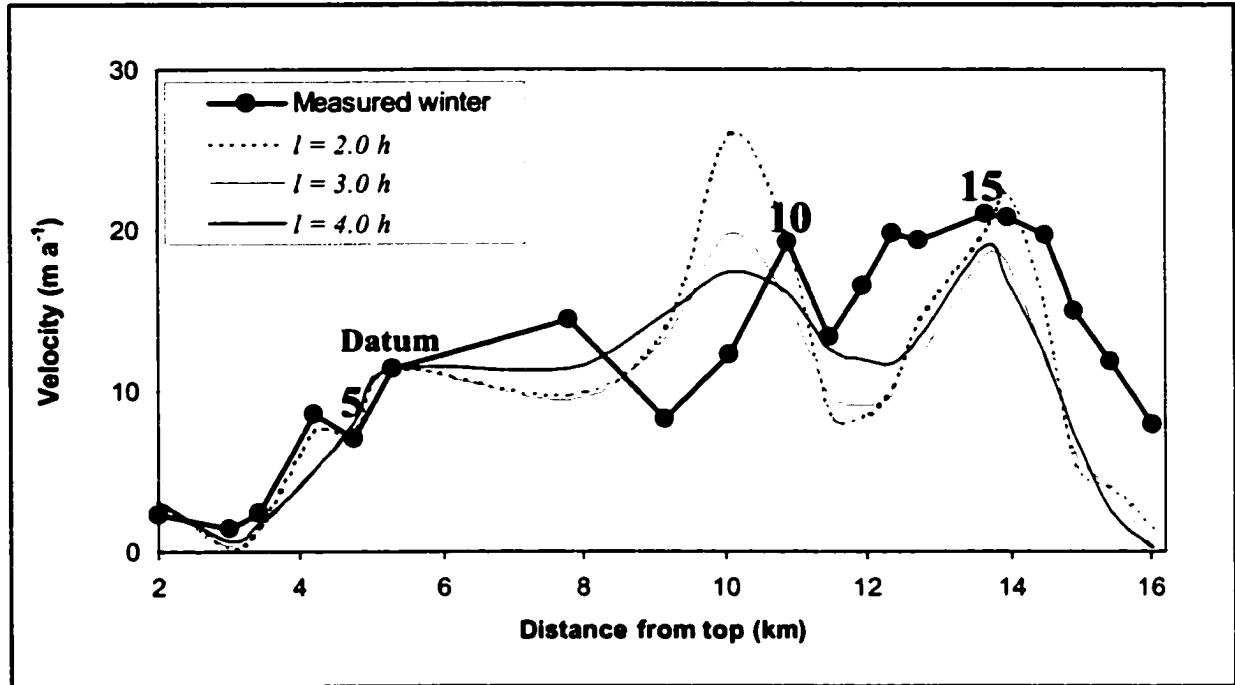


Figure 4.6 Comparison between measured and predicted surface velocities along the centre-line of John Evans Glacier from equations (2) and (3) for longitudinal coupling lengths of 2, 3 and 4 times the local ice thickness. Ice temperature variations are not taken into account. Each dot indicates a velocity stake. Stake 6 is used as the datum.

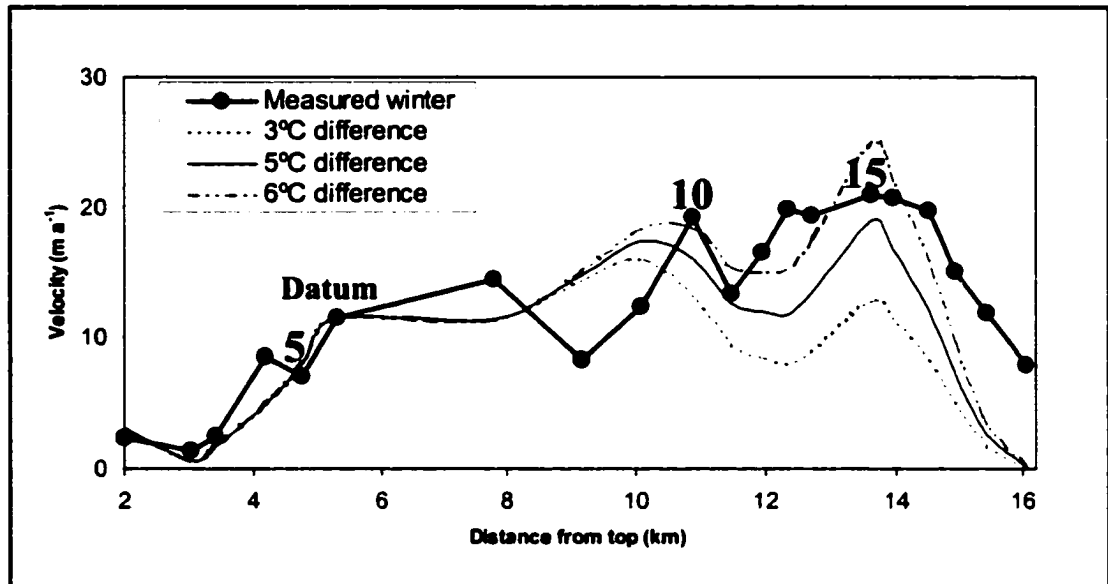


Figure 4.7 Comparison between measured and predicted surface velocities along the centre-line of John Evans Glacier from equations (4) and (3) for a longitudinal coupling length of $4h$. The differences indicate the difference in temperature between stakes 10-20 (-3°C) and stakes 1-9 (-6 , -8 or -9°C). Each dot indicates a velocity stake. Stake 6 is used as the datum.

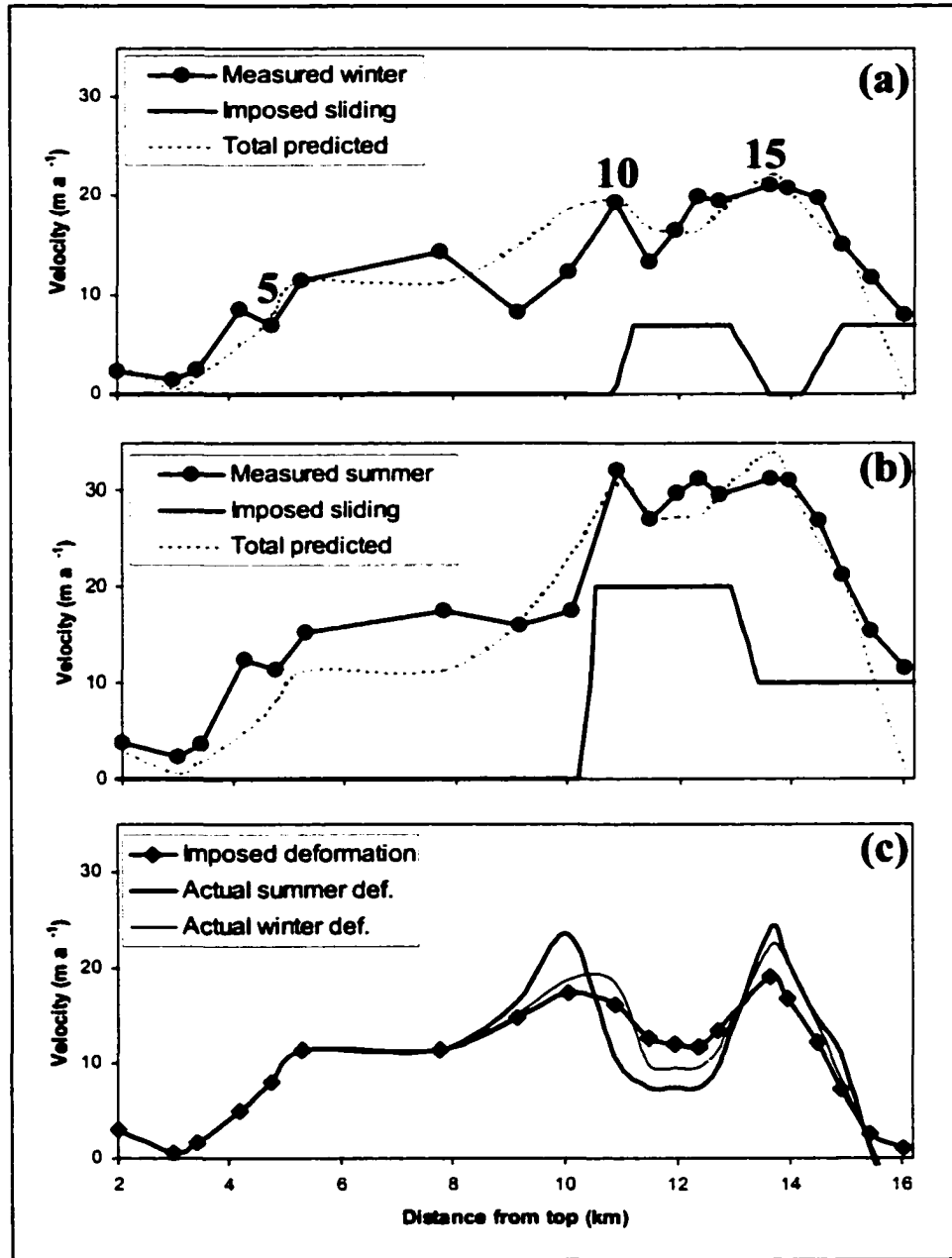


Figure 4.8 Comparison between measured and predicted surface velocities along the centre-line of John Evans Glacier from equations (5) and (3) for a longitudinal coupling length of $4h$ and the imposed basal sliding distribution shown in each figure: (a) in the winter (b) in the summer. (c) Comparison between imposed and actual ice deformation rates for the summer and winter. Differences are caused by the influence of basal sliding on longitudinal stresses. The imposed ice deformation is defined by the '5°C difference' line shown in Fig. 4.7.

CHAPTER 5

LINKS BETWEEN SHORT-TERM VELOCITY VARIATIONS AND THE SUBGLACIAL HYDROLOGY OF A POLYTHERMAL GLACIER

5.1 INTRODUCTION

The objectives of this study are to determine: (i) whether surface meltwater can penetrate cold ice to reach the bed of a polythermal glacier and affect its surface motion; (ii) whether high velocity events similar to those observed in temperate glaciers also occur in polythermal glaciers (and if they do, then when, how often, and how big are they?); (iii) the spatial distribution of surface velocity variations during ice motion events, and how these relate to the spatial distribution of subglacial drainage elements; and (iv) the cause of short-term motion events, and in particular the influence of time-varying water inputs and subglacial drainage system development and evolution.

Previous research on polythermal glaciers has shown that ice motion is generally faster during the summer than the winter in areas close to where there is water at the bed (Hooke et al., 1983; Andreasen, 1985; Rabus and Echelmeyer, 1997), with a strong correlation between hourly to daily high velocity events and basal water pressures (Iken, 1974). Little is currently known about the detailed flow dynamics of polythermal glaciers and the structure and evolution of their subglacial drainage systems, however, as most studies have been based on measurements with limited temporal or spatial resolution. Although we have a good knowledge of the relationships between the hydrology and dynamics of temperate glaciers (e.g., Willis, 1995), these studies are not directly applicable to polythermal glaciers due to their complex thermal structure. Since polythermal glaciers contain ice which is both at and below the pressure melting point, they have a subglacial hydrological system which differs from that of temperate glaciers because liquid water can exist in significant quantities only where the ice is warm. Consequently, a polythermal glacier may be expected to produce a different dynamic response to a given water input than a temperate glacier.

To improve on the resolution of previous studies, we established a network of up to 34 stakes over the terminus of polythermal John Evans Glacier, Ellesmere Island. Horizontal and vertical surface velocities were determined for successive two day periods throughout the summers of 1998 and 1999, and subglacial discharge was monitored by water level sensors in streams that entered and exited the subglacial drainage system. The location of subglacial drainage passageways was determined from the form of the subglacial hydraulic potential surface, and from spatial variability in returned bed power in radio-echo sounding records (Copland and Sharp, 2000, in press). In addition, records from a weather station located on the glacier terminus were used to place changes in surface motion and glacier hydrology in a climatological context. Three geophones in the lower reaches of the glacier provided further information about the timing, location and relative magnitude of basal motion events.

5.1.1 John Evans Glacier

John Evans Glacier is a 165 km² polythermal valley glacier on the east coast of Ellesmere Island, Nunavut, Canada (79°40'N, 74°30'W; Fig. 5.1). It terminates on land, and ranges in elevation from 100 m to 1200 m asl, with the long term equilibrium line at ~750-850 m asl. Ice depths reach a maximum of 400 m over the upper ablation area, and average 100-250 m in the lower ablation area where the ice motion measurements were made (Copland and Sharp, in press). For the period 1997-99, mean annual air temperatures near the equilibrium line were -15.2°C.

High bed reflection powers in radio-echo sounding records indicate warm ice at the bed throughout most of the ablation zone, except along the glacier margins and where the ice is thin (Copland and Sharp, in press). Low bed reflection powers and 15 m borehole temperatures of -9.5 to -15.1°C in the accumulation and upper ablation areas suggest that the remaining ice is cold. Similar ice temperature patterns have been measured at McCall Glacier, Alaska (Rabus and Echelmeyer, 1997), and at White Glacier, Axel Heiberg Island (Blatter, 1987).

The main melt season typically occurs between early June and early August. During this time, meltwater from approximately 40% of the surface area of the glacier flows into moulins in a crevasse field at the top of the terminus region (personal

communication from S. Boon, 2001; Fig. 5.2). Tracking of this water with dye tracing, together with the large increase in suspended sediment content and electrical conductivity (EC) of the water as it passes through the glacier, suggests that most of it is routed subglacially (Bingham et al., 2001). In the early summer, the meltwater is trapped at the glacier bed behind a thermal dam at the snout (Skidmore and Sharp, 1999). The first meltwater release of the summer typically occurs as an artesian fountain on the glacier surface and/or an upwelling in the proglacial area. The proglacial upwelling subsequently evolves into a channelised outlet at the ice/bed interface as the thermal dam is fully breached. The first water to be released has high total solute concentrations ($EC > 400 \mu\text{S cm}^{-1}$), is somewhat turbid, and contains ionic species (Na^+ , K^+ and Si) that are products of silicate weathering (Skidmore and Sharp, 1999). Within a few days, the water becomes more dilute, although solute concentrations are still much higher than for supraglacial water. These observations suggest that the first water to be released has been stored for a long period (possibly overwinter), while later water has been transmitted more rapidly through the subglacial system. Initial release dates have varied between June 22 and July 11 since the start of observations in 1994.

5.2 MEASUREMENTS

5.2.1 Ice motion

Twenty-one velocity stakes were established over the lowermost 2 km of John Evans Glacier in 1998, and a further 13 were added in 1999 to expand the network 1 km upglacier (Fig. 5.2). The terminus region was chosen as it is easily accessible, there are surrounding cliffs to locate survey stations on bedrock, and subglacial water flow is present (Skidmore and Sharp, 1999; Bingham et al., 2001; Copland and Sharp, in press). Reflecting prisms were mounted on 3 m stakes frozen into the ice surface, which were periodically redrilled before surface melting made them unstable. When an old stake was still frozen into the ice surface, a new one was added next to the old one and the prism moved across.

When the weather conditions were favourable, the position of each prism was measured daily in the summers of 1998 and 1999 with a Geodimeter 540 total station theodolite. To reduce errors, the data were subsampled to determine stake displacements

over periods of two days or longer. The exact time between surveys was recorded and used to convert the displacements to velocities in cm day^{-1} (24 hrs). Velocity patterns were interpolated over the entire terminus region from the point measurements at the stakes. All interpolations were completed with the 'v4' interpolation routine in Matlab, which is based on biharmonic spline interpolation (Sandwell, 1987). Interpretations of velocity patterns are made only for areas where stakes are present. For the purposes of our discussion, the lower terminus is defined as the area south of the upper geophone (UG on Fig. 5.2), and the upper terminus is defined as the area north of the upper geophone.

5.2.2 Ice motion errors

When a stake is surveyed, errors in positioning arise from instrument limitations, and from operator and external factors. Instrument limitations relate to the accuracy and resolution of the distance and angle sensors in the theodolite. From the Geodimeter technical specifications, uncertainties in the distance measurements amount to $\pm (2 \text{ mm} + 3 \text{ mm per km})$, which equates to $\pm 5 \text{ mm}$ over a typical survey distance of 1 km. Angle measurements are made to a resolution of 2 arc seconds, which equates to a maximum potential error of ± 1 arc second, or $\pm 4.8 \text{ mm}$ over a distance of 1 km.

Operator and external errors arise from factors such as variations in air temperature and pressure between surveys, instrument drift during a survey, and the ability to position the theodolite in the same position at a station from one survey to the next. The effect of air pressure and temperature on the distance measurements was accounted for by inputting these values into the theodolite at the start of each survey. The effect of refraction on the vertical angle measurements was also accounted for in our calculations by using the standard corrections stated in the Geodimeter user's manual. To account for instrument drift, the reference marker was resurveyed after every 7 or fewer stake measurements. The stake positions were corrected according to these values, with the drift assumed to be linear between resurveys. Improvements in the positioning of the theodolite were made in 1999 by making the top plates of the tripods horizontal. This meant that the Geodimeter base screws did not have to be adjusted between surveys, and reduced errors related to the movement of the theodolite between stations.

In our discussion we evaluate total errors (as we cannot distinguish between internal and external sources), and discuss three types:

(i) *Position error*: this is the error in determining the location of a stake during a single survey, and is given in units of +/- cm.

(ii) *Displacement error*: this is the error in determining the displacement of a stake between two surveys. It can be calculated by summing the position errors from the two surveys and/or from two or more independent measurements of the displacement of a stake. It is expressed in units of +/- cm.

(iii) *Velocity error*: this is the displacement error adjusted for the time between surveys, and is given in units of +/- cm day⁻¹. As the measurement period increases, the velocity error decreases, as we can be more sure that the measured displacement is real.

In 1998, all stakes were surveyed independently from each of two stations located ~100 m apart. For each measurement period, this provided two measures of the displacement of each stake, and the displacement error was calculated from the difference between these and the mean displacement of the stake for that survey. Separate velocity error calculations were then made for each stake for each two day measurement period and are displayed in the velocity figures discussed later. For the entire 1998 measurement period, mean velocity errors for all stakes are +/- 1.09 cm day⁻¹ in horizontal motion and +/- 0.63 cm day⁻¹ in vertical motion.

In 1999, the displacement of each stake was determined once for each measurement period from surveys at a single station. This is because one of the 1998 stations was moved to a new location in 1999 to enable surveying of the stakes that were added that year. This meant that each stake could then only be seen from one station. To evaluate errors, we measured the location of each stake at least twice from the same station during each survey in July and August 1999. On a given day, the difference between the two or more measurements of a stake and its mean location provide a position error. The position errors from the surveys at the start and end of a measurement period then provide the displacement error, which in turn provides the velocity error. The velocity errors are calculated separately for every stake for every two day measurement period in July and August 1999. The seasonal mean is used for the surveys prior to day

184 (i.e., mainly June) as each stake was only surveyed once then. For summer 1999, mean velocity errors for all stakes are $\pm 0.61 \text{ cm day}^{-1}$ in horizontal motion and $\pm 0.16 \text{ cm day}^{-1}$ in vertical motion.

Detailed discussion focuses on the 1999 measurements due to the lower velocity errors, improved spatial coverage, and better records from supporting instruments such as water pressure sensors. For comparison, the characteristics of high velocity events in 1998 are outlined where they are above velocity error estimates. For the few measurements where data are missing, velocities were determined by interpolating from adjacent stake measurements over the same period, or by using velocities from 1 or 2 day periods which overlapped the period of interest. In our discussion, the stated start and end time of velocity events is approximate due to the 2 day resolution of our measurements. This also leads to underestimation of the true magnitude of velocity changes when a single event crosses two measurement periods, and/or when an event is shorter than a measurement period.

5.2.3 Geophones

In 1997, three geophones were installed at a depth of 5 m along the centre of the terminus: a lower geophone close to the snout, a middle geophone $\sim 1 \text{ km}$ from the snout, and an upper geophone $\sim 2 \text{ km}$ from the snout (Fig. 5.2). The 4.5 Hz geophones were interfaced to a Campbell Scientific data logger, which recorded the number of seismic events above a defined gain, and output a total every hour (in 1998) or two hours (in 1999). A gain of 2000 was used, since it provided a good compromise between sensitivity and the recording of background noise in tests at Trapridge Glacier (personal communication from J. Kavanaugh, 1997). The geophone records did not allow for the accurate location of individual seismic events, but did allow for general positioning by noting which geophones recorded activity.

Given the lack of volcanic activity or active faults in this area, we assumed that most detected events had a glacial origin. Previous studies have shown strong correlations between ice motion, water discharge and seismicity at other glaciers (Iken and Bindshadler, 1986; Raymond et al., 1995). This is because ice fracturing commonly occurs during periods of rapid ice motion due to changes in the internal stress

distribution. In addition, basal sliding may produce seismic events as the ice moves across the glacier bed.

5.2.4 Weather stations

Three weather stations were installed on John Evans Glacier in 1996. The lower station is located next to the middle geophone in the centre of the terminus at ~200 m asl (Fig. 5.2). In this study, we use hourly measurements of air temperature and surface albedo from this station to quantify changes in weather and surface conditions. Rates of surface lowering recorded by an ultrasonic depth gauge (UDG) also provide an indication of meltwater production and availability. These records are not corrected for differences in surface density between ice and snow, so provide only a general measure of surface melt rates.

5.2.5 Discharge records

To provide an indication of the relative discharge entering the subglacial drainage system in 1999, pressure sensors were installed upstream of the main crevasse field in an ice-marginal lake and in two locations in a supraglacial stream draining from the lake (Fig. 5.2). To monitor the flow of water from the glacier, a pressure sensor was installed in the main subglacial stream shortly after it exited the snout. This proglacial record is approximate due to frequent bed aggradation and erosion around the sensor, and the need to move the sensor because of channel migration. The sensors were not calibrated to discharge, so each record was rendered dimensionless by scaling it between the highest and lowest water levels over the period of interest.

5.2.6 Subglacial flow routing

To assess the relationship between ice motion and basal hydrology, we reconstructed subglacial flow routing from the subglacial hydraulic potential surface using the method of Shreve (1972) (Copland and Sharp, 2000). Reconstructions were made for assumed basal water pressures between 0 and 100% of ice overburden pressure, but no significant differences were found in predicted flow routing. This indicates that subglacial topography, rather than variations in ice thickness, provide the dominant

control on basal water flow at John Evans Glacier. The drainage pattern presented here is for a basal water pressure of 100% of ice overburden pressure.

5.2.7 Residual vertical motion (cavity opening)

To determine the importance of basal processes in accounting for the measured vertical velocities, we calculated residual vertical motion (w_c) for each of our surveys. This describes the unexplained vertical motion after vertical strain and the horizontal movement along a sloping bed have been accounted for, and is commonly attributed to basal cavity formation. In reality, it may be caused by any unaccounted for basal process such as a change in the dilatancy of subglacial till or the size of subglacial drainage channels. We calculated w_c from (Hooke et al., 1989):

$$w_c = w_s - u_b \tan \beta - \dot{\epsilon}_{z\bar{z}} h \quad (1)$$

where w_s = measured Lagrangian vertical motion at the surface, u_b = horizontal basal motion, β = bed slope (negative when the ice is flowing downhill), $\dot{\epsilon}_{z\bar{z}}$ = measured vertical strain rate at the surface (which is assumed to be equal to $\overline{\dot{\epsilon}_{z\bar{z}}}$, the depth averaged vertical strain rate), and h = ice thickness. The difference in w_c between overwinter 1999/2000 and the period of interest was determined to provide an estimate of the basal processes occurring solely during a high velocity event.

For our calculations we used the measured values of u_s (horizontal surface motion) interpolated to a regular 100 m grid, rather than u_b , since we do not have any measurements of basal motion. Ice thickness was determined by radio-echo sounding (Copland and Sharp, in press), and interpolated to the same 100 m grid. Bed slope was calculated from the change in bed elevation across the four grid points to the N, E, S and W of the point of interest. By assuming incompressibility, the vertical strain rate at the surface was determined from the surface horizontal strain rates ($\dot{\epsilon}_{z\bar{z}} = -\dot{\epsilon}_{x\bar{x}} - \dot{\epsilon}_{y\bar{y}}$), which were calculated from the gradient in surface horizontal motion between adjacent grid points. Previous studies (Balise and Raymond, 1985; Hooke et al., 1989) indicate

that $\dot{\epsilon}_{\neq s}$ is not the same as $\dot{\epsilon}_{\neq}$ at depth, however, so we need to evaluate the impact of possible variations in $\dot{\epsilon}_{\neq}$ on calculations of w_c . If there is no cavity opening ($w_c = 0$) and there is no change in $\dot{\epsilon}_{\neq}$ with depth, then for a given ice depth we can define the range of values that $\dot{\epsilon}_{\neq s}$ must fall between if $0 < u_b < u_s$ (Hooke et al., 1989; Mair et al., in review). Values of $\dot{\epsilon}_{\neq s}$ outside of these limits define conditions when $\dot{\epsilon}_{\neq}$ must increase or decrease with depth relative to $\dot{\epsilon}_{\neq s}$. For negative values of β (i.e., the usual case when the glacier is flowing downhill):

(i) No change in $\dot{\epsilon}_{\neq}$ with depth relative to $\dot{\epsilon}_{\neq s}$: $(w_s) \leq (\dot{\epsilon}_{\neq s} h) \leq (w_s - u_s \tan\beta)$

(ii) Decrease in $\dot{\epsilon}_{\neq}$ with depth relative to $\dot{\epsilon}_{\neq s}$: $(\dot{\epsilon}_{\neq s} h) > (w_s - u_s \tan\beta)$

(iii) Increase in $\dot{\epsilon}_{\neq}$ with depth relative to $\dot{\epsilon}_{\neq s}$: $(\dot{\epsilon}_{\neq s} h) < (w_s)$

For positive values of β (i.e., the more unusual case when the glacier is flowing uphill, such at the downstream end of an overdeepening):

(i) No change in $\dot{\epsilon}_{\neq}$ with depth relative to $\dot{\epsilon}_{\neq s}$: $(w_s) \geq (\dot{\epsilon}_{\neq s} h) \geq (w_s - u_s \tan\beta)$

(ii) Decrease in $\dot{\epsilon}_{\neq}$ with depth relative to $\dot{\epsilon}_{\neq s}$: $(\dot{\epsilon}_{\neq s} h) > (w_s)$

(iii) Increase in $\dot{\epsilon}_{\neq}$ with depth relative to $\dot{\epsilon}_{\neq s}$: $(\dot{\epsilon}_{\neq s} h) < (w_s - u_s \tan\beta)$

Basal vertical motion is relatively unlikely in scenarios (i) and (ii) as surface vertical motion can be accommodated entirely by vertical strain and/or basal sliding in these situations. Basal vertical motion is more likely in scenario (iii) if the surface vertical motion is higher than can be plausibly explained by the increase in $\dot{\epsilon}_{\neq}$ with depth relative to $\dot{\epsilon}_{\neq s}$. Hooke et al. (1989) argued that a value of $\dot{\epsilon}_{\neq s} h$ of $\sim 3\text{mm day}^{-1}$

less than w_s (when β is negative) is indicative of cavity opening in an ice depth of ~ 100 m. Classification of the glacier into areas where each of these cases holds for each velocity event therefore helps in defining areas where basal vertical motion is likely to have occurred.

5.3 RESULTS

5.3.1 Long-term velocities

Velocities were calculated for winter 1998/99 (day 205, 1998 to day 146, 1999) and 1999/2000 (day 214, 1999 to day 161, 2000) to provide a measure of the 'background' velocities against which short-term variations can be compared. Only the 1999/2000 velocities are presented here as the records cover a larger area, and are very similar to the 1998/99 records. For the stakes which were measured in both winters, differences average 0.14 cm day^{-1} in horizontal motion and 0.57° in horizontal direction. The velocities are well defined due to the low errors related to the long period between measurements, with a mean horizontal velocity of 3.47 cm day^{-1} for winter 1999/2000 (Fig. 5.3a). Vertical velocities are low during the winter, reaching a maximum of approximately -0.5 cm day^{-1} in an area of steep surface slopes between the upper and lower terminus (Fig. 5.3b).

To provide information about the spatial scale of forcing mechanisms and how these change over time, we used principal components analysis (PCA) to define groups of stakes with coherent patterns of horizontal velocity variation. From analysis of all two day horizontal velocity data over days 164.71-211.98, 1999 (Table 5.1), PCA identified eight principal component factors with eigenvalues >1 (Table 5.2). When the 34 velocity stakes are grouped based on their loadings on these factors, two main clusters are identified: factor 1 generally groups stakes from the lower terminus, while factor 2 generally groups stakes from the upper terminus (Table 5.3; Fig. 5.3a). There is a transition zone around stakes 20-26 where there is not a spatially coherent grouping of the stakes on one factor (Table 5.3; Figs. 5.2 and 5.3). Grouping with more than the first two factors subdivides these two clusters into smaller groups that are not as spatially contiguous. In addition, the factor scores for the other factors are generally low and do not load on the velocity events. Since most of the variance in horizontal motion is

explained by the first two factors (60.7%), and the loadings on these factors cluster stakes into populations that act differently during the high velocity events (Fig. 5.4d), we use these groupings in our discussion of the 1999 short-term velocity data. PCA could not be performed on the 1998 velocity data due to the shorter summer measurement period and relatively small number of stakes.

5.3.2 1999 short-term velocity events

5.3.2.1 Event 1/99: Days 184.60 – 189.04

This event encompasses two measurement periods, days 184.60-186.94 and days 186.94-189.04, during which mean horizontal motion was almost 100% above overwinter levels at 6.72 cm day^{-1} (Fig. 5.4a). There was little change in either mean horizontal or mean vertical motion between these periods (Figs. 5.4 and 5.5), so the mean velocities from the two periods combined are presented in Fig. 5.6.

The relative increases in horizontal motion during Event 1/99 were spatially non-uniform: the mean velocity of stakes in the lower terminus increased by 110% above overwinter levels, while that of stakes in the upper terminus increased by 75% (Figs. 5.4b and 5.4c). Compared to overwinter, there was an expansion of the region of high velocities towards the glacier margins, particularly over the lower terminus and close to the snout (Figs. 5.3a, 5.6a and 5.6b). The largest absolute velocity anomalies of up to 6 cm day^{-1} occurred over the upper terminus close to where winter velocities were highest, and close to the predicted subglacial drainage routing. Over the centre of the lower terminus, horizontal velocities were an almost constant 3 cm day^{-1} above overwinter levels (Fig. 5.6b), and there was a marked rotation of the surface velocity vectors towards the west (compare Fig 5.6a with Fig. 5.3a). The rotation of the velocity vectors increased towards the glacier snout, where it reached $>45^\circ$ at some stakes.

There was little change in vertical motion from overwinter levels, with most vertical velocities close to 0 cm day^{-1} (Figs. 5.5 and 5.6c). Residual vertical motion was also generally low, and there was only a relatively small area over the lower terminus where cavity opening would be possible (i.e., where an increase in ϵ_{zz} with depth relative to ϵ_{zz} could have occurred). Within this area there was uplift up to $+3 \text{ cm day}^{-1}$ at one

stake, although this limited spatial occurrence makes it difficult to determine whether the changes were real (Fig. 5.6d).

Event 1/99 occurred at the end of the first week of intense summer melting and the first exposure of ice over the terminus. There was a short lag between the period of high air temperatures and the period of high horizontal velocities, with a drop in air temperatures approximately 2 days prior to the decrease in ice motion at the end of Event 1/99 (Fig. 5.7a). By the start of the event the albedo had fallen to 40% (Fig. 5.7b), which defines the approximate boundary between a snow and ice covered surface (Paterson, 1994). Surface melting had been occurring for approximately one month prior to Event 1/99 (Fig. 5.7c), although much of this melt may have refrozen in the cold snowpack. The rate of surface lowering was continuously positive during the event (Fig. 5.7d). The ice marginal lake drained rapidly during Event 1/99 (Fig. 5.8), and the first major discharges from the snout were observed in the form of outburst floods shortly after the lake drainage during the overnight period between days 185 and 186. The timing of these drainage events is approximate and based on field observations as the water pressure sensors were not installed until day 188.

The largest geophone activity of the summer was recorded at the lower and middle geophones on day 186 (Figs. 5.9b and 5.9c). A further three smaller periods of activity were recorded at each of these geophones before the end of Event 1/99, while no unusual counts were recorded at the upper geophone during this time (Fig. 5.9a).

5.3.2.2 Event 2/99: Days 196.60 – 198.88

Event 2/99 saw large horizontal velocity increases at most stakes compared to both the preceding measurement period (days 193.92-196.60), and to overwinter levels (Figs. 5.3, 5.4, 5.10 and 5.11). The horizontal velocity increases were highly spatially variable, with the increase in velocity of the stakes over the upper terminus much higher than that of the stakes over the lower terminus (Figs. 5.4b and 5.4c). On a local scale, the horizontal velocity increases were low and only a little above overwinter levels over the western part of the lower terminus (Fig. 5.11b). In contrast, the largest velocity increases of the year occurred over the western part of the upper terminus, with velocity anomalies up to 18 cm day^{-1} , or $\sim 400\%$ above overwinter levels (Figs. 5.11a and 5.11b). These

anomalies were localised above the predicted areas of subglacial water flow, and decreased rapidly towards the glacier margins. In addition, there was a strong rotation in horizontal velocity vectors towards the glacier margin in this area compared to both the overwinter and preceding measurement periods (Figs. 5.3a, 5.10a, 5.11a). The rotation was greatest for stakes closest to the glacier edge, which consists of unsupported ice walls up to 100 m high.

There were rapid and dramatic changes in vertical motion during and immediately prior to Event 2/99, particularly over the upper terminus (Fig. 5.5). There was strong vertical uplift at most stakes during the event, compared to significant vertical lowering in the preceding measurement period (Figs. 5.5, 5.10c and 5.11c). For the lower terminus stakes, vertical velocities averaged $-1.42 \text{ cm day}^{-1}$ in the preceding period and $+0.95 \text{ cm day}^{-1}$ during Event 2/99 (Fig. 5.5b). For the upper terminus stakes, mean vertical velocities were $-1.09 \text{ cm day}^{-1}$ in the preceding period and $+3.53 \text{ cm day}^{-1}$ during Event 2/99 (Fig. 5.5c). As with horizontal motion, these patterns are highly spatially variable, with largest changes occurring over the western part of the upper terminus (Figs. 5.10c and 5.11c). At many stakes in this region the change in rate of vertical motion was $>10 \text{ cm day}^{-1}$ between Event 2/99 and the preceding period.

Cavity opening would have been possible over only a limited area in the period prior to Event 2/99 (Fig. 5.10d), but could have occurred over the entire lower terminus and the western part of the upper terminus during the event (Fig. 5.11d). In particular, the residual vertical motion of $>15 \text{ cm day}^{-1}$ along the area of predicted subglacial drainage over the western upper terminus is higher than can be explained by changes in vertical strain rate with depth, and makes it likely that cavity opening occurred in this area.

During the two days prior to Event 2/99, a storm system reduced air temperatures to below freezing and produced new snowfall. Temperatures increased rapidly on day 197, and stayed well above freezing for the remainder of the event (Fig. 5.7a). The albedo sensor records the increase in albedo due to the new snowfall (Fig. 5.7b), and the UDG records net accumulation during this period (Figs. 5.7c and 5.7d). Surface melting restarted rapidly once the weather warmed, with the highest sustained surface lowering rates of the summer occurring throughout Event 2/99 (Fig. 5.7d).

All the water pressure sensors showed a clear response to these weather changes (Fig. 5.8). Discharges were low at all locations during the cool period prior to Event 2/99, with diurnal variability disappearing due to the reduction in meltwater supply. As air temperature and surface melt increased at the onset of Event 2/99, water levels at the sensors rose. Surface lowering rates peaked on day 198.1, the lake and supraglacial streams peaked between days 198.7 and 198.8, while the proglacial stream peaked on day 199.1 (Figs. 5.7d and 5.8). The largest number of events of the summer were recorded at the upper geophone on day 198 during Event 2/99 (Fig. 5.9). Smaller events, with counts well below those during Event 1/99, were also recorded at the middle and lower geophones.

5.3.3 1998 short-term velocity events

5.3.3.1 Event 1/98: Days 180.71 – 184.71

The lower number of stakes and higher measurement errors in summer 1998 mean that only one event can be conclusively identified (Fig. 5.12). Event 1/98 covers the two measurement periods over days 180.71-182.71 and 182.71-184.71, with the largest and most significant horizontal velocity increases during the second half of the event. Consequently, only the velocity patterns from this second period are plotted here (Fig. 5.13).

The mean horizontal velocity for the 15 stakes present during Event 1/98 was 4.96 cm day^{-1} during the first half of the event, and 8.20 cm day^{-1} during the second half (Fig. 5.12a). This compares to a mean overwinter velocity for these stakes of 3.27 cm day^{-1} . As with the other events, the high standard deviation in horizontal velocity shows that the increases were not spatially uniform (Fig. 5.12a). The highest velocity increases of up to 14 cm day^{-1} occurred over the eastern part of the lower terminus (Fig. 5.13b). This area of high horizontal velocities is defined by at least 4 stakes, and the velocity increases are well above error estimates. As in Event 1/99, there was also a rotation in the velocity vectors towards the west that was greatest close to the glacier snout (compare Fig. 5.13a with Fig. 5.3a).

Vertical velocities varied little and were close to overwinter values during Event 1/98 (Figs. 5.12b and 5.13c). Of the 15 stakes measured during the event, most had

vertical velocities of 0 to -1 cm day^{-1} . The residual vertical motion was centered around 0 cm day^{-1} , and there were few areas where cavity opening could have occurred (Fig. 5.13d).

As in Event 1/99, Event 1/98 occurred during the first week of the exposure of bare ice over the terminus as albedos dropped below 40% (Fig. 5.14b). Air temperatures were higher than at any previous time in 1998, and remained high and well above freezing throughout (Fig. 5.14a). Approximately 95 cm of surface lowering occurred in the month prior to Event 1/98 as the surface snow cover was melted (Fig. 5.14c), and surface lowering rates reached their highest sustained levels of the summer during the event (Fig. 5.14d).

Associated with these surface changes, Event 1/98 coincides with the 1998 initiation of subglacial water outflow from the terminus. This occurred via an englacial outlet close to the glacier bed at the snout, and via an artesian fountain over the lower eastern terminus (white dot on Figs. 5.13b and 5.13d). Both of these features were first observed on day 180, and the artesian fountain reached its peak during days 182-184, before declining around day 186 (Fig. 5.15). The fountain reached heights of 5 m, and brought large volumes of turbid and high EC water to the glacier surface through an ice thickness of 70 m (measured by radio-echo sounding; Copland and Sharp, in press). This suggests a subglacial origin for the water, and indicates that basal water pressures were at least 120% of ice overburden pressure over the lower terminus. Longitudinal fracturing of the ice surface was also observed around the artesian fountain, with most fracturing occurring when the fountain first released. This fracturing was recorded by a small number of events at the middle geophone on day 180.25, and a large number of events at the lower geophone on day 180.46 (Fig. 5.16). No significant activity was recorded at the upper geophone at this time.

5.4 DISCUSSION

From our measurements, it is evident that short-term velocity events are associated with periods of rapidly increasing meltwater inputs to the subglacial drainage system. This most commonly occurs in the early melt season at the onset of subglacial

drainage (Events 1/98 and 1/99), but may also occur later in the melt season during a warm period after a prolonged cold spell (Event 2/99).

5.4.1 Early season events

The early season events are characterized by air temperatures which were warmer than at any previous time during the year, a change from a snow covered to an ice covered surface, and high rates of surface lowering (melting) (Figs. 5.7 and 5.15). These changes are important hydrologically as a bare ice surface melts faster than higher albedo snow, and allows rapid transmission of surface melt to supraglacial lakes and streams, and in turn to the glacier interior via the crevasse field at the top of the terminus region. The outburst flood at the snout typically occurs within 24 hours of these first supraglacial water inputs to the subglacial drainage system. This is probably because the new water input pressurizes the existing subglacial reservoir beneath the lower terminus, and drives outlet development at the snout. Evidence for pressures above ice overburden levels is provided by the formation of the artesian fountain, while the high EC of the first water to be released is indicative of overwinter storage. This outlet development provides an explanation for the high counts recorded at the lower and middle geophones during Events 1/99 and 1/98 (Figs. 5.9 and 5.16).

High horizontal velocities would be expected at this time because high basal water pressures reduce basal friction and enhance basal motion. This was particularly apparent during Event 1/98, when there was a close association between the area of highest horizontal velocity anomalies and the location of predicted subglacial water flow and the artesian fountain (Fig. 5.13). The increasingly large rotation of the horizontal velocity vectors towards the snout can be explained by the compression of the fast moving warm-based ice against the slow moving cold-based ice at the margins. Since the cold-based ice deforms slowly and probably does not slide, the warm ice would be deflected away from the snout. The PCA scores for the factor 1 stakes reached their highest values during Event 1/99 (Fig. 5.4d) as the largest horizontal velocity changes of the year occurred over the lower terminus.

Using the calculations of limits on vertical strain rates discussed in Section 5.2.7, there were few areas where $\dot{\epsilon}_{zz}$ could have increased with depth relative to $\dot{\epsilon}_{zzs}$ during Events 1/98 and 1/99, which means there are few areas where basal cavity opening could have occurred (Figs. 5.6d and 5.13d). Even within those areas where cavity opening was possible, the residual vertical motion was generally low. This provides information about the basal motion mechanisms that must have occurred at this time. The small vertical changes during Events 1/98 and 1/99 make it unlikely that the high horizontal velocities were driven by basal cavity formation or the over-pressurization of subglacial drainage channels as these would have produced vertical uplift. A more likely scenario is that the horizontal velocity increases were produced by widespread lubrication of the interface between the ice and underlying basal sediment as water became backed up behind the thermal dam at the snout. This would result in only small changes in vertical motion, and is supported by the gradual increase in positive residual bed reflection power towards the snout in early season radio-echo sounding records (which is indicative of the widespread presence of water at the bed; Copland and Sharp, in press).

The larger horizontal and vertical velocity anomalies close to the snout during Event 1/98 than Event 1/99 suggests that the early season changes in basal hydrology were weaker in 1999. We hypothesize that this could be due to: (a) an incomplete closure during winter 1998/99 of large drainage channels which breached the thermal dam during the warm summer of 1998, and/or (b) a larger rate of supraglacial water input to the glacier interior in 1998 than 1999. Without further field evidence, we are unable to distinguish between these scenarios.

5.4.2 Mid-season event

Event 2/99 occurred after a prolonged cold period during which there was a cessation of surface melting (Fig. 5.7), and low water levels in all monitored streams (Fig. 5.8). It is likely that subglacial water pressure dropped at this time as meltwater stopped flowing to the glacier interior. Depending on the subglacial drainage configuration, this would result in the closure by ice and/or basal sediment deformation of basal cavities or subglacial channels, and/or compaction of the glacier bed due to a

reduction in the porosity of basal sediment. These processes would likely be greater in areas where the ice is thicker. While we do not know which of these processes occurred beneath John Evans Glacier, they all produce the same net effect of surface lowering. This provides an explanation for the negative vertical motion close to the subglacial drainage pathways in the period prior to Event 2/99 (Fig. 5.10c), with the largest magnitudes over the NW part of the upper terminus where the ice thicknesses are greatest (200-250 m) (Copland and Sharp, in press). Over the lower terminus the vertical motion was still negative, but of lower magnitude, in an area where the ice thicknesses are 100-150 m. A reduction in basal water pressure would also increase basal drag and account for the relatively low horizontal velocities at this time (Fig. 5.10b).

Melt resumed as the weather warmed at the start of Event 2/99 (Fig. 5.7), with a rapid rise in water levels at all sensors (Fig. 5.8). The water levels reached their highest levels of the summer at the sensors in the supraglacial streams, which suggests that a large meltwater pulse entered the subglacial drainage system via the crevasse field at the top of the terminus. This is the area where subglacial drainage would be most restricted, however, due to the high closure rates during the preceding cold period. The inability of the drainage system to effectively transmit these large meltwater volumes would result in high basal water pressures and reduced basal drag. We see high residual vertical motion and high horizontal velocities localized along the main drainage axis over the NW terminus at this time, which suggests that these basal hydrological changes cause basal cavity opening and are a major influence on surface motion patterns. The strong rotation in the velocity vectors in this area is probably due to diversion of flow towards the unsupported ice walls of the glacier margin as the fast moving ice of the upper terminus pushed against the slower moving ice downglacier. As expected, horizontal motion was less over the lower terminus due to the reduced closure of the subglacial drainage system during the preceding cold period, and the fact that the meltwater pulse would be damped by the restricted flow through the upper terminus. The high counts registered at the upper geophone during Event 2/99 (Fig. 5.9), together with the high PCA factor 2 scores at this time (Fig. 5.4d), support the fact that this velocity event was focused over the upper terminus.

5.5 CONCLUSIONS

Measurements over two years at a high Arctic polythermal glacier demonstrate that surface meltwater can penetrate significant thicknesses (> 200 m) of cold ice to reach the glacier bed and affect horizontal and vertical surface velocities. Horizontal surface velocities across the entire glacier terminus are higher in the summer than the winter, with two to four-day very high velocity events (up to 400% above overwinter levels) occurring during periods of rapidly increasing meltwater input to the glacier interior.

In the early summer, these high velocity events occur at the onset of supraglacial water flow to the glacier bed, which causes high basal water pressures and the release of basal water from a thermally dammed reservoir behind the glacier snout. Horizontal velocity increases are greatest over the lower terminus at this time, with a close correlation between the areas of largest velocity increase and predicted subglacial flow routing in 1998. The small changes in vertical motion during the early season events suggests that they are driven by a widespread lubrication of the glacier bed as meltwater becomes trapped behind the thermal dam at the snout.

High velocity events may also occur later in the summer if melt suddenly resumes after a cold period, as happened in 1999. Low horizontal velocities and negative vertical motion in the cold period indicate that the subglacial drainage system effectively closed down when the meltwater inputs from the glacier surface stopped. When melt resumed, horizontal and vertical velocities increased rapidly and were greatest over the upper terminus where the ice was thickest and closure greatest in the preceding cold period. Within this area, the largest velocity changes were highly localised over distances of less than one ice thickness and occurred in close proximity to areas of large basal cavity opening and predicted locations of subglacial drainage. This suggests that the basal motion mechanisms were very different during Event 2/99 than during the early season events, with cavity opening and the over-pressurization of subglacial channels the dominant mechanism once the subglacial drainage system has had a chance to develop through the melt season.

These observations indicate a strong relationship between polythermal glacier hydrology and ice motion over small spatial and temporal scales that has not been resolved in previous studies based on a single longitudinal stake network and/or

infrequent velocity measurements. There is a close correlation between changes in meltwater inputs to the glacier interior and short-term high velocity events, with the largest velocity increases typically localized along drainage axes.

5.6 BIBLIOGRAPHY

Andreasen, J.-O., 1985. Seasonal surface-velocity variations on a sub-polar glacier in West Greenland. *J. Glaciol.*, **31**(109), 319-323.

Balise, M.J. and Raymond, C.F. 1985. Transfer of basal sliding variations to the surface of a linearly viscous glacier. *J. Glaciol.*, **31**(109), 308-318.

Bingham, R., Nienow, P., Sharp, M., Boon, S. and Heppenstall, K. 2001. Dye-tracer studies of the hydrology of a High-Arctic polythermal valley glacier: implications for glacier motion. CGU/ESC Annual Meeting, Ottawa.

Blatter, H. 1987. On the thermal regime of an arctic valley glacier: a study of White Glacier, Axel Heiberg Island, N.W.T., Canada. *J. Glaciol.*, **33**(114), 200-211.

Copland, L. and Sharp, M. 2000. Radio-echo sounding determination of polythermal glacier hydrology. *In: Eighth International Conference on Ground Penetrating Radar*, David Noon, Glen F. Stickley, Dennis Longstaff (eds.). *SPIE Vol. 4084*, pp. 59-64.

Copland, L. and Sharp, M. *In press*. Mapping thermal and hydrological conditions beneath a polythermal glacier with radio-echo sounding. *J. Glaciol.*

Gordon, S., Sharp, M., Hubbard, B., Smart, C., Ketterling, B. and Willis, I. 1998. Seasonal reorganization of subglacial drainage inferred from measurements in boreholes. *In: Sharp, M., Richards, K.S. and Tranter, M. (eds.) Glacier Hydrology and Hydrochemistry*. John Wiley and Sons Ltd., Chichester.

Hooke, R. LeB., Brzozowski, J. and Bronge, C. 1983. Seasonal variations in surface velocity, Storglaciären, Sweden. *Geogr. Ann.*, **65A**(3-4), 263-277.

Iken, A. 1974. Velocity fluctuations of an Arctic valley glacier, a study of the White glacier, Axel Heiberg Island, Canadian Arctic Archipelago. *Axel Heiberg Island Research Reports, Glaciology no. 5*. McGill University, Montreal.

Iken, A. 1977. Variations of surface velocities of some Alpine glaciers measured at intervals of a few hours. Comparison with Arctic glaciers. *Z. Gletscherkd. Glazialgeol.*, **13**(1/2), 23-35.

Iken, A. and Bindschadler, R.A. 1986. Combined measurements of subglacial water pressure and surface ice velocity of Findelengletscher, Switzerland: conclusions about drainage system and sliding mechanism. *J. Glaciol.*, **32**(110), 101-117.

Mair, D., Sharp, M. and Willis, I. *In review*. Influence of cavity opening on subglacial drainage system evolution and configuration: Haut Glacier d'Arolla, Switzerland. *J. Glaciol.*

Murray, T. and Clarke, G.K.C. 1995. Black-box modeling of the subglacial water system. *J. Geophys. Res.*, **100**(B7), 10231-10245.

Paterson, W.S.B. 1994. *The Physics of Glaciers (3rd ed.)*. Elsevier Science Ltd., Oxford.

Rabus, B.T. and Echelmeyer, K.A. 1997. The flow of a polythermal glacier: McCall Glacier, Alaska, U.S.A. *J. Glaciol.*, **43**(145), 522-536.

Raymond, C.F., Benedict, R.J., Harrison, W.D., Echelmeyer, K.A. and Sturm, M. 1995. Hydrological discharges and motion of Fels and Black Rapids Glaciers, Alaska, U.S.A.: implications for the structure of their drainage systems. *J. Glaciol.*, **41**(138), 290-304.

Sandwell, D.T. 1987. Biharmonic spline interpolation of GEOS-3 and SEASAT altimeter data. *Geophys. Res. Letters*, **2**, 139-142.

Skidmore, M.L. and Sharp, M.J. 1999. Drainage system behaviour of a High Arctic polythermal glacier. *Ann. Glaciol.*, **28**, 209-215.

Willis, I.C. 1995. Intra-annual variations in glacier motion: a review. *Prog. Phys. Geogr.*, **19**(1), 61-106.

| | Stake number | | | | | | | | | | | | | | | | | | | | | | | | | | | | | | | | | |
|---------------|--------------|------|------|------|------|------|------|------|------|------|------|------|------|------|------|------|------|-------|-------|------|-------|-------|------|------|-------|-------|-------|-------|-------|-------|-------|-------|-------|-------|
| 1999 day | 1 | 2 | 3 | 4 | 5 | 6 | 7 | 8 | 9 | 10 | 11 | 12 | 13 | 14 | 15 | 16 | 17 | 18 | 19 | 20 | 21 | 22 | 23 | 24 | 25 | 26 | 27 | 28 | 29 | 30 | 31 | 32 | 33 | 34 |
| 164.71-166.71 | 4.52 | 1.83 | 1.44 | 1.68 | 1.50 | 2.34 | 1.81 | 5.12 | 2.36 | 1.94 | 5.95 | 4.28 | 3.80 | 2.49 | 4.43 | 5.64 | 5.78 | 6.12 | 5.85 | 2.35 | 6.80 | 6.67 | 3.44 | 5.62 | 6.13 | 5.18 | 2.67 | 6.16 | 6.21 | 5.85 | 8.00 | 7.19 | 2.09 | 8.53 |
| 166.71-168.79 | 3.43 | 2.57 | 2.37 | 1.74 | 2.91 | 2.47 | 3.24 | 1.71 | 2.97 | 4.11 | 1.20 | 0.94 | 3.71 | 3.12 | 3.67 | 2.98 | 4.79 | 5.12 | 5.98 | 2.80 | 5.65 | 5.57 | 2.10 | 2.61 | 5.29 | 5.39 | 2.97 | 2.17 | 1.67 | 7.36 | 2.76 | 1.29 | 6.02 | 5.55 |
| 168.79-170.67 | 3.60 | 4.35 | 6.59 | 2.48 | 3.46 | 3.22 | 4.79 | 1.36 | 2.88 | 3.60 | 3.41 | 2.90 | 4.30 | 4.14 | 4.89 | 5.32 | 5.37 | 6.46 | 6.89 | 3.50 | 6.25 | 7.98 | 3.50 | 3.96 | 7.39 | 8.08 | 4.39 | 5.20 | 4.52 | 1.90 | 2.13 | 2.68 | 4.13 | 4.30 |
| 170.67-172.71 | 3.02 | 1.77 | 1.95 | 1.20 | 5.35 | 2.77 | 0.57 | 2.09 | 3.42 | 2.82 | 3.71 | 2.39 | 4.95 | 3.68 | 3.99 | 1.34 | 3.89 | 4.24 | 3.80 | 1.79 | 4.52 | 3.62 | 0.52 | 1.78 | 4.56 | 3.34 | 2.74 | 5.33 | 8.18 | 0.47 | 5.01 | 6.57 | 1.58 | 5.22 |
| 173.61-176.68 | 2.63 | 2.38 | 2.14 | 1.84 | 3.92 | 2.91 | 2.77 | 1.56 | 2.75 | 2.54 | 1.18 | 1.95 | 3.53 | 3.33 | 4.03 | 4.11 | 4.72 | 5.21 | 5.17 | 2.65 | 5.23 | 4.79 | 1.68 | 2.89 | 5.18 | 6.41 | 2.05 | 4.39 | 6.23 | 0.93 | 3.55 | 5.43 | 0.65 | 4.97 |
| 176.68-178.63 | 2.74 | 3.62 | 3.87 | 2.06 | 3.70 | 3.53 | 1.53 | 0.84 | 3.02 | 5.12 | 5.18 | 3.83 | 4.18 | 3.88 | 5.04 | 5.55 | 4.94 | 6.22 | 6.26 | 2.76 | 6.38 | 5.58 | 2.63 | 3.98 | 6.03 | 7.15 | 1.54 | 3.85 | 5.33 | 1.16 | 4.06 | 5.28 | 1.44 | 5.65 |
| 178.63-180.68 | 3.21 | 2.95 | 2.67 | 1.92 | 4.93 | 1.40 | 2.26 | 2.12 | 2.16 | 2.36 | 1.18 | 4.14 | 3.96 | 3.59 | 3.15 | 2.46 | 5.86 | 5.25 | 6.35 | 3.04 | 6.13 | 7.72 | 3.89 | 4.49 | 7.13 | 6.11 | 2.89 | 6.82 | 5.27 | 1.12 | 5.00 | 5.12 | 2.02 | 4.32 |
| 180.68-182.83 | | | | | | 1.92 | 6.17 | | | 6.48 | 5.46 | 2.94 | 4.95 | 4.39 | 5.86 | 5.62 | 4.12 | 6.18 | 3.86 | 3.42 | 6.71 | 6.13 | 3.08 | 4.05 | 6.15 | 5.89 | 1.68 | 2.99 | 4.22 | 1.46 | 4.68 | 7.22 | 1.68 | 6.08 |
| 182.83-184.80 | 2.46 | | | 2.12 | 2.71 | | | 1.75 | 2.58 | | | | | 1.48 | 2.57 | | 7.15 | 2.94 | 3.93 | 5.45 | 6.09 | 4.24 | 4.62 | 7.28 | | 4.83 | 5.29 | 5.96 | 2.21 | 9.57 | 7.36 | 1.53 | 7.61 | |
| 184.80-186.84 | 6.38 | 5.48 | 5.68 | 4.33 | 6.34 | 6.48 | 4.06 | 3.30 | 4.77 | 7.67 | 6.57 | 5.13 | 6.59 | 7.99 | 8.31 | 9.32 | 9.88 | 8.42 | 10.48 | | 7.26 | 6.50 | 4.36 | 6.29 | 8.20 | | 3.12 | 8.63 | 10.12 | 2.08 | 7.19 | 9.71 | 3.02 | 7.93 |
| 186.84-189.04 | 5.68 | 4.25 | 4.80 | 5.05 | | 5.37 | 3.39 | 3.44 | 4.52 | 6.47 | 6.13 | 6.52 | 7.71 | 5.33 | 7.43 | 7.25 | 7.82 | 11.56 | 9.44 | 3.96 | 10.24 | 8.88 | 3.18 | 5.83 | 10.31 | 9.94 | 5.37 | 8.42 | 11.67 | 3.52 | 10.04 | 10.30 | 1.78 | 10.09 |
| 189.04-190.77 | 3.68 | 3.05 | 7.21 | 3.11 | | 5.21 | 4.83 | 1.83 | 5.45 | 4.90 | 5.02 | 5.07 | 4.99 | 4.49 | 6.21 | 7.11 | 6.93 | 9.00 | 6.16 | 2.12 | 7.21 | 6.41 | 3.10 | 6.34 | 8.02 | 8.83 | 3.20 | 9.11 | 8.23 | 3.60 | 7.06 | 7.44 | 2.25 | 9.32 |
| 190.85-192.79 | 2.50 | 2.72 | 2.58 | 2.58 | 2.85 | 3.61 | | | | | | | 4.04 | 3.10 | 4.58 | 3.21 | 5.55 | | 5.24 | 5.76 | | 7.39 | | | 3.07 | | 5.17 | 5.43 | 6.65 | 4.78 | 9.00 | 8.60 | 7.56 | 9.92 |
| 193.82-196.60 | | | 2.49 | 2.18 | 2.96 | 3.09 | 1.88 | 1.40 | 2.75 | 4.64 | 2.91 | 2.81 | 4.50 | 4.08 | 5.51 | 5.80 | 6.20 | 7.60 | 6.68 | 4.33 | | 7.46 | 1.80 | 4.01 | 8.61 | 7.67 | 4.06 | 7.99 | 9.59 | 0.74 | 6.49 | 9.07 | 0.23 | 6.14 |
| 196.60-198.88 | | | 5.57 | 3.93 | 3.31 | | 5.30 | 2.23 | 4.34 | 4.64 | 5.99 | 4.05 | 7.77 | 4.85 | 7.61 | 7.48 | 7.96 | 8.71 | 10.93 | 6.78 | 11.33 | 11.69 | 4.45 | 5.77 | 9.75 | 10.99 | 10.52 | 17.45 | 21.24 | 12.68 | 23.85 | 21.68 | 13.50 | |
| 198.88-200.83 | 3.27 | 5.09 | 4.84 | 3.01 | 4.92 | | 4.60 | 2.04 | 4.50 | 5.23 | 2.82 | 6.12 | 6.90 | | 6.98 | | 7.03 | 8.09 | | | 7.58 | | 3.22 | 5.28 | 6.51 | | | | | | | | | |
| 200.83-202.79 | 3.68 | 5.59 | 4.90 | 2.93 | 2.30 | | 1.92 | 0.91 | 2.23 | 4.84 | 5.29 | 2.54 | 4.46 | 3.75 | 5.36 | 4.94 | 5.97 | 6.67 | 8.19 | 3.54 | 8.12 | 8.07 | 2.15 | 4.09 | 5.89 | | 0.67 | 2.73 | 7.53 | 6.44 | 4.14 | 8.08 | 1.95 | 6.30 |
| 202.79-204.88 | 2.20 | 1.57 | 2.84 | 1.91 | 3.03 | 1.74 | 1.84 | 1.07 | 2.56 | | 1.39 | 2.69 | | 3.83 | | 5.18 | 6.21 | 7.90 | 7.29 | 4.35 | 6.54 | 7.65 | 2.79 | 4.82 | 7.76 | 7.43 | 5.19 | 6.22 | 8.95 | 1.88 | 7.91 | 9.96 | 1.02 | 8.77 |
| 204.88-206.79 | 4.21 | 9.76 | 8.87 | 4.31 | 3.55 | 6.28 | 4.75 | 2.21 | 4.25 | 5.47 | 5.98 | 4.77 | 4.53 | 4.32 | 4.90 | 5.51 | 5.75 | 6.94 | 5.66 | 3.61 | 9.22 | 8.86 | 3.11 | 5.17 | 10.07 | 11.92 | 2.56 | 7.92 | 10.28 | 1.87 | 10.01 | 10.07 | 2.48 | 10.24 |
| 206.79-208.92 | 1.12 | 3.90 | 3.65 | 1.71 | 2.80 | 2.33 | 3.25 | 1.30 | 2.73 | 3.90 | 2.71 | 3.78 | 4.86 | 4.45 | 5.28 | 5.61 | 6.34 | 7.07 | 8.54 | 3.01 | 6.94 | 6.92 | 3.20 | 4.54 | 8.02 | 8.22 | 2.43 | 5.82 | 7.73 | 0.48 | 5.44 | 6.77 | 0.20 | 6.17 |
| 208.92-211.98 | 3.07 | 4.98 | 5.10 | 2.12 | 3.19 | 3.26 | 2.21 | 1.91 | 3.17 | 2.39 | 1.99 | 3.51 | 3.77 | 3.11 | 3.79 | 2.76 | 5.04 | 5.82 | 5.03 | 4.60 | 7.98 | 7.65 | 3.41 | | 6.47 | 6.38 | 3.19 | 5.96 | 6.95 | 3.98 | 7.13 | 8.47 | 3.22 | 7.95 |

Table 5.1 Summer 1999 measured horizontal velocities (cm day⁻¹) used as input for the principal components analysis. Blank cells indicate missing data; pairwise deletion was used to remove these from the analysis. Stake locations are indicated in Figure 5.2.

| Factor | Eigenvalue | % explained variance |
|---------------|-------------------|-----------------------------|
| 1 | 17.13 | 50.4 |
| 2 | 4.60 | 13.5 |
| 3 | 2.43 | 7.1 |
| 4 | 2.10 | 6.2 |
| 5 | 1.71 | 5.0 |
| 6 | 1.46 | 4.3 |
| 7 | 1.32 | 3.9 |
| 8 | 1.07 | 3.2 |

Table 5.2 Eigenvalues and % explained variance for the principal component factors with an eigenvalue greater than 1.

| Stake number | Factor 1 loading | Factor 2 loading |
|--------------|------------------|------------------|
| 1 | 0.744 | 0.057 |
| 2 | 0.614 | 0.095 |
| 3 | 0.685 | 0.157 |
| 4 | 0.869 | 0.350 |
| 5 | 0.482 | -0.374 |
| 6 | 0.863 | 0.147 |
| 7 | 0.545 | 0.258 |
| 8 | 0.308 | 0.135 |
| 9 | 0.802 | 0.177 |
| 10 | 0.831 | -0.024 |
| 11 | 0.677 | 0.200 |
| 12 | 0.765 | 0.206 |
| 13 | 0.701 | 0.482 |
| 14 | 0.868 | -0.027 |
| 15 | 0.835 | 0.346 |
| 16 | 0.829 | 0.232 |
| 17 | 0.758 | 0.399 |
| 18 | 0.707 | 0.446 |
| 19 | 0.589 | 0.438 |
| 20 | 0.062 | 0.843 |
| 21 | 0.548 | 0.712 |
| 22 | 0.377 | 0.792 |
| 23 | 0.403 | 0.476 |
| 24 | 0.688 | 0.451 |
| 25 | 0.668 | 0.383 |
| 26 | 0.652 | 0.497 |
| 27 | 0.064 | 0.882 |
| 28 | 0.448 | 0.749 |
| 29 | 0.451 | 0.749 |
| 30 | -0.039 | 0.774 |
| 31 | 0.263 | 0.906 |
| 32 | 0.351 | 0.823 |
| 33 | -0.015 | 0.776 |
| 34 | 0.411 | 0.559 |

Table 5.3 Factor loadings for principal components analysis with the first two factors. Bold numbers indicate the factor that each stake loads most heavily on. The spatial distribution of the stakes grouped together by these factors is shown in Figure 5.3a.

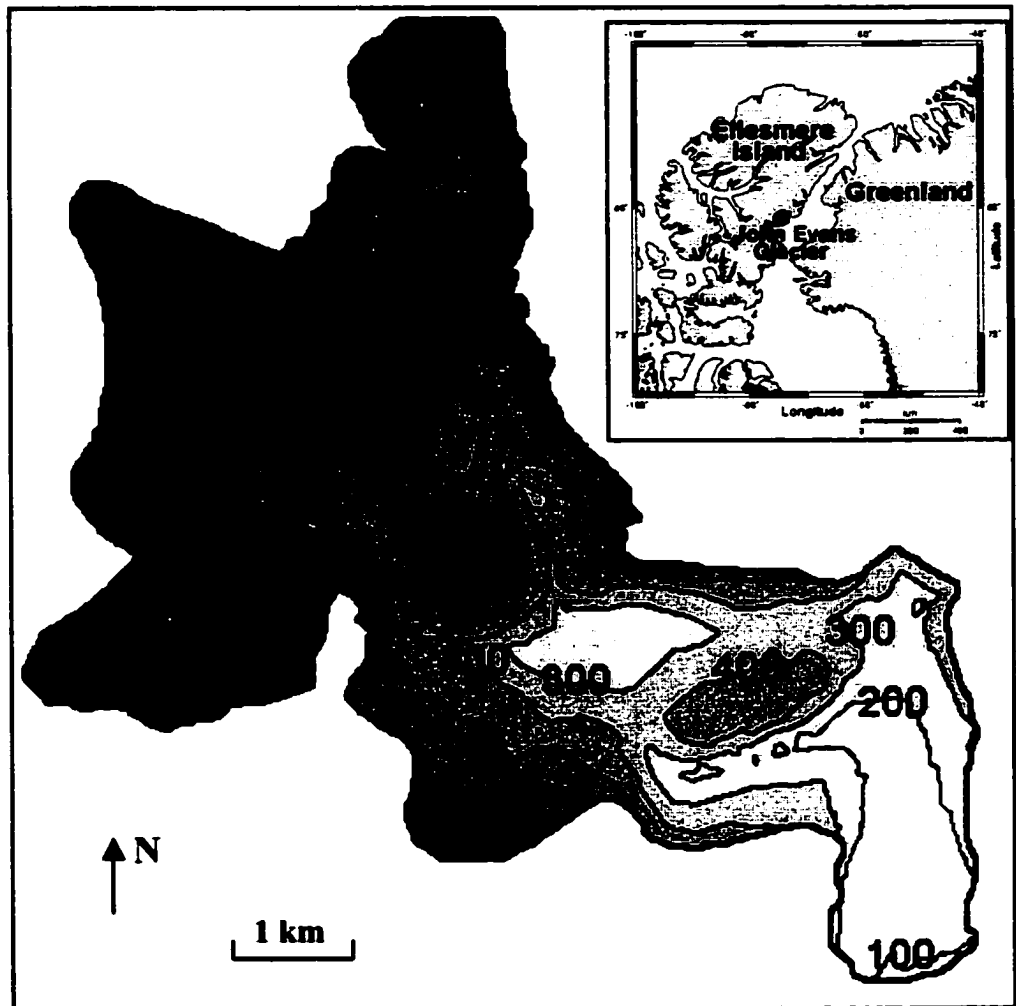


Figure 5.1 Bed topography (m asl) and location of John Evans Glacier

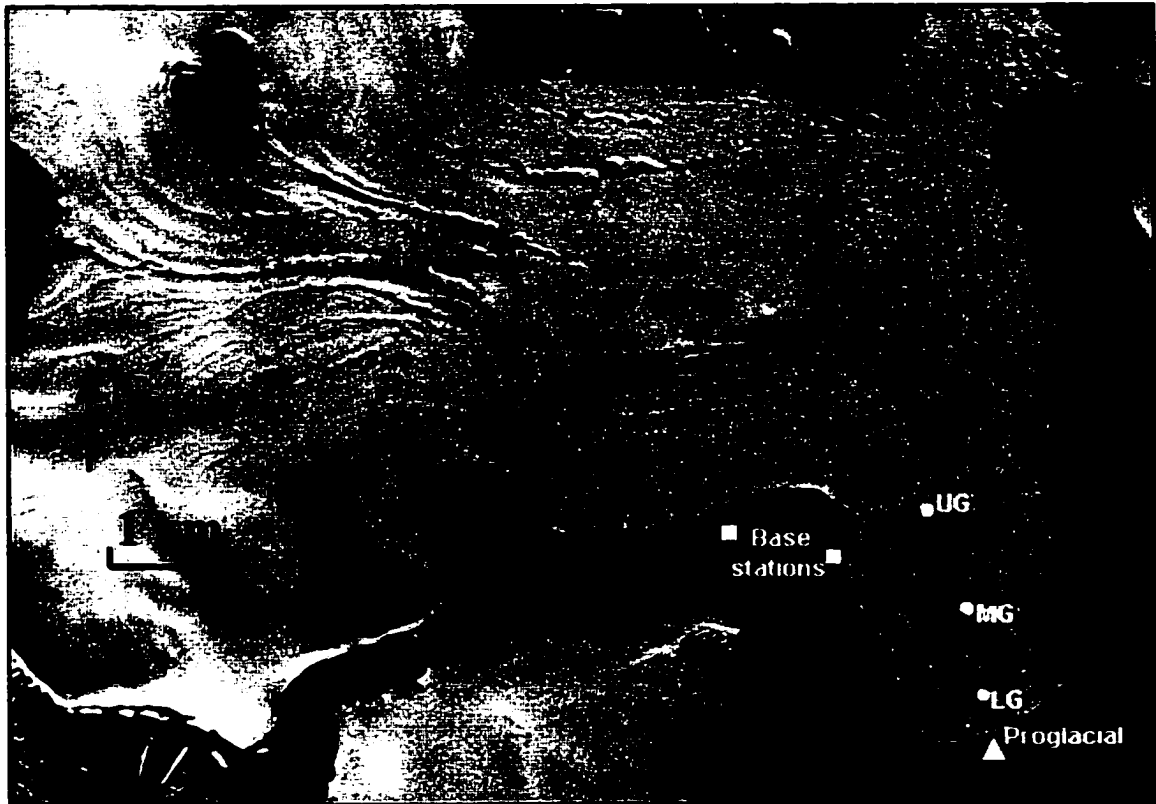


Figure 5.2 Landsat 7 image of John Evans Glacier from July 1999 showing the location of the velocity stakes (numbered black dots), geophones (white dots; LG = lower geophone, MG = middle geophone, UG = upper geophone), surveying base stations (white squares), stream gauging stations (triangles). Crevasse field indicates location where most supraglacial meltwater reaches the glacier bed. Lower weather station is located next to the middle geophone.

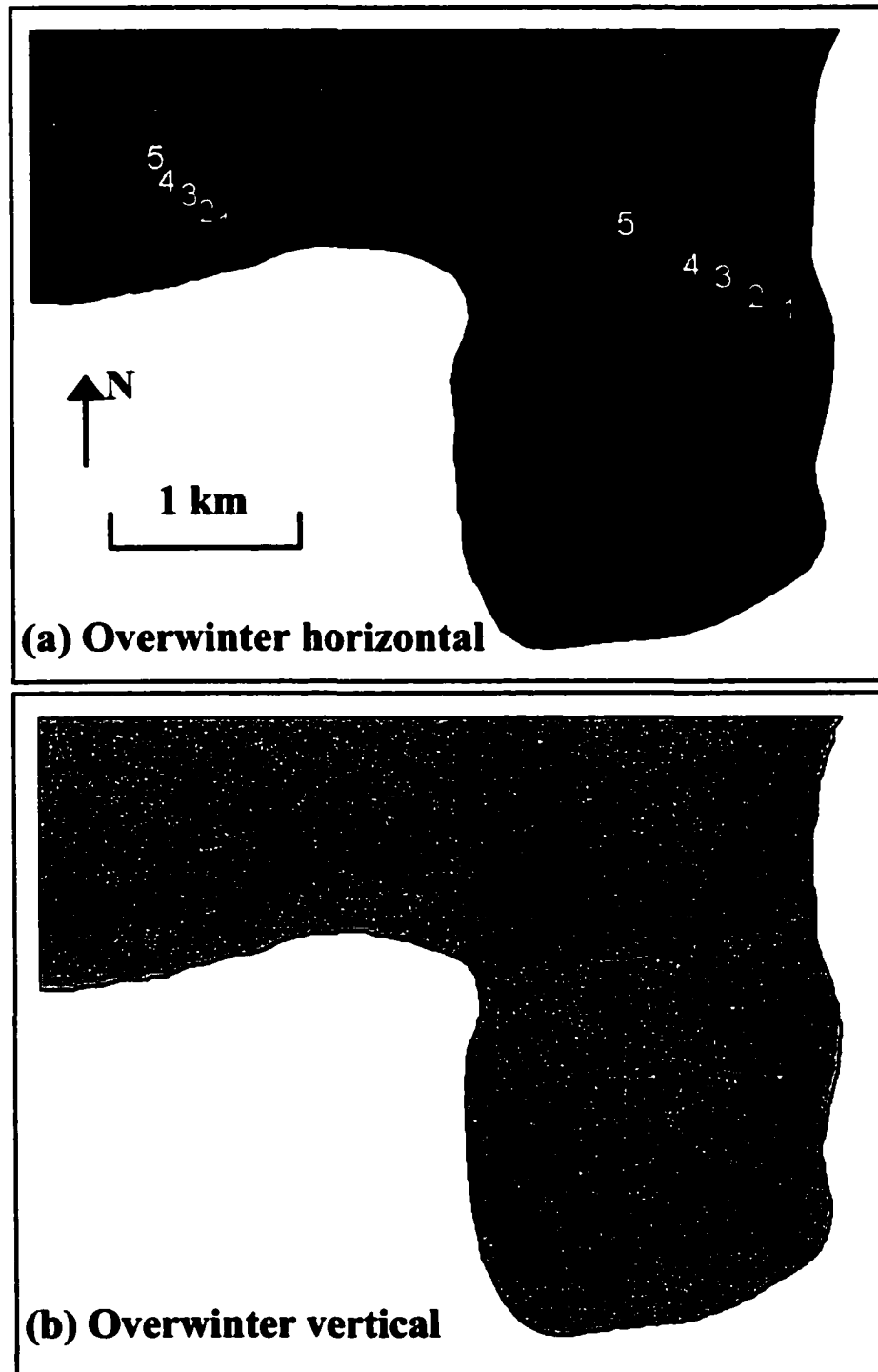


Figure 5.3 (a) Overwinter 1999/2000 horizontal velocities. Each arrow indicates the direction and velocity of a stake. Black squares indicate stakes grouped into Factor 1 in principal components analysis; black circles indicate stakes grouped into Factor 2. (b) Overwinter 1999/2000 vertical velocities. All velocities in cm day^{-1} .

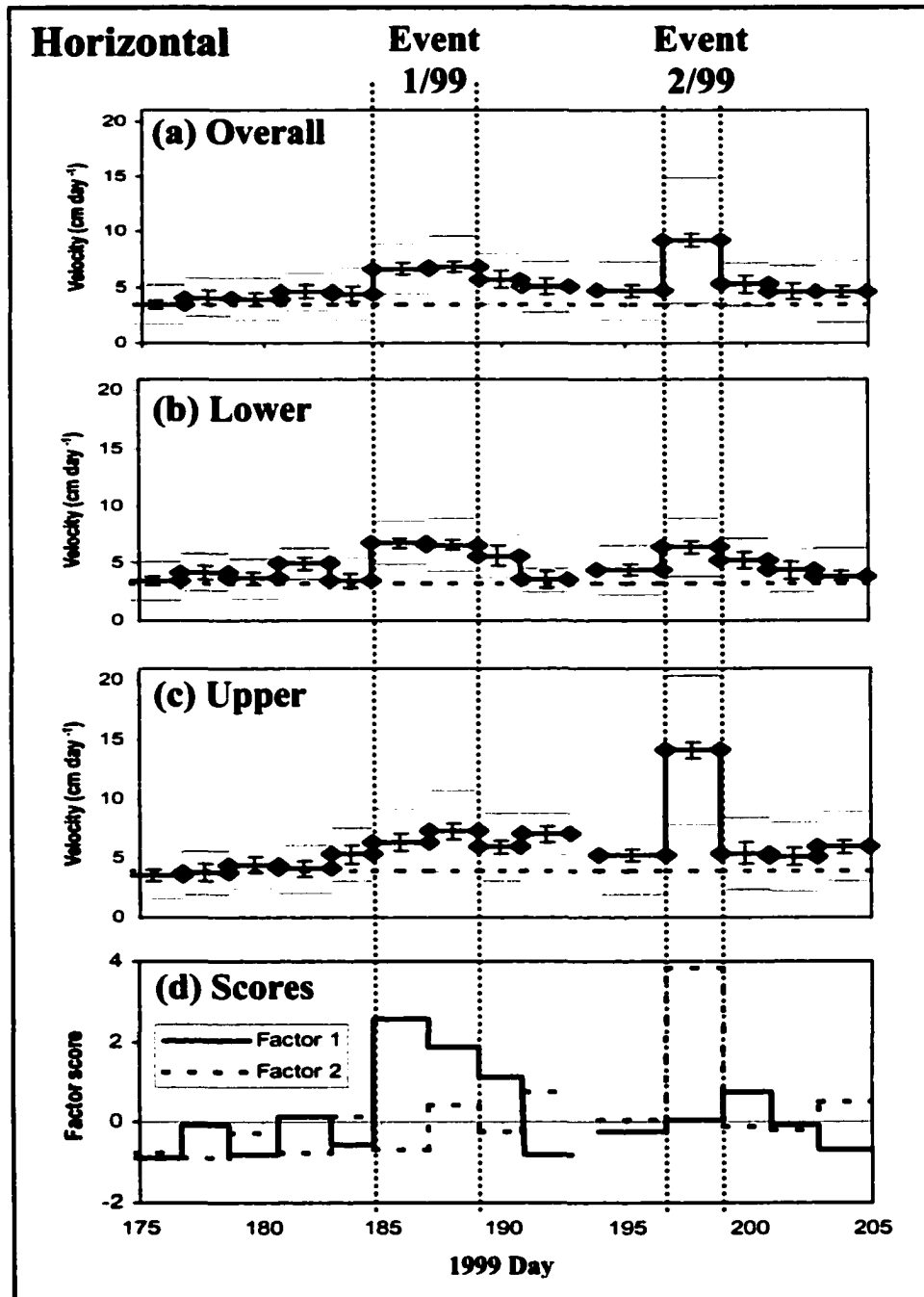


Figure 5.4 Summer 1999 mean horizontal velocities (solid line), overwinter 1999/2000 mean horizontal velocities (dashed line), errors in horizontal velocity (vertical bars), and standard deviation in horizontal velocity (grey lines): (a) for all stakes (b) for stakes grouped by factor 1 in principal components analysis (i.e., lower terminus) (c) for stakes grouped by factor 2 in principal components analysis (i.e., upper terminus). All velocities in cm day^{-1} . (d) Factor scores over time for the two factors.

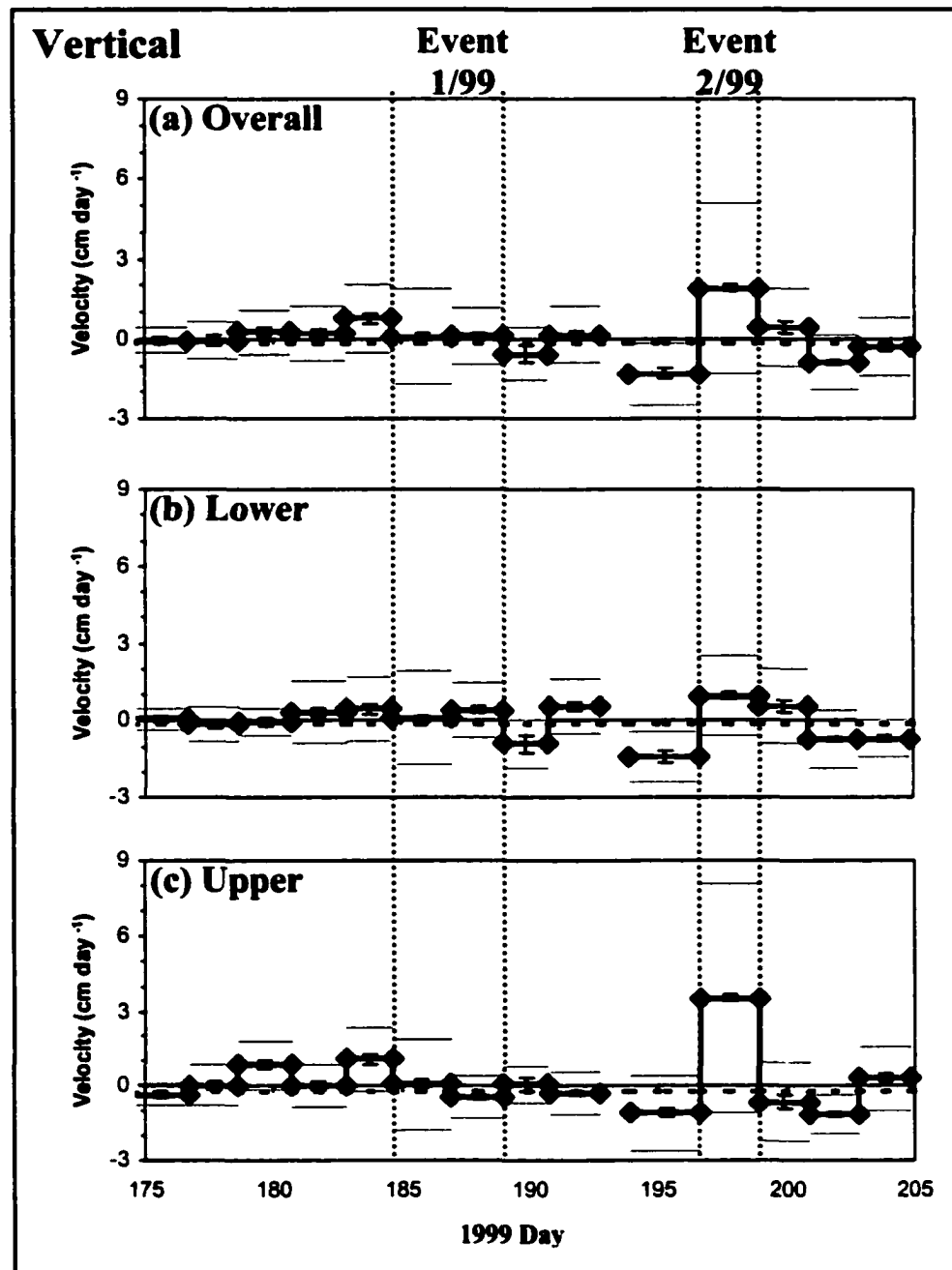


Figure 5.5 Summer 1999 mean vertical velocities (solid line), overwinter 1999/2000 mean vertical velocities (dashed line), errors in vertical velocity (vertical bars), and standard deviation in vertical velocity (grey lines): (a) for all stakes (b) for stakes grouped by factor 1 in principal components analysis (i.e., lower terminus) (c) for stakes grouped by factor 2 in principal components analysis (i.e., upper terminus). All velocities in cm day^{-1} .

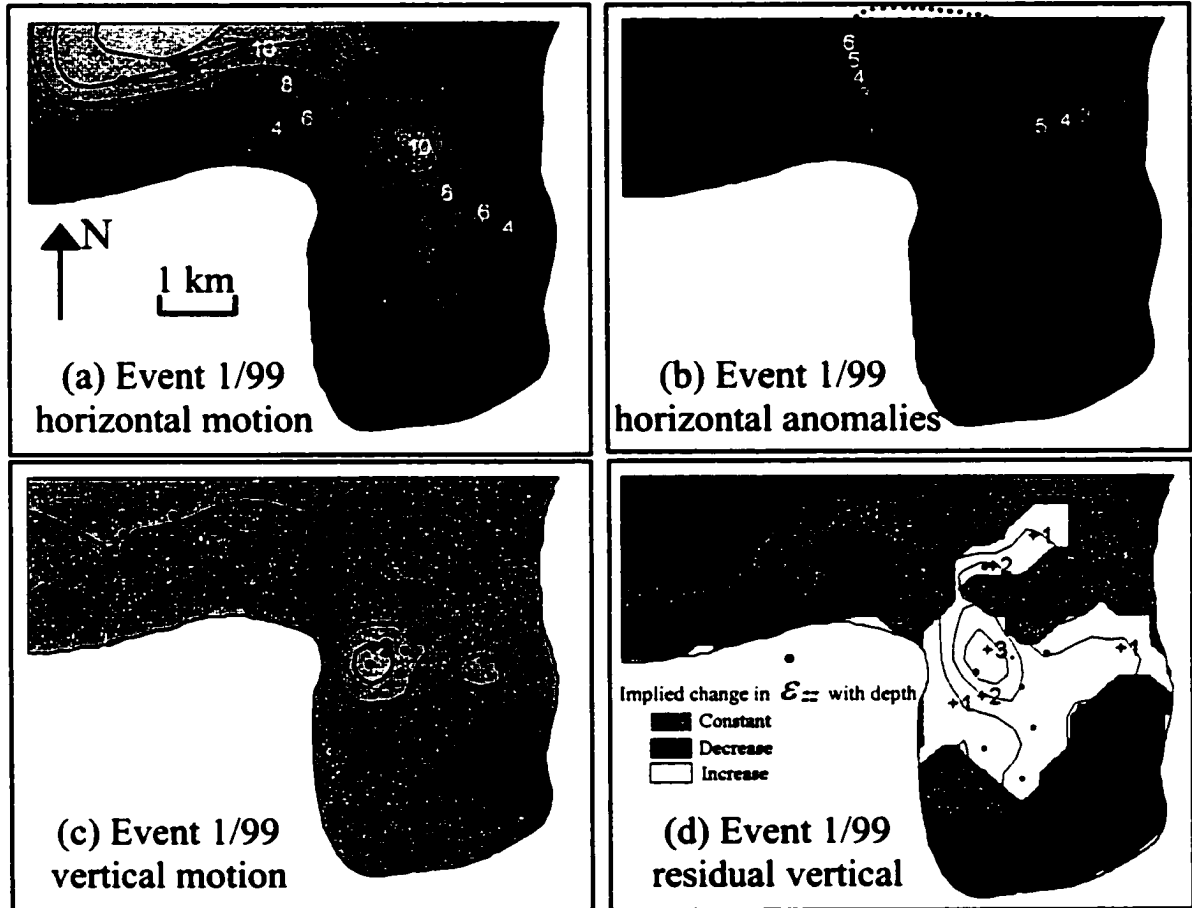


Figure 5.6 Event 1/99 (days 184.60-189.04) velocities in cm day^{-1} : (a) horizontal (b) horizontal anomalies (i.e., difference from overwinter 1999/2000) (c) vertical (d) residual vertical: cavity opening is only likely where the assumption that $w_c = 0$ requires ϵ_{zz} to increase with depth relative to ϵ_{zzs} . Black lines in (b) mark reconstructed subglacial drainage pathways.

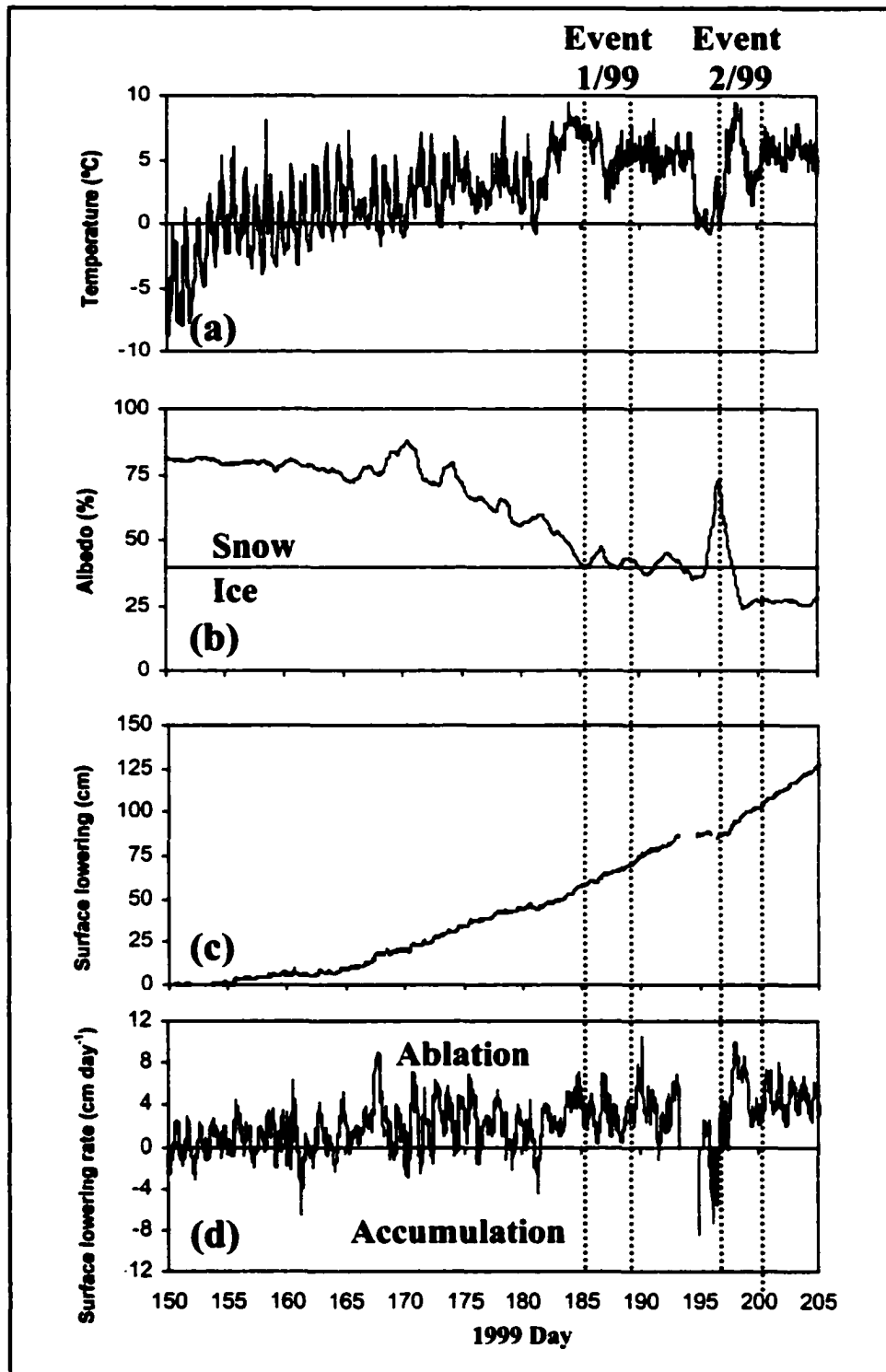


Fig. 5.7 Summer 1999 lower weather station records: (a) air temperature (b) albedo (%): a value of 40% is defined as the approximate boundary between snow and ice (c) total surface lowering (cm), determined from an ultrasonic depth gauge (UDG) (d) rate of surface lowering (cm day⁻¹) determined from the UDG

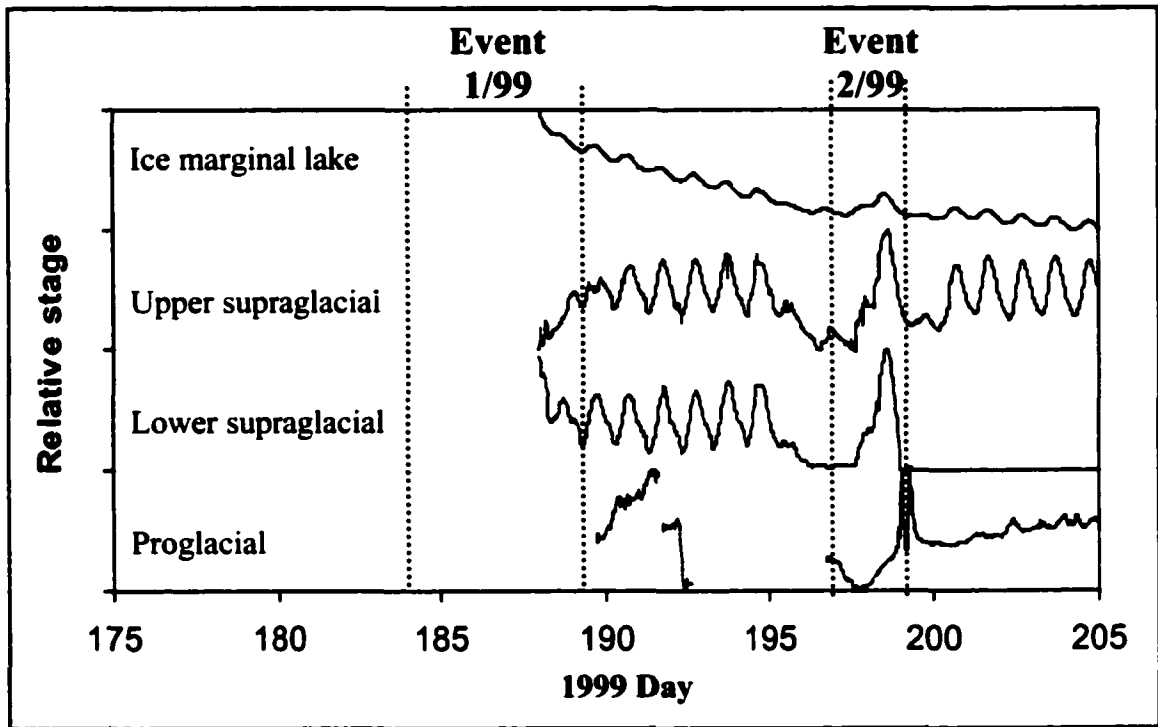


Figure 5.8 Water pressure records for summer 1999 (see Fig. 5.2 for sensor locations). The measurements are standardized between the highest and lowest values from each sensor over the period of interest. The proglacial sensor is repositioned during breaks.

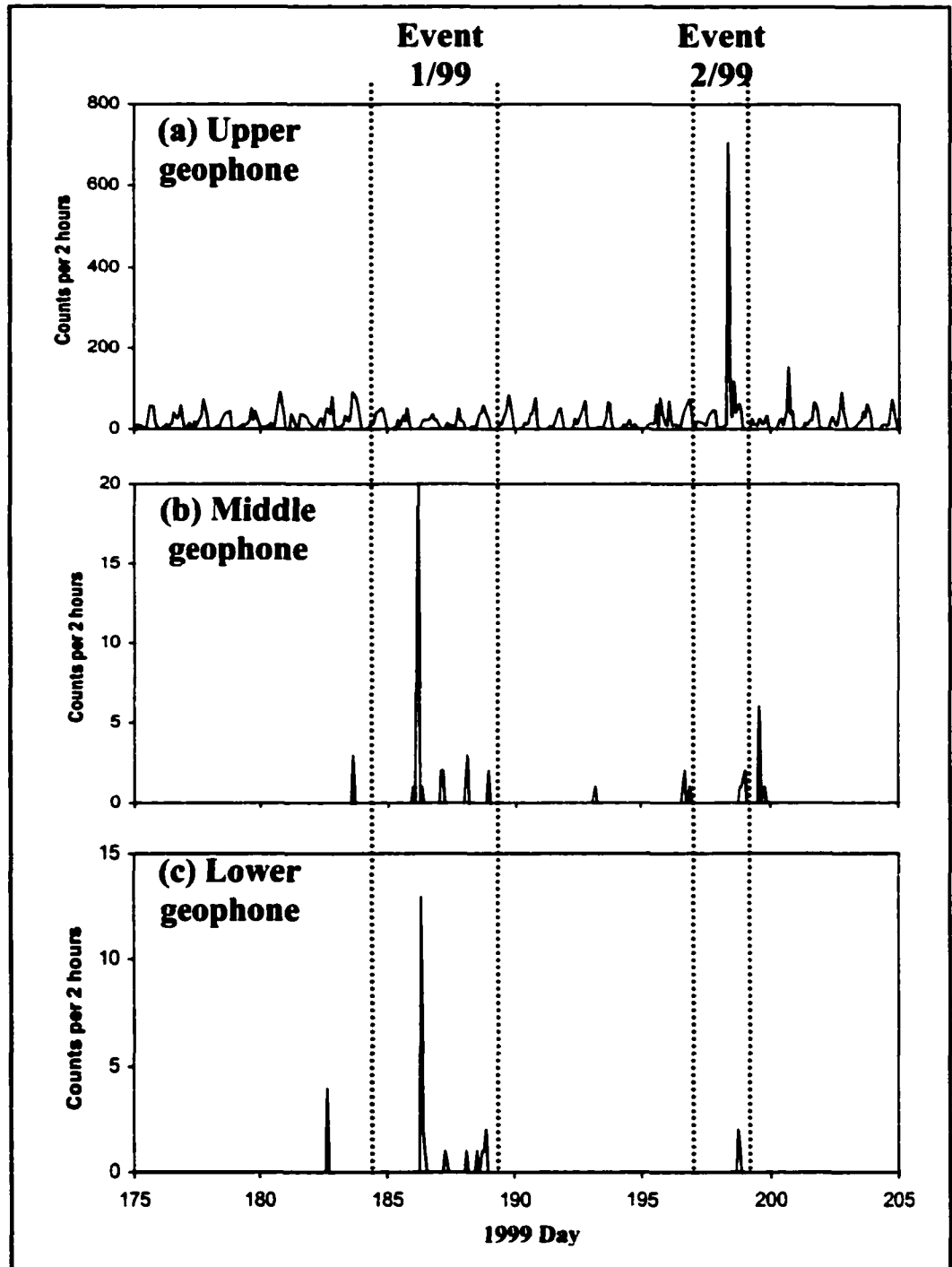


Figure 5.9 Summer 1999 geophone records: (a) upper geophone (b) middle geophone (c) lower geophone. Note that only the relative magnitude of events are comparable between geophones, not the actual number of counts.

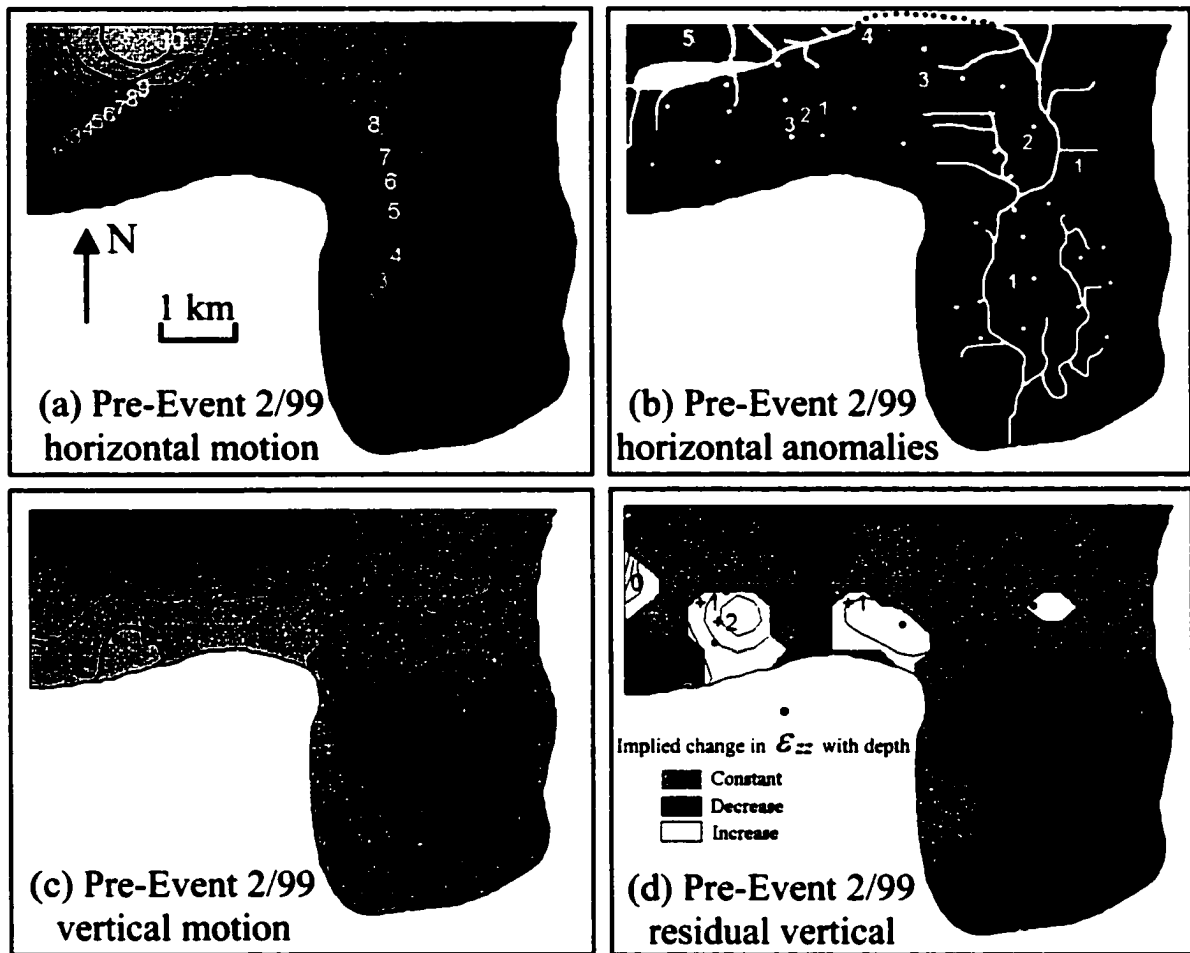


Figure 5.10 Pre-Event 2/99 (days 193.92-196.60) velocities in cm day^{-1} : (a) horizontal (b) horizontal anomalies (i.e., difference from overwinter 1999/2000) (c) vertical (d) residual vertical: cavity opening is only likely where the assumption that $w_c = 0$ requires ϵ_{zz} to increase with depth relative to ϵ_{zz} .

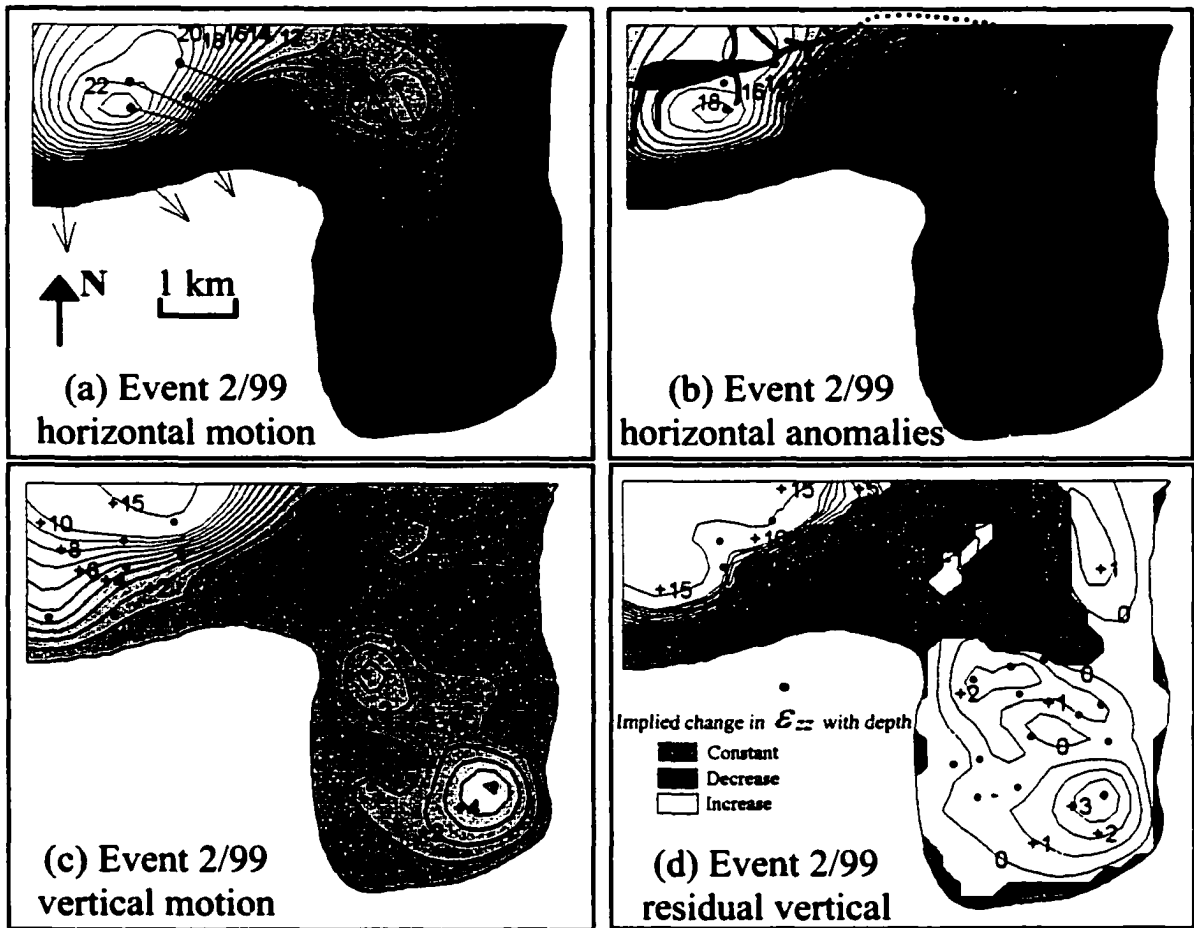


Fig. 5.11 Event 2/99 (days 196.60-198.88) velocities in cm day^{-1} : (a) horizontal (b) horizontal anomalies (i.e., difference from overwinter 1999/2000) (c) vertical (d) residual vertical: cavity opening is only likely where the assumption that $w_c = 0$ requires ϵ_{zz} to increase with depth relative to ϵ_{zzs} .

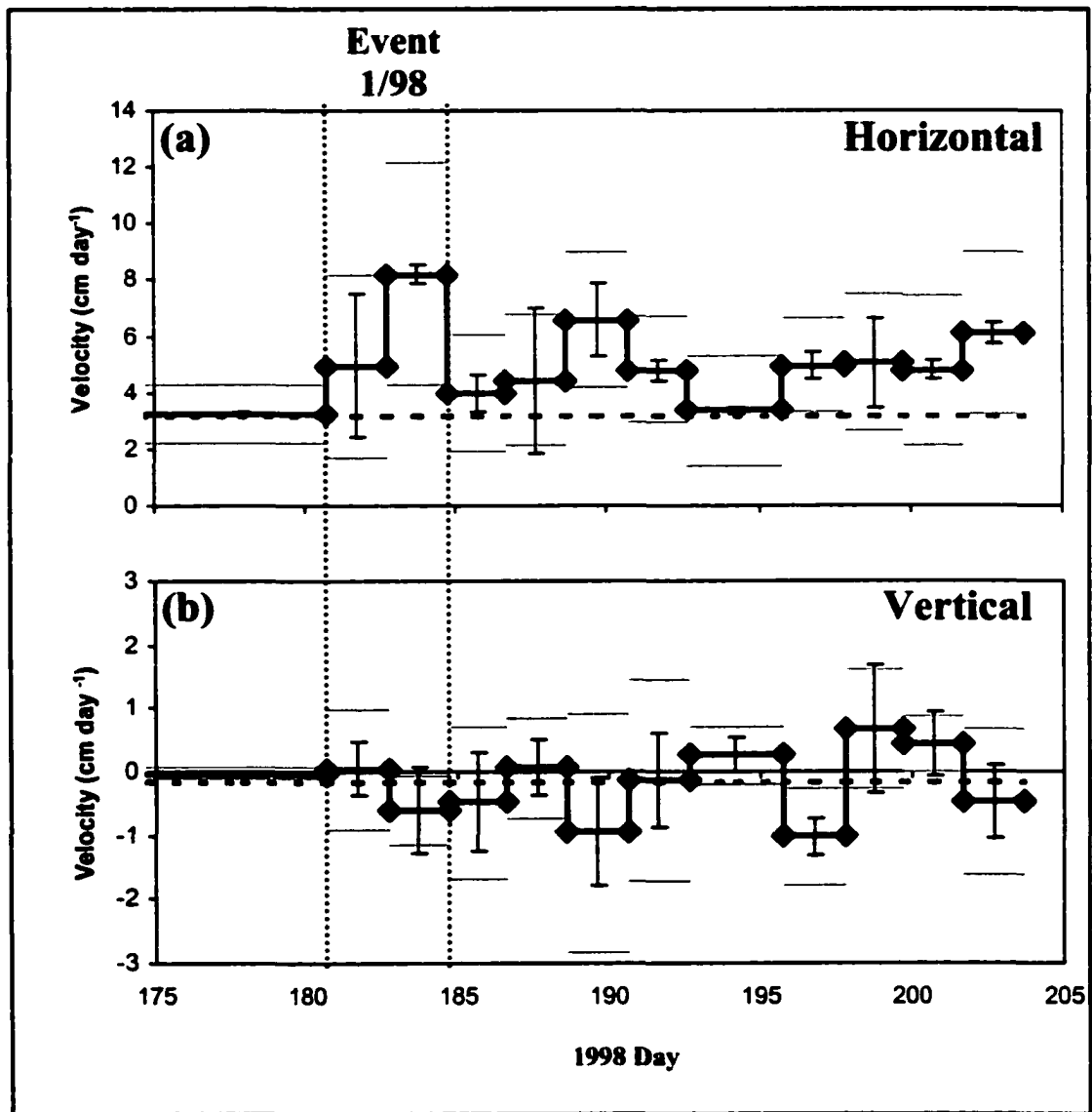


Figure 5.12 Summer 1998 (a) horizontal and (b) vertical, mean velocity (solid line), overwinter 1999/2000 mean velocity (dashed line), errors in velocity (vertical bars), and standard deviation in velocity (grey lines). All values in cm day^{-1} . An additional 6 stakes were added to the original network of 15 from day 185 onwards.

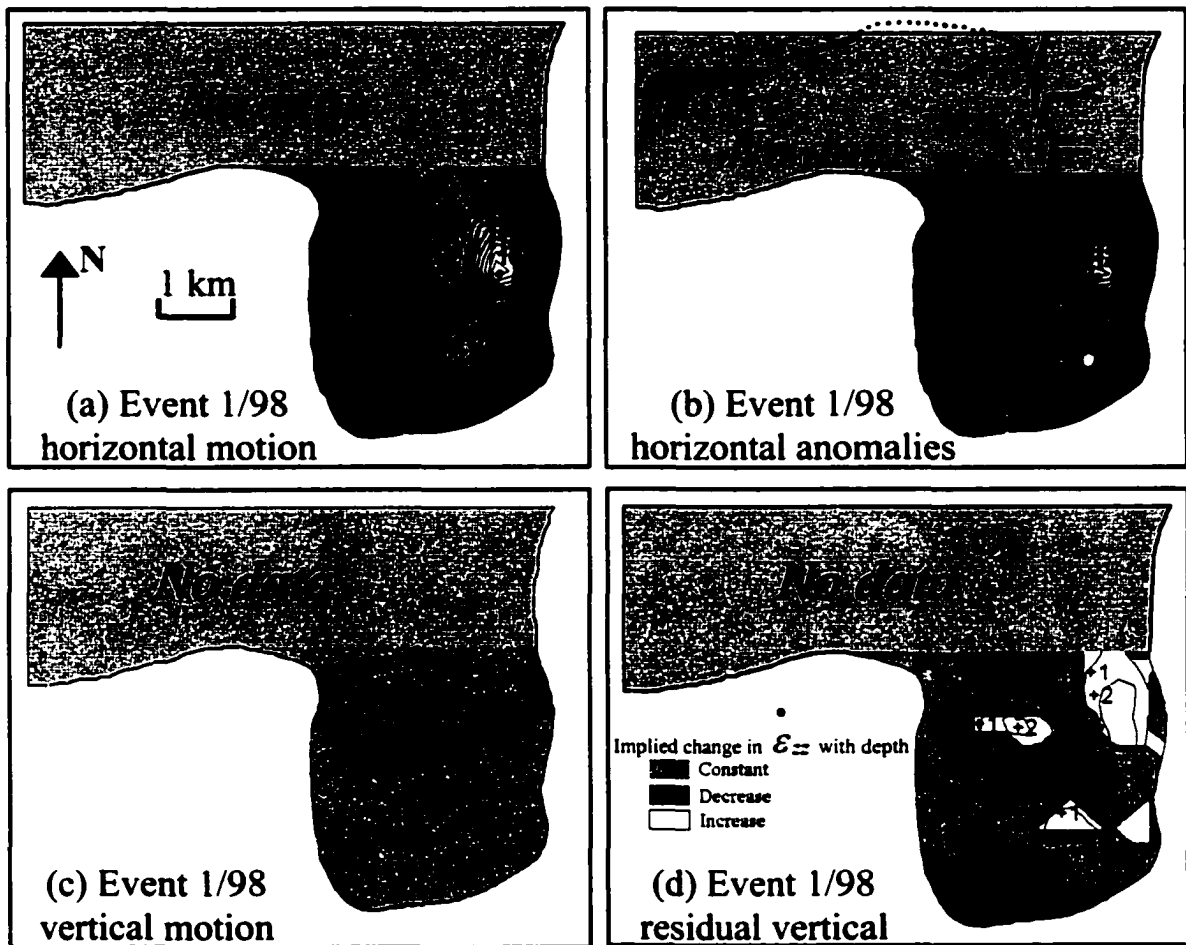


Figure 5.13 Event 1/98 (days 182.70-184.70) velocities in cm day^{-1} : (a) horizontal (b) horizontal anomalies (i.e., difference from overwinter 1999/2000) (c) vertical (d) residual vertical: cavity opening is only likely where the assumption that $w_c = 0$ requires ϵ_{zz} to increase with depth relative to ϵ_{zzs} . In (b), white circle indicates location of artesian fountain pictured in Fig. 5.15.

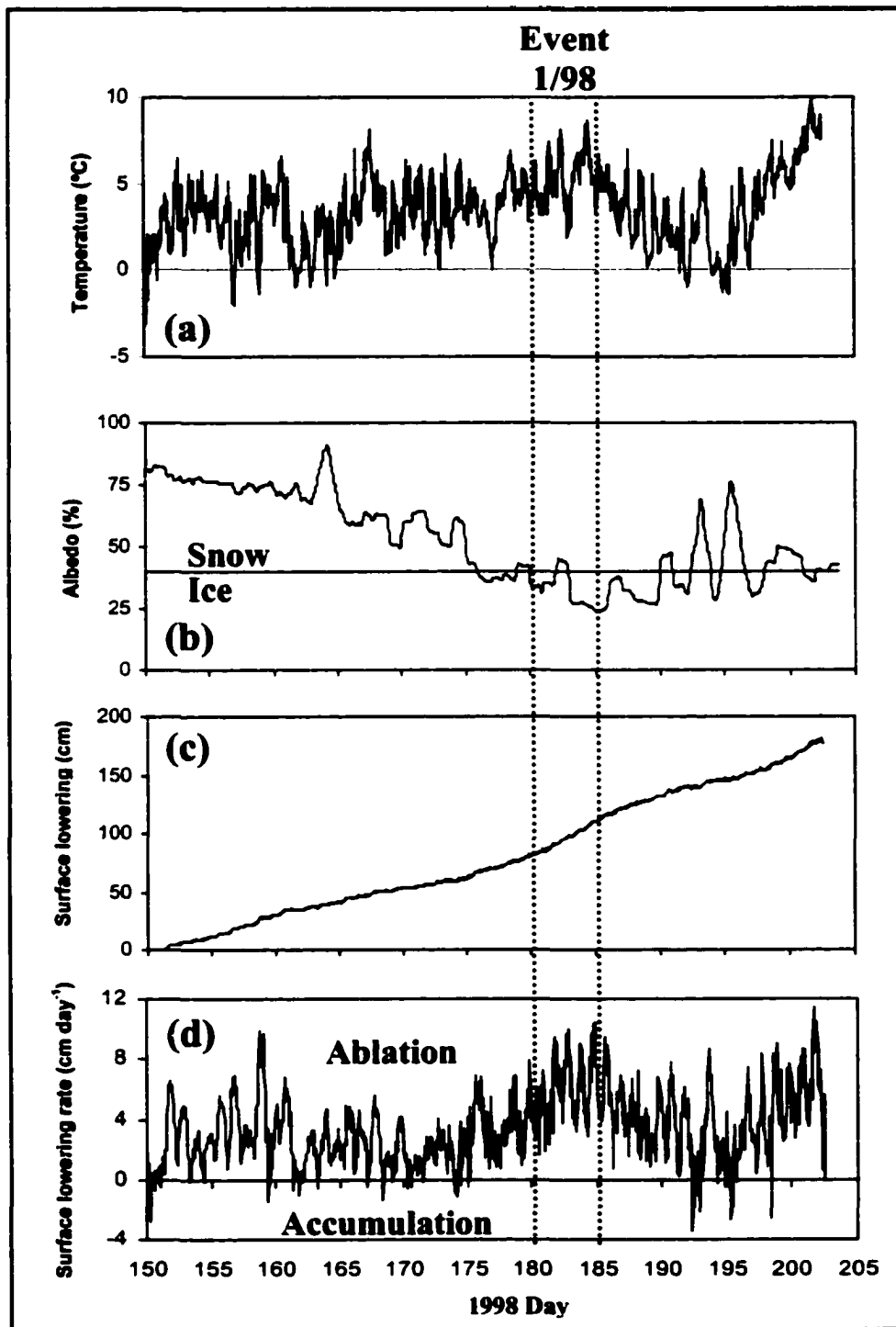


Figure 5.14 Summer 1998 lower weather station records: (a) air temperature (b) albedo (%): a value of 40% is defined as the approximate boundary between snow and ice (c) total surface lowering (cm), determined from an ultrasonic depth gauge (UDG) (d) rate of surface lowering (cm day^{-1}) determined from the UDG



Fig. 5.15 Artesian fountain observed on the lower terminus between days 180 and 186, 1998. Photograph by Martin Sharp.

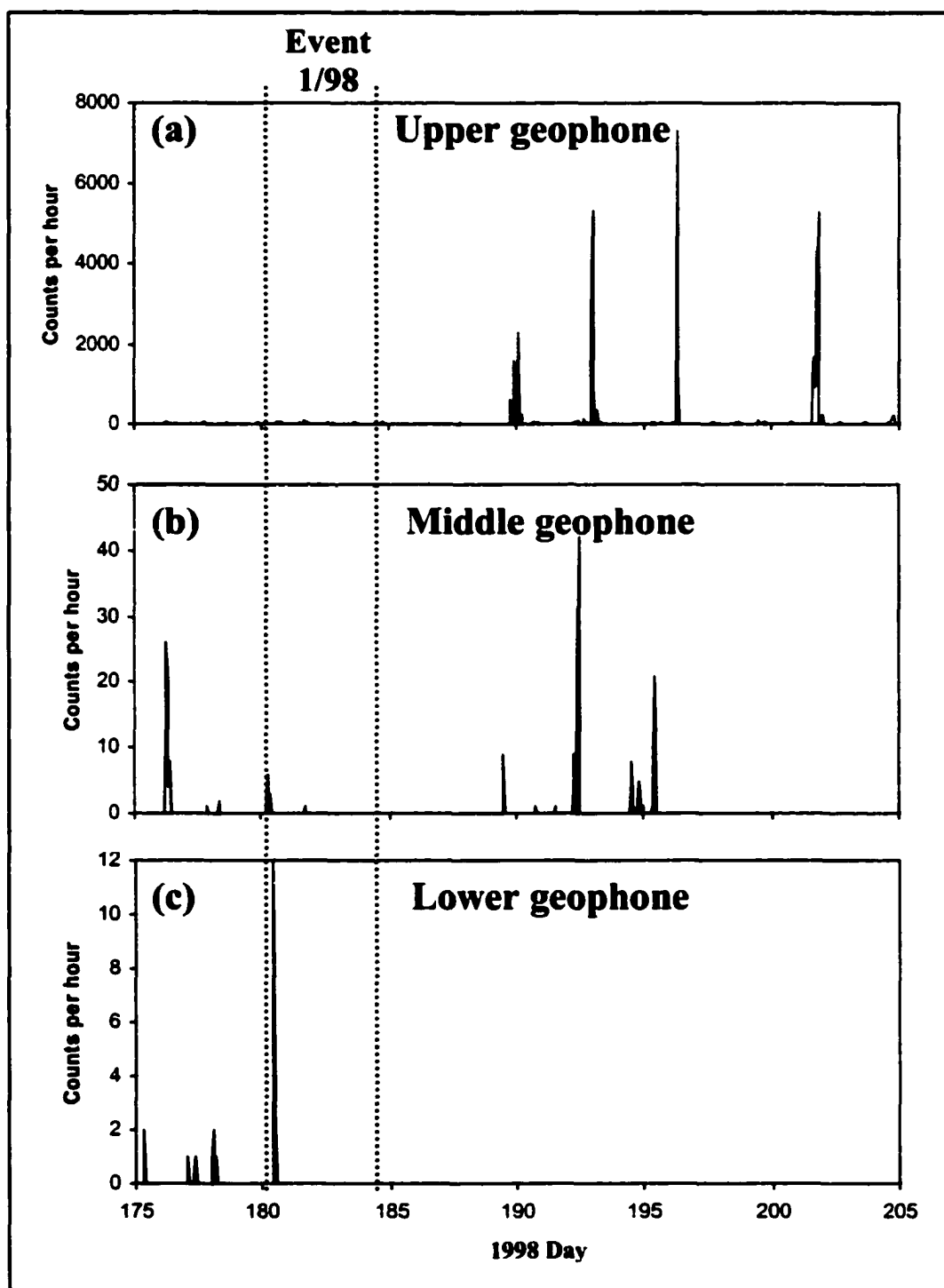


Figure 5.16 Summer 1998 geophone records: (a) upper geophone (b) middle geophone (c) lower geophone. Note that only the relative magnitude of events are comparable between geophones, not the actual number of counts.

CHAPTER 6

SUMMARY AND CONCLUSIONS

6.1 SUMMARY

This study has shown that there are strong links between the hydrology and dynamics of a polythermal glacier, with variations in ice motion occurring on timescales from days to months in relation to varying surface water inputs. Similar variations have previously been observed on temperate glaciers, but not at such high spatial and temporal resolutions on a polythermal glacier.

Most of the information about the hydrology and englacial and basal properties of John Evans Glacier has been provided by radio-echo sounding:

- (a) Ice depths were determined from the timing of the bed reflection, with travel time converted to true ice depth by using a mean radio-wave velocity of 0.1711 ± 0.0031 m ns⁻¹ measured in common mid-point surveys. The subglacial hydraulic potential surface was calculated from the ice thicknesses and bed topography, and was in turn used to predict the routing of water across the glacier bed.
- (b) The thermal structure of the glacier was determined from spatial patterns in residual bed reflection power (BRP_r). BRP_r is the difference between measured BRP and BRP predicted from the relationship between measured BRP and ice thickness (which describes the rate of apparent attenuation with depth in the glacier), and enabled division of the glacier into three areas: (i) Positive BRP_r and an internal reflecting horizon occurred over the glacier terminus. The reflecting horizon is interpreted as the boundary between warm and cold ice, and suggests the presence of a warm basal layer. (ii) Positive BRP_r occurred without an internal reflector in the upper part of the ablation zone, which suggests that ice is at the pressure melting point only at the bed. (iii) Negative BRP_r without an internal reflector occurs in all other regions, suggesting cold ice at the bed.
- (c) In regions where BRP_r is positive, the detailed pattern of BRP_r was similar to the pattern of subglacial water flow predicted from the subglacial hydraulic potential

surface. This suggests that hydrological conditions at the glacier bed are a major control on BRP_r, probably because the dielectric contrast between ice and water is higher than that between ice and other subglacial materials.

- (d) Internal and near-surface features such as moulins and crevasses were identified by high englacial reflection powers. This provides a method for remotely mapping near-surface features which are often snow covered and difficult to access in the field.
- (e) Repeat traces collected over a 9 day period in July 1999 appear to show a relationship between basal reflection strength, air temperature, and supraglacial/proglacial stream discharge. The strength of the ground wave did not correlate with the bed reflection power, which suggests that the variability in basal reflection strength is related to physical changes at the glacier bed, and not to differences in surface coupling. This method may therefore provide a way to remotely monitor changes in basal hydrology.

Surface velocity measurements indicate that ice motion was slightly higher in the summer than in the winter in the accumulation area, but it was almost 100% higher in the summer than in the winter in the ablation area. Ice deformation can account for the observed motion in the accumulation and upper ablation areas, but it is insufficient to account for all of the motion in the lower ablation area in either the summer or the winter. To match the observed velocities in this area in the winter requires a basal motion anomaly with two peaks. The first peak occurs in an area where the radio-echo sounding and subglacial drainage reconstructions suggest that subglacial water is present throughout the year in an overdeepening. In addition, this area is located upstream from a region of thick ice and steep surface slopes, where rapid conduit closure at the end of the melt season may trap subglacial water upstream. The second peak in basal motion is close to the glacier terminus, in an area where the radio-echo sounding and meltwater chemistry suggest that water is present overwinter. Water becomes trapped in this area due to the presence of a thermal dam at the glacier snout formed by the penetration of cold winter temperatures. In summer, basal motion increases in magnitude and accounts for up to 75% of the total surface motion throughout the lower ablation area. This summer basal motion initiates just downglacier from the main location where meltwater flowed to the glacier bed via a series of moulins. Longitudinal stresses are important in

increasing the surface area affected by basal motion variations up to 2 km from their source, with a longitudinal coupling length of four times the local ice thickness providing the best fit to observations. Longitudinal stresses have the effect of decreasing ice deformation in areas where there is high basal motion, but increasing ice deformation where there is a change from an area of high to low or no basal motion.

On the small scale, three short-term (two- to four-day) high velocity events were recorded in the summers of 1998 and 1999 during periods of rapidly increasing meltwater flow to the glacier bed. The first events in 1998 and 1999 occurred at the start of the melt season at the transition from a snow covered to an ice covered surface. A second event in 1999 occurred midway through the summer as surface melting resumed following a cold period. Horizontal velocities were typically >100% above overwinter levels during these events, although the changes were spatially non-uniform, and only the second event in 1999 correlated with significant changes in vertical motion. The lack of significant vertical motion changes during the early season events in either 1998 or 1999 suggest that basal motion was the result of widespread lubrication of the glacier bed, as basal water was trapped behind the thermal dam at the snout. Horizontal velocities were highest upstream from an artesian fountain in a narrow region above a predicted subglacial drainage axis during the 1998 early season event. This observation suggests that the local concentration of basal water played an important role in enhancing surface horizontal motion. The largest horizontal and vertical velocity increases during the mid-season event in 1999 occurred along a subglacial drainage axis upstream from the region where closure of drainage passages was maximised during the preceding cold spell. These observations suggest that the main basal motion mechanism changed between the early and mid-season events, with basal cavity opening along subglacial drainage axes providing the dominant source of basal motion later in the summer.

6.2 CONCLUSIONS

This study has significantly advanced our understanding of the thermal structure, hydrology and ice dynamics of polythermal glaciers, and the links between them. Detailed analysis of variations in BRP, in radio-echo sounding records, combined with information about the presence and distribution of an internal reflecting horizon, has

provided detailed information about the englacial and subglacial thermal structure of John Evans Glacier. Gades et al. (2000) previously looked at similar variations in BRP_T across a single transect at Siple Dome, Antarctica, to infer the presence of basal water, but here we describe for the first time a successful application to a polythermal valley glacier with complex basal topography. Analysis of local variations in positive BRP_T also provides a new method for identifying and tracking subglacial drainage routing on scales potentially as small as individual channels. Our previous understanding of polythermal glacier hydrology has been mainly based on analysis of tracers, meltwater chemistry, and the discharge of streams as they enter and exit the subglacial system (Jansson, 1996; Hodgkins, 1997; Skidmore and Sharp, 1999; Wadham et al., 2000), or from variations in basal water pressure in moulins and boreholes (Iken, 1974; Hooke et al., 1988). While these studies provide useful information about temporal variations in basal water flow, they cannot provide the detailed spatial resolution available from radio-echo sounding.

We have demonstrated that basal motion occurs throughout the year over the lower ablation area of the glacier, with higher basal velocities in the summer than the winter. Most previous studies on polythermal glaciers have been restricted to measurements during the short summer melt season (e.g., Andreasen, 1985; Iken, 1974), with only Rabus and Echelmeyer (1997) making a convincing case for basal sliding in the winter. Rabus and Echelmeyer (1997) did not have any hydrological information to compare with their measured velocities, whereas we have demonstrated that the location of subglacial drainage elements is closely correlated to areas of high basal motion. In particular, the thermal dam at the glacier snout traps basal meltwater upglacier in a way not seen in temperate glaciers. This phenomenon enables basal sliding even when midwinter temperatures reach -40°C .

Superimposed within the areas of basal sliding are increases in surface motion of up to 400% above overwinter levels on timescales of two days or less in the summer. These high motion events occur during periods of rapidly increasing surface meltwater input to the glacier bed, with the high spatial resolution of our measurements demonstrating that local increases occur within close proximity to subglacial drainage paths. In addition, measurements of vertical motion suggest that the dominant basal motion mechanism changes through the melt season from a widespread lubrication of the

bed to strongly localized uplift along subglacial drainage channels. Iken (1974) demonstrated that short-term velocity variations occurred in close correlation with the water pressure measured in a nearby moulin on White Glacier, Axel Heiberg Island, while Battle (1949), Andreasen (1985), and Rabus and Echelmeyer (1997), all recorded short-term velocity variations on polythermal glaciers, but could not make detailed comparisons with subglacial drainage conditions.

The high spatial and temporal resolution of our ice motion measurements has demonstrated that polythermal glaciers are much more dynamic than previously believed, with a close association between ice motion variations and the distribution and development of subglacial drainage. This is similar to observations on temperate glaciers, but the unique subglacial hydrology of polythermal glaciers created by features such as the thermal dam at the snout, mean that the two are not directly comparable. This dynamic variability needs to be taken into account when modelling the response of high latitude glaciers to climate change.

6.3 BIBLIOGRAPHY

Andreasen, J.-O., 1985. Seasonal surface-velocity variations on a sub-polar glacier in West Greenland. *Journal of Glaciology*, **31**(109), 319-323.

Battle, W.R.B. 1951. Glacier movement in North-East Greenland, 1949. *Journal of Glaciology*, **1**(10), 559-563.

Gades, A.M., Raymond, C.F., Conway, H. and Jacobel, R.W. 2000. Bed properties of Siple Dome and adjacent ice streams, West Antarctica, inferred from radio-echo sounding measurements. *Journal of Glaciology*, **46**(152), 88-94.

Hodgkins, R. 1997. Glacier hydrology in Svalbard, Norwegian High Arctic. *Quaternary Science Reviews*, **16**, 957-973.

Hooke, R.LeB., Miller, S.B., and Kohler, J. 1988. Character of the englacial and subglacial drainage system in the upper part of the ablation area of Storglaciären, Sweden. *Journal of Glaciology*, **34**(117), 228-231.

Iken, A. 1974. Velocity fluctuations of an Arctic valley glacier, a study of the White glacier, Axel Heiberg Island, Canadian Arctic Archipelago. *Axel Heiberg Island Research Reports, Glaciology no. 5*. McGill University, Montreal.

Jansson, P. 1996. Dynamics and hydrology of a small polythermal valley glacier. *Geografiska Annaler*, **78A**(2-3), 171-180.

Rabus, B.T. and Echelmeyer, K.A. 1997. The flow of a polythermal glacier: McCall Glacier, Alaska, U.S.A. *Journal of Glaciology*, **43**(145), 522-536.

Skidmore, M.L. and Sharp, M.J. 1999. Drainage system behaviour of a High Arctic polythermal glacier. *Annals of Glaciology*, **28**, 209-215.

Wadham, J.L., Tranter, M. and Dowdeswell, J.A. 2000. Hydrochemistry of meltwaters draining a polythermal-based, high-Arctic glacier, south Svalbard: II. Winter and early Spring. *Hydrological Processes*, **14**(10), 1767-1786.